# Charles University

## Faculty of Science

Study program: Modelling of Chemical Properties of Nano- and Biostructures




**M.Sc. Shuo Li**


# Theoretical Investigation of Low-dimensional Magnetic Materials

# Teoretické studium nízkorozměrových magnetických materiálů

Type of thesis

Doctoral thesis


Supervisor: RNDr. Lukáš Grajciar, Ph.D.

Advisor: Prof. RNDr. Petr Nachtigall, Ph.D.



Prague, 2021

*I dedicate this thesis to*

*my wife, Ran Wang*

*for her love and uncondictional support.*

# Acknowledgment

First of all, I would like to express my sincere gratitude to my supervisor, Lukáš Grajciar for giving me an opportunity to study, work, and live in Prague. I really appreciate his scientific interests and dedication for my PhD study. Then I would like to thank the group leader and my advisor, Prof. Petr Nachtigall. My thesis is impossible to complete without his patient guidance and supports. I sincerely appreciated his heartwarming encouragement, nice guidance, and great assistance in my research and life. I have four years of pleasant time in here, which is a part of most precious memory in my life.

Second, I also want to thank my colleagues in our group for all their help: Dr. Junjie He, Dr. Federico Brivio, Dr. Christopher James Heard, Dr. Andreas Erlebach, M.Sc. Mingxiu Liu, M.Sc. Dianwei Hou, M.Sc. Chen Lei, and M.Sc. Mengting Jin, as well as other members. Then, I am grateful to experimental collaborators in the group of Prof. Jiří Čejka, Dr. Pavla Eliášová, Dr. Mohamed Infas Haja Mohideen, Dr. Michal Mazur, and M.Sc. Ang Li for their insightful discussions. I also thank Dr. Carlos Henrique Vieira Melo, who taught me a lot of scientific writing skills and helped me a lot with manuscripts writing. I would like to express my deep thanks to other people in our department, with whom I have discussed and learned. I also would like to thank Dr. Ke Li, in Ireland; Prof. Yuxi Xu, in China, for their wonderful collaboration.

Finally, I would like to thank my wife, Ran Wang and my parents for all their understanding providing me with support and encouragement through my doctoral life. Thank you very much!

Shuo Li

*In Prague*

July 2021

## Prohlášení

Dizertační práci jsem vypracoval na Přírodovědecké fakultě, Univerzity Karlovy.
Prohlašuji, že jsem závěrečnou práci zpracovala samostatně a že jsem uvedla všechny použité informační zdroje a literaturu. Tato práce ani její podstatná část nebyla předložena k získání jiného nebo stejného akademického titulu.

## Declaration

I did my dissertation at the Faculty of Science, Charles University.
I declare that I have prepared the thesis independently and that I have listed all the information sources and literature used. Neither this thesis nor any substantial part of it has been submitted for another or the same academic degree.

Signed:

_____

Date:

_____

# Table of Contents

# Abstract

Low-dimensional (D) materials, such as graphene, transition metal dichalcogenides and chalcogenide nanowires, are attractive for spintronics and valleytronics due to their unique physical and chemical properties resulting from low dimensionality. Emerging concepts of spintronics devices will greatly benefit from using 1D and 2D materials, which opens up new ways to manipulate spin. A majority of 1D and 2D materials is non-magnetic, thus their applications in spintronics are limited. The exploration, design and synthesis of new 1D and 2D materials with intrinsic magnetism and high spin-polarization remains a challenge. In addition, the valley polarization and spin-valley coupling properties of 2D materials have attracted great attention for valleytronics, which not only manipulates the extra degree of freedom of electrons in the momentum space of crystals but also proposes a new way to store the information.

The computational investigation of magnetic and electronic properties of low-dimensional materials is the subject of this thesis. We have systematically investigated geometric, electronic, magnetic and valleytronic properties of several 2D and 1D materials by using the density functional theory. These investigations not only theoretically show rich and adjustable magnetic properties of low-dimensional materials but also provide a future perspective on those materials for spin and valley logic devices. Unique magnetic properties of three different types of MXenes, Vanadium tetrasulfide ($VS_4$) nanowires (NWs) and Janus transition metal dichalcogenides (TMDs) have been investigated, and they show great potential applications in spintronics or valleytronics. The main results of relevant low-dimensional materials from this thesis are summarized as below:

***Bipolar antiferromagnetic MXenes:*** Antiferromagnetic (AFM) spin devices can be one type of spintronics due to resistance to magnetic field perturbation. However, detecting and manipulating the spin of AFM materials is still a major challenge due to spin degeneracy in the band structure. Bipolar antiferromagnetic semiconductors (BAFS) are promising solutions to these problems. We present asymmetrical functionalized double MXenes ($Cr_2TiC_2FCl$) that behave as a BAFS with vanishing magnetism, in which the valence band and conduction band around the Fermi level exhibit opposite spin directions. The gate voltage can manipulate the

spin orientation of $Cr_2TiC_2FCl$ MXene and can lead to a magnetic transition from BAFS to half-metallic antiferromagnetism (HMAF). Moreover, mixed functionalized $Cr_2TiC_2$ MXenes with various F and Cl concentrations show adjustable BAFS features due to the different chemical environment for Cr atoms. Our results show a new strategy towards AFM spintronics and the realization of the AFM spin field effect transistor

***Bimetallic and vacancy-ordered MXenes:*** Magnetic *i*-MXenes ("*i*" means in-plane ordering) are one type of 2D transition metal carbides with high potential for spintronics. Structural, electronic and magnetic properties of bimetallic and vacancy-ordered MXenes derived from a new $(V_{2/3}Zr_{1/3})_2AlC$ MAX phase have been investigated. In particular, we have investigated the properties of pristine and surface-functionalized $(V_{2/3}Zr_{1/3})_2CX_2$ bimetallic and $(V_{2/3}\square_{1/3})_2CX_2$ (where $\square$ denotes the vacancies) vacancy-ordered MXenes with X = O, F and OH. The results show that modifying the MXene stoichiometry and/or MXene surface functionalization changes MXene properties. $(V_{2/3}Zr_{1/3})_2CX_2$, $(V_{2/3}\square_{1/3})_2CF_2$ and $(V_{2/3}\square_{1/3})_2C(OH)_2$ MXenes are stable structures. Among them, $(V_{2/3}Zr_{1/3})_2CO_2$ MXene is predicted to be an intrinsically ferromagnetic (FM) half-semiconductor with a high Curie temperature ($T_C$) of 270 K. Moreover, the adjustable work function (WF) of *i*-MXenes suggests that they are candidate for electronic devices. These theoretical predictions of *i*-MXene properties motivate further experimental research towards developing spintronics devices.

***Magnetic MXenes for valleytronics:*** 2D valleytronics, using the valley index of carriers to perform logic operations, serves as the basis of the next-generation electronic devices. Breaking inversion symmetry of 2D hexagonal lattices is the precondition to generate the valley degree of freedom. The inversion symmetry of MXenes can be naturally broken with surface functionalization. Therefore, we first proposed a general strategy to induce intrinsic ferrovalley polarizations for magnetic MXenes by surface-engineering driving. Our results indicate that Janus $Cr_2COX$ (X= F, Cl and OH) MXenes are FM semiconductors (or half-metals) with the robust spin polarization and high $T_C$ above the room temperature. According to Berry curvatures calculations, $Cr_2COX$ MXenes belong to the family of valley Hall materials. In particular, $Cr_2COF$ MXene as the optimal candidate of ferrovalley materials has the strong valley polarization of 334 meV and the high $T_C$ of 1146 K. Moreover, among $Cr_2CO_{2-x}F_x$ ($0 < x < 2$) MXenes, $Cr_2CO_{0.75}F_{1.25}$ and $Cr_2CO_{1.25}F_{0.75}$ are also show valley polarizations and high

$T_C$. Therefore, Janus and mixed functionalized $Cr_2C$ MXenes can be used as room-temperature valleytronics devices. In addition, the valley polarization also exhibits in other MXenes, for example the bipolar antiferromagnetic $Cr_2TiC_2FCl$ MXene. Our work not only investigates the fundamental principle of the valley polarization in functionalized MXenes, but also provides an experimentally workable approach (i.e. surface-engineering) for exfoliated MXenes.

.***1D magnetic NWs:*** Quasi 1D $VS_4$ NWs are synthetic semiconductors which forms bundles through Van der Waals interactions. Our simulations of their stability indicate that $VS_4$ NWs can be separated from their bulk phases. We theoretically investigated the geometrical, electronic, and magnetic properties of bulk phase and isolated $VS_4$ NWs. Our results indicate that both bulk phase and isolated $VS_4$ NWs are AFM semiconductors. These calculations also suggested that isolated $VS_4$ NWs show HMAF upon electron and hole doping because carriers doping can split the spin degeneracy to induce a small local spin polarization. Spin polarization currents in isolated $VS_4$ NWs can be manipulated by applying gate voltages. Therefore, these 1D AFM materials have a high potential for improving both fundamental research and spintronics applications.

***Janus magnetic TMDs:*** 2D TMDs have been widely explored due to their extraordinary physical properties and potential device applications. The Janus MoSSe monolayer has been successfully synthesized by replacing the top-layer S with Se atoms of $MoS_2$, but is non-magnetic. Therefore, we proposed these intrinsic 2D ferromagnetic Janus TMDs monolayer (TMXX', TM= V, Cr and Mn; X, X' = S, Se and Te, $X \neq X'$) with large spin-polarization and high $T_C$. In particular, MnSSe monolayer shows half-metal with 100% spin polarization and wide half-metallic gap. Our work presents a new type of 2D magnetic materials for spintronics applications.

# Abstrakt

Nízkorozměrné struktury, jako například grafen, dvourozměrné chalkogenidy tranzitních kovů či jednorozměrná vlákna chalkogenidů, jsou atraktivní pro jejich potenciální aplikace ve spintronice a valleytronice a to právě kvůli vlastnostem vyplývajícím z nízkorozměrné struktury. Nové koncepce v elektronice a spintronice se opírají o využití jednorozměrných (1D) a dvourozměrných (2D) struktur. Většina 1D a 2D struktur není magnetická, což představuje významnou překážku k přímočarým aplikacím ve spintronice. Je proto pochopitelné, že objevování nových nízkorozměrných magnetických struktur je velkou výzvou současné materiální chemie a fyziky. Velkou výzvou je rovněž valleytronika, která přináší nové možnosti ukládání informací.

Předmětem předkládané práce je teoretické studium magnetických a elektronických vlastností nízkodimenzionálních struktur. Geometrické, elektronické a magnetické vlastnosti několika tříd 2D a 1D materiálů byly zkoumány pomocí metod funkcionálu hustoty (DFT). V práci je popsána řada nových materiálů s širokou škálou magnetických vlastností a ukazuje na možné způsoby jejich budoucího využití. Mez popisované materiály patří 2D MXeny, 1D nanovlákna tetrasulfidu vanadu a 2D nesymetricky substituované (Janus) dichalkogenidy, které všechny vykazují parametry požadované k aplikacím ve spintronice. Hlavní výsledky této práce jsou stručně shrnuty pro jednotlivé třídy studovaných materiálů:

***Bipolární antiferomagnetické MXeny:*** Antiferomagnetické materiály jsou vhodné pro využití ve spintronice díky své rezistenci ke změnám magnetického pole. Detekce a manipulace spinu v AFM materiálech je ovšem komplikována spinovou degenerací v pásové struktuře. Bipolární antiferomagnetické polovodiče (BAFS) nabízí řešení zmíněného problému. V práci popisujeme vlastnosti asymetricky funkcionalyzovaného MXenu $Cr_2TiC_2FCl$, ve kterém valenční a vodivostní pásy vykazují v blízkosti Fermiho hladiny opačný spin. Orientaci spinů je možné kontrolovat pomocí vloženého napětí a je možné vyvolat přechod z BAFS do polokovového antiferomagnetického (HMAF) stavu. Naše studie také ukazuje možnost optimalizace BAFS charakteristik jednoduše změnou relativních koncentrací povrchových funkčních skupin (atomů F a Cl). Práce tak ukazuje nové cesty směrem k realizaci AFM spinových tranzistorů.

***Bimetalické MXeny a MXeny s uspořádanými vakancemi:*** Pro aplikace ve spintronice mají rovněž velký potenciál bimetalické 2D karbidy tranzitních kovů (označované *i*-MXeny), ve kterých jsou tranzitní kovy uspořádány v rámci jednotlivých vrstev. Strukturní, elektronické a magnetické vlastnosti bimetalických *i*-MXenů a MXenů s uspořádanými vakancemi byly studovány pro třídu materiálů odvozenou od $(V_{2/3}Zr_{1/3})_2AlC$ 3D materiálu (označovaného „MAX“ fáze). Studovány byly následující materiály: bimetalický $(V_{2/3}Zr_{1/3})_2CX_2$ a $(V_{2/3}\square_{1/3})_2CX_2$ (□ označuje vakanci) *i*-MXene s uspořádanými vakancemi, v obou případech pro X = O, F a OH. Studie ukazuje, jakým způsobem se mění magnetické vlastnosti těchto 2D materiálů v závislosti na stechiometrii obou kovů a stechiometrii vakancí. Bylo ukázáno, že $(V_{2/3}Zr_{1/3})_2CX_2$, $(V_{2/3}\square_{1/3})_2CF_2$ and $(V_{2/3}\square_{1/3})_2C(OH)_2$ MXeny jsou stabilní struktury. $(V_{2/3}Zr_{1/3})_2CO_2$ MXene je feromagnetický polo-polovodič vykazující tyto magnetické vlastnosti i za pokojové teploty ($T_C$=270 K). Kromě toho mohou být materiály z této třídy využity v elektronice díky relativně snadno laditelné (pomocí povrchových funkčních skupin) výstupní práci.

***Magnetické MXeny pro valleytroniku:*** 2D materiály vhodné pro valleytronické aplikace vykazují dodatečný stupeň volnosti (index údolí), který lze využít pro ukládání informací. Podmínkou pro takové vlastnosti je porušení inverzní symetrie 2D hexagonální mříže. V případě MXenů může být inverze přirozeně porušena vhodnou funkcionalizací povrchu. Naše studiu ukazuje, jak lze vybudit vnitřní polarizaci magnetických MXenů pomocí chemické modifikace povrchů. Výsledky ukazují, že nesymetricky funkcionalizované $Cr_2COX$ (X = F, Cl a OH) MXeny jsou FM polovodiče (případně polokovy) s významnou spinovou polarizací a vysokou $T_C$. Pomocí výpočtů Berryho fáze lze ukázat, že tyto MXeny patří do třídy Hallových materiálů, v tomto případě v novém stupni volnosti. Optimálním kandidátem pro aplikace je $Cr_2COF$ MXene vykazující silnou polarizaci údolí (334 meV) a extrémně vysokou $T_C$=1146 K. I další MXeny funkcionalizované F a O ($Cr_2CO_{2-x}F_x$) vykazují dostatečnou polarizaci údolí a vysoké $T_C$. Nejen perfektně asymetrické MXeny, ale i částečně asymetrické MXeny mohou být využity pro aplikace za pokojových teplot. Polarizace údolí byla nalezena i pro další MXeny, například pro $Cr_2TiC_2FCl$ bipolární AFM. Naše práce objasňuje základní principy polarizace údolí ve funkcionalizovaných MXenech a rovněž ukazuje experimentálně slibnou cestu k materiálům vhodným pro valleytroniku.

***1D magnetická nanovláklna:*** Syntéza kvazi-jednodimenzionálních $VS_4$ nanovláken (NW) byla reportována v literatuře. Tato nanovlákna tvoří svazek vykazující polovodičové vlastnosti. Naše výpočty naznačují, že by mělo být možné separovat individuální 1D molekuly ze svazku a že rovněž individuální vlákna jsou AFM polovodiče. Výpočty rovněž ukazují, že NW dopovaná elektrony či elektronovými dírami vykazují HMAF charakteristiky a to v důsledku odstranění spinové degenerace. Spinová polarizace v izolovaných $VS_4$ NW závisí na vloženém potenciálu. Ze všech výše uvedených důvodů lze usuzovat, že 1D AFM materiály mají obrovský potenciál pro budoucí aplikace ve spintronice.

***Nesymetricky substituované (Janus) magnetické dichalkogenidy přechodných kovů (TMD):*** 2D TMD jsou předmětem intenzivního zájmu v důsledku jejich mimořádných fyzikálních vlastností. Nesymetricky substituovaná MoSSe mono vrstva byla úspěšně připravena experimentátory náhradou S atomů v horní vrstvě atomy Se. Tento konkrétní 2D TMD ovšem nevykazuje magnetické vlastnosti. V naší práci jsme navrhli a výpočetně charakterizovaly nesymetricky substituované TMXX' (TM=V, Cr a Mn; X, X' = S, Se a Te) vykazující velkou spinovou polarizaci a vysoké $T_C$. Například MnSSe mono vrstva vykazuje charakteristiky polokovu se 100% spinovou polarizací. Naše teoretická práce tak otevírá cestu k nové třídě materiálů s vysokým aplikačním potenciálem.

# List of the Abbreviations

| | |
|---|---|
| AFM | Antiferromagnetic |
| AIMD | *ab initio* Molecular Dynamics |
| BAFS | Bipolar Antiferromagnetic Semiconductor |
| BMS | Bipolar Magnetic Semiconductors |
| CBM | Conduction Band Minimum |
| DFPT | Density Functional Perturbation Theory |
| DFT | Density Functional Theory |
| DFT+U | Density Function Theory Plus Hubbard U |
| nD | n Dimensional |
| DOS | Density of states |
| ELF | Electron Localization Functions |
| FET | Field Effect Transistors |
| FIM | Ferrimagnetic |
| FM | Ferromagnetic |
| GGA | Generalized Gradient Approximation |
| HMAF | Half-metallic Antiferromagnetism |
| HMF | Half-metallic Ferromagnets |
| HSC | Half Semiconductors |
| HSE | Heyd-Scuseria-Ernzerhof functional |
| LDA | Local Density Approximation |
| MXene | Two-dimensional Transition Metal Carbide/Nitride/Carbonitride |
| NW | Nanowire |
| PBE | Perdew-Burke-Ernzerhof functional |
| PDOS | projected density of states |
| QAHE | Quantum Anomalous Hall Effect |
| QAVHE | Quantum Anomalous Valley Hall Effect |
| QSHE | Quantum Spin Hall Effect |
| QVHE | Quantum Valley Hall Effect |

| | |
|---|---|
| SGS | Spin Gapless Semiconductors |
| SHE | Spin Hall Effect |
| SOC | Spin Orbital Coupling |
| TM | Transition Metal |
| TMC | Transition Metal Chalcogenides |
| TMD | Transition Metal Dichalcogenides |
| VBM | Valence Band Maximum |
| vdW | van der Waals |
| $VS_4$ | Vanadium Tetrasulfide |
| WF | Work Function |

# CHAPTER 1. Introduction

Low-dimensional (1D and 2D) materials[1-3] have unusual optical, electronic and magnetic properties due to the effect of dimensionality[4]. The scientific research of layered materials has a history of more than 150 years. Researchers realized the true potential of these layered materials in advanced technological applications[5]. When layered materials thin to its physical limit, the monolayer of those layered materials exhibits new characteristics different from corresponding 3D bulk phase[6]. With the rapidly growing field of nanomaterials and nanodevices, 2D materials have drawn great attention due to their distinctive and tunable electronic, optoelectronic, and magnetic properties[7]. Perspective 2D materials include graphene[8], graphyne[9], silicene[10], phosphorene[11], boronene[12], and transition metal chalcogenides (TMCs)[13]. With the rapid development of materials science, electronics and spintronics, previously impossible experiments can be carried out and the fundamental theory can be tested by using novel 2D materials (**Figure 1.1**). In addition, (quasi-)1D materials, including nanoribbon[14], nanowire[15], nanotube[16], etc., also show great potential in electronics and spintronics due to their dimensionality and structures flexibility.

MXene[17, 18] is chemically exfoliated from its bulk phase, MAX, in which M is a transition metal, A is A-group element (for example Al and Si), and X is carbon or nitrogen. In a 2D layer of MXene, n + 1 (n = 1−4) layers of transition metals are interleaved with n layers of carbon or nitrogen, with a general formula of $M_{n+1}X_nT_x$. $T_x$ in the formula represents the surface functionalizations, such as O, OH, F, and/or Cl elements, which are bonded to the outer M layers. The first MXene ($Ti_3C_2T_x$) was discovered at Drexel University in 2011[19]. Up to now, more than 70% of all MXene research has focused on $Ti_3C_2T_x$[20]. Many new compounds have been synthesized in this sub-family of MXenes[21]. The hot-topic for synthesizing new ordered MXenes has brought excitement to the MAX phase research[17]. Researchers who are working on MAX phases have started to develop new MXene precursors, not only the MAX phases but also other layered carbides and nitrides. Since 2017, researchers have synthesized around 30 new ordered double transition metal MAX phases (MM'AX) and explored their properties[22, 23]. Moreover, in-plane ordered MAX (*i*-MAX) phases have been synthesized, $(Mo_{2/3}Sc_{1/3})_2AlC$ and $(V_{2/3}Zr_{1/3})_2AlC$ phases[24, 25]. The $(Mo_{2/3}\square_{1/3})_2C$ ($Mo_{1.33}C$) was also

synthesized ("□" means vacancy defects), namely *i*-MXene[26, 27]. It is important to keep searching and discovering new MAX structures and compositions, which provides support to exfoliate new MXenes. MXenes have a unique combination of properties[17], including the high electrical conductivity, efficient absorption of electromagnetic waves, and abundant functional groups which have led to a large number of applications[28, 29], such as batteries, energy storages, catalysis, photo detectors, sensors, electronics, and spintronics, as well as electromagnetic interference shielding and printable antennas. In spintronics fields, including electronic and spintronic applications, most of investigations are theoretical works with relatively few experimental works, such as magnetic semiconductors and topological insulators[30-32]. To date, at least 100 stoichiometric MXene compositions and an unlimited number of solid solutions offer not only a way to adjust their structures by changing the ratio of M or X elements, but also their unique combinations of properties [23]. Therefore, the large number of unexplored MXene and their unique properties opens the door to their potential applications. The possibility of new MXenes suggests that we are still in the early stages of MXene research.

2D transition metal dichalcogenides (TMDs)[33, 34] are mostly semiconductors of the $MX_2$ type. M is a transition metal atom (such as Mo and W) and X is a chalcogen atom (S, Se and Te). $MoS_2$ is the most studied material in TMDs due to its stability and unusual electronic and optical properties[35]. TMDs generally exhibit the strong spin-orbital coupling (SOC) effect and favorable electronic and mechanical properties, which has attracted wide attention for their applications in electronics, spintronics, optoelectronics, and valleytronics[36, 37]. Most TMDs are intrinsically non-magnetic (except for $VX_2$, $CrX_2$ and $MnX_2$). The adsorption, vacancy, tensile strain, and hydrogenation have been performed for inducing the magnetism and spin-polarization in TMDs[13, 38]. However, such approaches are still great challenge to realize experimentally ordered spin structures and high magnetic transition temperatures due to the cluster effects of absorbed atoms and uncontrolled distribution of defect and dopant as well as the large strain requirement. For these reasons, the search for 2D magnetic TMDs is of great importance for both fundamental interest and device applications but it remains a challenge. In addition, a synthetic strategy of growing Janus monolayers of TMDs[39, 40] with broken the out-of-plane structural symmetry was achieved by the top-layer S atoms being fully replaced

with Se atoms. However, Mo/W-based Janus TMDs have no intrinsic magnetism. Therefore, the design and exploration of Janus TMDs with intrinsic magnetism and high spin-polarization is important for their applications in electronics and spintronics.

The scientific achievements resulting from 2D materials suggest that relevant new physics exists in the few-chain to single-chain limit of 1D materials. Extending to 1D wired materials is also exciting but remains challenging. There are 1D materials with atomic structures of TMCs[15], including $MX_3$, $MX_4$, and $M_6X_6$ (M = transition metal, X = chalcogen). For example, the $M_6X_6$ wires can be stacked parallelly into a hexagonal crystal with van der Waals (vdW) interaction between each other[41]. $M_6X_6$ wires have well-defined electronic structures and physical properties for a given stoichiometry, which is a distinct advantage for practical applications. Some of these wires have been already synthesized[42]. Based on the high-throughput calculations [15], 53 $M_6X_6$ wires were identified as experimentally feasible. Six of them are robust ferromagnetic (FM) nanowires with high Curie temperatures ($T_C$). Moreover, these $M_6X_6$ atomic wires possess high stability and resistance to oxidation, which are desirable for device applications. Moreover, the previous investigation reported that Vanadium tetrasulfide ($VS_4$) as a quasi-1D compound (thin films) can be synthesized with promising properties for energy conversion applications[43]. Furthermore, the quasi-1D $NbSe_3$ in the few-chain limit have been synthesized and single chains were isolated[44]. Those $NbSe_3$ chains can be encapsulated in protective boron nitride (or carbon) nanotubes to prevent oxidation and to facilitate characterization. Consequently, the large family of 1D materials with definite structures and rich magnetic properties remains to be explored for flexible electronics and spintronics.

## 1.1 Spintronics

Information technology is an important issue for the development of modern science and technology[45]. The end of conventional charge-based electronics will come in the near future along with the Moores' law gradually losing its effect[46, 47]. Therefore, developing high speed and low energy consuming information technology is an urgent need. Many methods and techniques[48-50] of molecular electronics, electronics, spintronics, quantum information technology were proposed, with spintronics being one of the most promising approaches[51].

Spintronics[52, 53], which stores information by manipulating the spin degree of freedom of electrons, is compatible with conventional electronics. Therefore, many techniques in traditional electronics can be extended to spintronics[54, 55]. Different from traditional electronics to manipulate charge, spintronics focus on controlling the spin. Under ideal conditions, there is a pure spin current and no charge current in the spintronic circuit, so no heat is generated or wasted. Moreover, information can be transmitted at a high speed due to the spin coherence effect[56]. Spintronic devices were deriving from the discovery of giant magnetoresistance[57] and the subsequent development of spin valves. Any spin current is carried by two types of carriers, namely spin-up (majority) and spin-down (minority). In general, logical "1" (i.e., the high-resistance state) and logical "0" (i.e., the low-resistance state) can be represented by the antiparallel configuration and the parallel configuration of two ferromagnetic layers, respectively. Up to now, the spin valve serves as the basic building block for advanced spintronic devices[56, 58].

The control and detection of the spin order of FM materials[59-63] is the main principle of current magnetic information storage and reading technology. Scientists have designed a variety of spintronic materials (**Figure 1.1**). Spintronic materials can be classified into magnetic metals, topological insulators (TIs) and magnetic semiconductors according to their electron and magnetic properties[64]. In spintronic circuits, magnetic metals and TIs can be used as spin sources and spin drains, while magnetic semiconductors can form the central area of the device. In each of these components, spin manipulation and detection can be carried out depending on the coupling of spin to light, magnetic or electric fields. In general, practical spintronic materials should have a strong magnetic order at room temperature (*i.e.* their magnetic order temperature should be significantly higher than room temperature). At the same time, there is a large spin polarization near the Fermi energy level. Such FM metals include iron, cobalt and nickel metals and their alloys[65]. They are the oldest materials for spintronics and are used to build spin valves and magnetic tunnel junctions[55]. These materials are abundant, inexpensive and easy to handle. However, due to their low spin polarizations, they can only provide partially spin-polarized carriers. For the reason, half-metallic ferromagnets (HMFs) can be used for pure spin generation and injection[66, 67]. For HMFs, one spin channel is metallic state while the other spin channel is semiconducting (or insulating). Thus, the 100% spin polarization can be

obtained in HMFs, which can provide single and pure spin electrons. In order to develop practical spintronic devices containing HMFs with high ferromagnetic $T_C$, the semimetallic gap should be wide enough to effectively prevent thermally stirred spin-flip transitions and to maintain semimetallicity at room temperature[68, 69].

On the other hand, magnetic semiconductors can combine the properties and advantages of magnets and semiconductors to form the basis of spintronics and can be used for spin generation and injection, as well as for spin manipulation and detection[70, 71]. Magnetic semiconductors can be divided into two types: diluted magnetic semiconductors[72] and intrinsic magnetic semiconductors[73, 74]. Based on different electronic and magnetic properties, intrinsic magnetic semiconductors can be divided into half semiconductors (HSCs), spin gapless semiconductors (SGSs), bipolar magnetic semiconductors (BMSs), and so on[64].

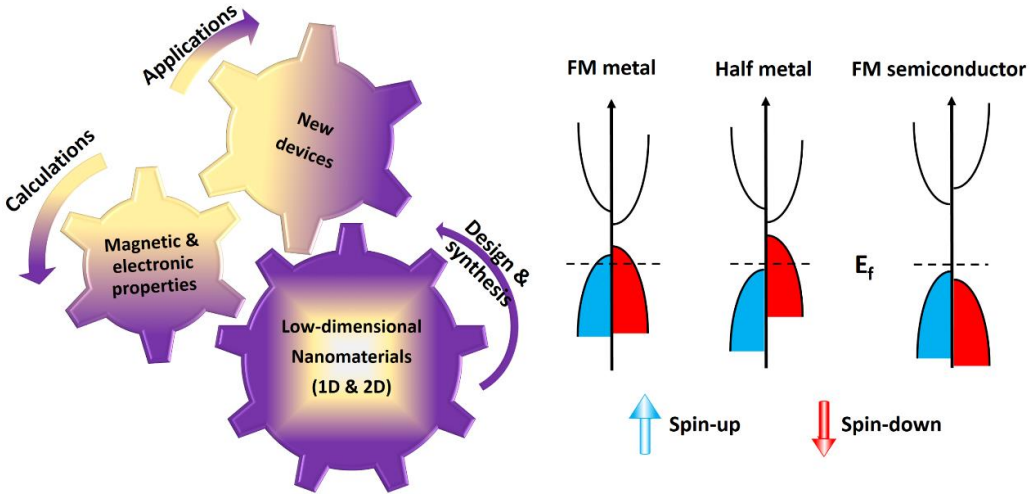


**Figure 1.1** Schematic plot of design and synthesis different spintronics materials (Left) and electronic structures for various ferromagnetic materials in spintronics (Right).

In addition to FM materials, antiferromagnetic (AFM) materials have some attractive properties, but they were rarely used. Because the internal net magnetic moment is zero, magnetism in AFM materials externally invisible. The zero magnetization of antiferromagnetic ordering and the lack of stray magnetic fields can eliminate interference between adjacent devices[75-77]. However, the spin manipulation in antiferromagnets requires extremely high magnetic fields. Traditional magnetic probes cannot detect AFM orders, therefore the information stored in AFM moment cannot be read. In recent years, scientists have found that

the electromagnetic radiation can be used to detect and modify the AFM order[78], which opens up a new opportunity for AFM spintronics and makes AFM materials potentially attractive in basic and applied investigations. In addition, AFM materials have been primarily manipulated for spintronics by inducing half-metallic antiferromagnetism (HMAF)[79]. HMAF materials were first proposed in Heusler compounds[80, 81], more specifically CrMnSb, could be fully spin-compensated half-metallic materials[82]. HMAF materials can be obtained from AFM materials by carrier doping or electric fields[83]. Although FM and AFM spintronics has huge potential advantages, it still faces many challenges, such as spin-polarized carrier (pure spin) generation and spin injection, long-distance spin transport, spin manipulation and detection, and so on[84, 85]. Meanwhile, the spin scattering at the metal-metal or metal-semiconductor interface is also important, because it directly affects the spin transport length (*i.e.* spin lifetime)[86]. The solution of these problems depends on the development of device manufacturing technology and the design of new spintronics materials with specifically electronic and magnetic properties.

Thanks to the discovery of graphene, the long distance spin transport is expected to be achieved in the near future[87]. In the past decade, the field of graphene spintronics exhibited many significant advances, such as spin injection, defect-induced magnetism, the intrinsic and extrinsic SOC, and so on[88]. The spin transport in the large-area graphene has been achieved by chemical vapour deposition, which is a key step for graphene spintronics at the large-scale[51]. These graphene-based devices exhibited longer spin diffusion lengths (exceeding several micrometers) and longer spin lifetime[89]. However, the graphene does not have *d* (or *f*) electrons, so the formation and control of magnetic moment in the graphene is non-trivial. Possible methods for tunable magnetism in the graphene include gating, doping, functionalization, and external fields (*e.g.* electric fields and FM substrates). There are many theoretical and experimental investigations of magnetic moments in graphene, such as vacancy defects, light adatoms functionalization (such as H and F), heavy adatoms (such as 3*d*, 4*d* and 5*d* elements), FM substrates supporting and molecular doping[51, 90]. Magnetic moments are also predicted to form at the graphene edges (zigzag nanoribbons)[91]. However the spin interaction of 2*p* electrons is still weak and external fields may be not easy controlled. Therefore,

the design and synthesis of low-dimensional materials with intrinsic magnetism remains a challenge.

In addition, SOC is an essential spin interaction, destructive for the spin coherence and is usually responsible for spin relaxation. Because of the weak SOC, the graphene can has a long spin coherence length up to a few micrometers, thus are ideal spin transportation materials. As with most graphene properties, SOC can be tuned and controlled by light, magnetic field, electric field, etc[92]. Moreover, SOC can also lead to many interesting phenomena, such as the spin Hall effect (SHE)[93-95], quantum spin Hall effect (QSHE)[96], quantum anomalous Hall effect (QAHE)[97], and even strongly modifying the plasmon spectrum[98].

According to the above, the design of new spintronics materials with specifically electronic and magnetic properties is a great way to explore physically and chemically fundamental principles, as well as their potential applications.

## 1.2 Valleytronics

Valleytronics as an emerging field will becomes a potential candidate for the next generation of electronic devices[99, 100]. The electronic band structure into crystalline systems determines the relationship between the crystal momentum and energy of electrons. In intrinsic semiconductors, the Fermi level lies between two bands, in which valence band maximum (VBM) below the Fermi level and conduction band minimum (CBM) above the Fermi level determine the electronic, magnetic, and optical properties. These extremes are known as the "valleys" (also named pseudospin) of the crystal momentum space and are stable points in the energy band structure that an electron or hole can occupy[101]. Thus, in addition to charge and spin, electrons in a crystal also have a valley degree of freedom, which determines the position of electrons in the crystal momentum space[102]. The field of valleytronics seeks to use the valley degrees of freedom of electrons to encode and process information (similar to the charge or spin in an electron). One of the motivations for research in valleytronics (and spintronics) is its application to low-energy information storage and processing devices. For example, pure valley (or spin) currents offer the possibility of carrying valley (or spin) information without the ohmic heating associated with charge currents[102-105].

It is difficult to dynamically control the valley degree of freedom in a variety of bulk semiconductors (*e.g.*, silicon). On the contrary, 2D material systems exhibit valleys with contrasting physical properties[106]. In particular, 2D hexagonal lattice materials, such as graphene, hexagonal boron nitride, and TMDs, can storage information by manipulating the band structure consisting of two valleys at the $K^+$ and $K^-$ (or marked as K and K') points in crystal momentum space[106]. For instance, the inversion symmetry that is intrinsic in graphene requires that the $K^+$ and $K^-$ valleys are indistinguishable. However, when this inversion symmetry is broken (*e.g.* externally applied fields), the valleys become distinguishable. Materials with broken inversion symmetry show a lot of valley dependent physical effects. Monolayer TMDs lack inversion symmetry and naturally possess valley-contrasting physical effects (**Figure 1.2**). One of the most important valley effects is the valley-dependent optical selection rule in monolayer TMDs, which provides a simple way to write and read valley-dependent signals by addressing specific valleys. This selection rule requires that normal-incidence (left or right) circularly polarized light of a given helicity only couples to an optical transition in one valley[107-109]. Therefore, the selection rule is a consequence of the valley structure in the momentum space and broken inversion symmetry. In addition, the strong SOC in monolayer TMDs lead to a locking effect between the spin and valley. The valley polarization is realized in a monolayer TMD accompanied by the spin polarization. Moreover, monolayer TMDs also exhibit the quantum valley Hall effect (QVHE) that results in the accumulation of valley polarization on two opposite edges during electrons (or holes) transport. The QVHE is derived from the opposite (non-zero) Berry curvature in inequivalent valleys. The Berry curvature acts like a magnetic field in crystal momentum space. The electrons (and holes) in inequivalent valleys accumulate on opposite edges of TMDs, resulting in a valley current in the transverse direction.

The major challenge of manipulating the valley index in valleytronics is to break the degeneracy between two valleys to achieve the valley polarization[110]. At the present stage, applying external fields have been performed to induce the valley polarization, such as external electric and magnetic fields. However, a sizable valley polarization requires a very strong field, which is hard to achieve in practical applications[111-113]. Other methods, such as magnetic atoms doping and magnetic supports, were also considered[114]. While all of the above

physical attempts are limited for data devices. The valley polarization is extrinsic and can disappear once the external fields are removed[101]. The valley polarization degenerates into the initial non-polarization state, resulting in disadvantages of practical applications. The ferrovalley materials with spontaneous valley polarization were for the first time unveiled in 2D 2H-$VSe_2$[115, 116], paving a way towards practical applications of valleytronics (**Figure 1.2**). The additional charge Hall current is derived from the spontaneous valley polarization in ferrovalley materials, namely quantum anomalous valley Hall effect (QAVHE)[115]. The electrically readable and magnetically writable memory devices based on the QAVHE in ferrovalley materials are rapidly developing. The binary logic states are stored by the valley polarization, which can be controlled by external magnetic field. It can be easily read out by measuring the sign of the transverse Hall voltage. Therefore, the memory applications based on the ferrovalley materials can innovate storage technology and can develop next-generation electronic devices. Up to now, majority 2D materials were not synthesized yet or their valleytronics properties were not demonstrated. Therefore, the valleytronics research is still at its early stage.

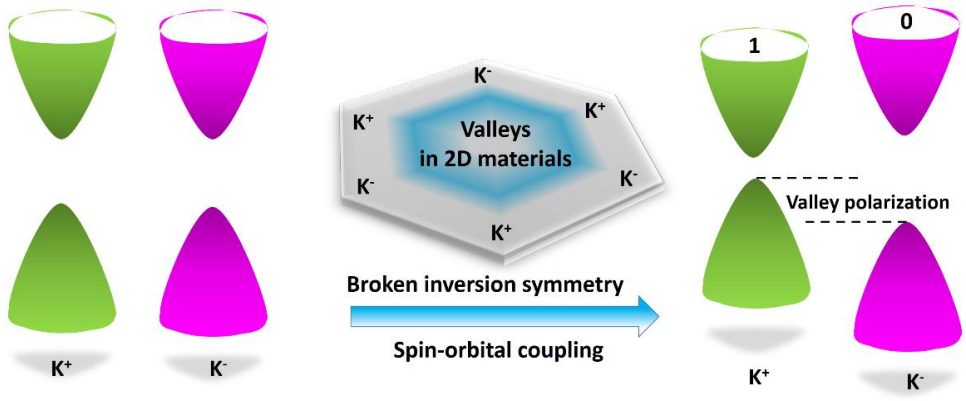


**Figure 1.2** Schematic plot of valley polarization in the 2D FM hexagonal crystal. The valley polarization can be induced with broken inversion symmetry and SOC. logical "1" and "0" suggest that the information can be stored and manipulated in different valleys.

The rest of the thesis is organized into the following sections: after the introduction given in this Section, computational methods used are briefly described in the Section 2, including specific technical details. The results are reported in Section 3, including FM and AFM MXenes

in spintronics and valleytronics, AFM nanowire in spintronics, and Janus TMDs in spintronics. Discussions and conclusions are provided in Section 4 and Section 5, respectively. Our investigations not only provide useful hints for experimentalists to design and to develop low-dimensional materials in spintronics, but also highlight so far neglected applications of MXenes in valleytronics. In short, we theoretically predict and design low-dimensional materials with specific properties that will direct experimental research. We aim to facilitate research into low-dimensional materials with high potential for spintronics and valleytronics applications. We believe that the reported results are highly relevant from both a theoretical and practical perspectives.

# CHAPTER 2. Methods

Low-dimensional materials were investigated using first-principle calculations. All electronic-structure calculations were performed at the density functional theory (DFT) level. This section briefly describes relevant methods used in this thesis.

## 2.1 DFT methods

The quantum chemical methods is to approximate the solution of the time-independent, non-relativistic Schrödinger equation[117]:

$$\hat{H}\Psi\left(x_1,\cdots x_N,R_1,\cdots R_M\right)=E\Psi\left(x_1,\cdots x_N,R_1,\cdots R_M\right) \tag{2.1}$$

where $\hat{H}$ is the Hamiltonian of a molecular system without external fields, containing *M* nuclei and *N* electrons. $\Psi$ is a wave function of this system. $\hat{H}$ (in atomic units) is described as:

$$\hat{H}=-\frac{1}{2}\sum_{i=1}^{N}\nabla_i^2-\frac{1}{2}\sum_{A=1}^{M}\frac{1}{M_A}\nabla_A^2-\sum_{i=1}^{N}\sum_{A=1}^{M}\frac{Z_A}{r_{iA}}+\sum_{i=1}^{N}\sum_{j>i}^{N}\frac{1}{r_{ij}}+\sum_{A=1}^{M}\sum_{B>A}^{M}\frac{Z_AZ_B}{R_{AB}} \tag{2.2}$$

where *A* and *B* sum over *M* nuclei and *i* and *j* sum over *N* electrons in the system. The first two terms express the kinetic energy of electrons and nuclei, respectively. The third term expresses the attractive (electrostatic) interaction between electrons and nuclei. The fourth and fifth terms express the electron-electron and nucleus-nucleus repulsion interaction, respectively.

The motion of electrons can be considered to take place in the field of fixed nuclei due to electrons moving much faster than nuclei, which is Born-Oppenheimer approximation[118]. Then the electronic Hamiltonian is approximately described as:

$$\hat{H}_{elec}=-\frac{1}{2}\sum_{i=1}^{N}\nabla_i^2-\sum_{i=1}^{N}\sum_{A=1}^{M}\frac{Z_A}{r_{iA}}+\sum_{i=1}^{N}\sum_{j>i}^{N}\frac{1}{r_{ij}} \tag{2.3}$$

The electronic wave function $\Psi_{elec}$ and the electronic energy $E_{elec}$ can be obtained from the following electron-only Schrödinger equation:

$$\hat{H}_{elec}\Psi_{elec}=E_{elec}\Psi_{elec} \tag{2.4}$$

The total energy of a system is the sum of $E_{elec}$ and the constant nuclear repulsion term:

$\sum_{A=1}^{M}\sum_{B>A}^{M}\frac{Z_A Z_B}{R_{AB}}$.

The traditional wave function theory depends on the wave functions with 4*N* coordinates (3*N* spatial and *N* spin coordinates of electrons) to solve Schrödinger equations. It is very costly for large systems. In turn, DFT only considers the total electron spin-densities which depend only on 8 coordinates. It is therefore convenient to investigate crystals, not just small molecules. In addition, it is practically easier to take electron correlation into account in DFT, although practically many approximations are required.

The entire field of DFT rests on two fundamental mathematical theorems proved by Hohenberg and Kohn[119]. In general, the relationship between electron density $n(r)$ and ground state wave function $\Psi$ is:

$$\rho(r)=\int ds_1 dx_2\cdots dx_N \Psi^*\left(x_1,x_2,\cdots,x_N\right)\Psi\left(x_1,x_2,\cdots,x_N\right) \tag{2.5}$$

The first HK theorem demonstrates that the external potential $V_{ext}$ (constants) and the total energy of an N-electron system is uniquely determined by electron density $n(r)$ of its system.

The second HK theorem demonstrates that the ground state energy can be variationally obtained: the density that minimizes the total energy is the exact ground state density. To obtain the total energy by using variational principle[117], a universal functional $F_{HK}[\rho(r)]$, valid for any external potential $V_{ext}$, is defined as,

$$F_{HK}[\rho]=T[\rho]+E_{ee}[\rho]=\Psi_\rho\left|T+V_{ee}\right|\Psi_\rho \tag{2.6}$$

The ground-state energy functional $E\left[\rho,V_{ext}\right]$ satisfies the variational principle:

$$E_{GS}=E\left[\rho,V_{ext}\right]=\int drV_{ext}(r)\rho[r]+F_{HK}[\rho] \tag{2.7}$$

where $\rho\left(r\right)$ is the minimum value.

Based on the Kohn-Sham approach[120], a simplified approximation for the energy functional $E\left[\rho,V_{ext}\right]$ is described as

$$F_{HK}[\rho]=T_s+\frac{1}{2}\int dr\Phi(r)\rho[r]+E_{xc}[\rho] \tag{2.8}$$

where $T_s$ is the kinetic energy of non-interacting electrons, $\Phi$ is the Coulomb potential of electrons, and $E_{xc}$ is the exchange-correlation energy[120]. The use of variational principle for Eq. (2.9) results in

$$\frac{\delta E[\rho, V_{ext}]}{\delta\rho(r)} = \frac{\delta T_s}{\delta\rho(r)} + V_{ext}(r) + \Phi(r) + \frac{\delta E_{xc}(\rho)}{\delta\rho(r)} = \mu \tag{2.9}$$

where $\mu$ is the Lagrange multiplier with the constraint of constant electron number. Considering the same electron density $\rho$ in the system, a new effective potential $V_{eff}(r)$ can be generally described as[121]:

$$\frac{\delta E[\rho]}{\delta\rho(r)} = \frac{\delta T_s}{\delta\rho(r)} + V_{eff}(r) = \mu \tag{2.10}$$

where $V_{eff}(r) = V_{ext}(r) + \Phi(r) + \frac{\delta E_{xc}(\rho)}{\delta\rho(r)}$.

In the model of non-interacting particles, the solution of Eq. (2.10) can be obtained by solving the Kohn-Sham equations:

$$\left[-\frac{1}{2}\nabla^2 + V_{eff}(r)\right]\phi_i(r) = \varepsilon_i\phi_i(r) \tag{2.11}$$

Using the density for the *N*-particle system in the following form:

$$\rho(r) = \sum_{i=1}^{N} f_i \left|\phi_i(r)\right|^2 \tag{2.12}$$

where $\phi_i$ are the Kohn-Sham (KS) orbitals and $f_i$ are occupation numbers. In principle, the energy expression of Kohn-Sham functional is exact. The main challenge is the unknown form of an exact exchange-correlation functional. Therefore, the approximations of $E_{xc}$ are unavoidable except for few very simple systems.

Kohn and Sham proposed the simple approximation for the exchange-correlation energy, *i.e.* local density approximation (LDA)[122-124]:

$$E_{xc}^{LDA} = \int dr\,\rho(r)\varepsilon_{xc}[\rho(r)] \tag{2.13}$$

where $\varepsilon_{xc}[\rho(r)]$ is the exchange-correlation energy of each particle of a homogeneous electron gas. For the spin-polarized systems, Eq. (2.13) becomes:

$$E_{xc}^{LSDA} = \int dr \rho(r) \varepsilon_{xc} \left[ \rho_{\uparrow}(r), \rho_{\downarrow}(r) \right] \tag{2.14}$$

LDA is a good approximation for those cases whose densities is almost constant[125]. However, LDA is unsuitable to describe the chemical bonding. To improve the description of the correlation energy, the effect of the density gradient must be considered, resulting in generalized gradient approximations (GGA)[126]:

$$E_{xc}^{GGA} = \int dr \rho(r) \varepsilon_{xc}[\rho(r), \nabla\rho(r)] \tag{2.15}$$

In practice, $E_{xc}^{GGA}$ can be usually divided into exchange and correlation contributions:

$$E_{xc}^{GGA} = E_{x}^{GGA} + E_{c}^{GGA} \tag{2.16}$$

Perdew, Burke and Ernzerhof developed the PBE approximation [126, 127], which is one of the most common GGA without empirical fitting. PBE and majority of other GGA functionals underestimate reaction barriers and band gaps, which can be improved by using some of hybrid functional. The general hybrid functional contains a partial contribution from Hatree-Fock exchange term:

$$E_{xc}^{hybrid} = E_{xc}^{GGA} + \lambda E_{x}^{HF} \tag{2.17}$$

For example, PBE0 can be expressed as[128]:

$$E_{xc}^{PBE0} = E_{xc}^{PBE} + 0.25\left( E_{x}^{HF} - E_{x}^{PBE} \right) \tag{2.18}$$

In addition, another hybrid functional, Heyd-Scuseria-Ernzerhof (HSE) functional[129] can be expressed as:

$$E_{xc}^{HSE} = 0.25 E_{x}^{HF,SR}(\omega) + 0.75 E_{x}^{PBE,SR}(\omega) + E_{x}^{PBE,LR}(\omega) + E_{c}^{PBE} \tag{2.19}$$

where *SR* and *LR* represent short range and long range components, and ω is a tunable parameter of the extent of short range interactions.

The HSE functional is often used to correct electronic structure deficiencies observer at PBE level, in particular when calculating electronic and optical properties of low dimensional materials.

## 2.2 DFT+U methods

GGA cannot describe systems with strong electron-electron correlations. One solution is the approximate DFT+U method[130], in which a non-local screened Coulomb potential is used to describe the non-local and energy-dependent self-energy. The DFT+U method can give the correct magnetic state for transition metals such as cerium oxides ($CeO_2$)[131], and can also provide more reasonable band gaps than GGA functionals themselves, in a better agreement with experimental values.

Dudarev *et al.*[132] proposed the rotationally invariant DFT+U approach, which is used in this thesis. The value of the effective Coulomb interaction $U_{eff} = U - J$ substitutes individual $U$ and $J$ values. The DFT+U energy is described as:

$$E_{DFT+U} = E_{DFT} + E_U \tag{2.20}$$

where $E_U$ is the effective on-site Coulomb interaction, in following form:

$$E_U = \frac{U_{eff}}{2}\sum_{\sigma}\left[\sum_{j}\rho_{jj}^{\sigma} - \sum_{j,l}\rho_{jl}^{\sigma}\rho_{lj}^{\sigma}\right] = \frac{U_{eff}}{2}\sum_{\sigma}\left[Tr\rho^{\sigma} - Tr\left(\rho^{\sigma}\rho^{\sigma}\right)\right] \tag{2.21}$$

where $\rho_{jl}^{\sigma}$ is the density matrix of $d$ electrons of transition metal element. Moreover, the $U_{eff}$ value for transition metals of a system is usually obtained by fitting experimental data, and the $U_{eff}$ value in this thesis is taken from the literature.

## 2.3 *ab initio* molecular dynamics

In *ab initio* molecular dynamics, the potential energy of the nucleus can be explicitly calculated at the DFT level (we have used Vienna *Ab initio* Simulation Package, VASP[133]). The *ab initio* molecular dynamics (AIMD) based on DFT is given by the Lagrangian[134, 135]:

$$L^{BO}(R,\dot{R}) = \frac{1}{2}\sum_{i} M_i R_i^2 - U_{DFT}\left[R;\Psi^{sc}\right] \tag{2.22}$$

where the nuclear coordinates are denoted as $R = \{R_i\}$ and the dot of $R$ is its time derivative; $U_{DFT}\left[R;\Psi^{sc}\right]$ is the ground state energy (including the ion-ion interaction) for the self-consistent electronic wave functions ($\Psi^{sc}$); $\Psi^{sc}$ is defined as $\Psi^{sc} = \{\psi_{nk}^{sc}\}$, where n and k are the band and reciprocal lattice vectors, respectively. The dynamical variables $R(t)$ and $\dot{R}(t)$ are given by the Euler-Lagrange equations:

$$\frac{d}{dt}\left(\frac{\partial L}{\partial \dot{R}}\right) - \frac{\partial L}{\partial \dot{R}} = 0 \tag{2.23}$$

In AIMD simulations in VASP, the costly process of finding the $\Psi^{sc}(t)$ is simplified with an initial guess, which is estimated from the previous steps:

$$\Psi^{sc}(t) = SCF\left[\sum_{m=1}^{M} c_m \Psi^{sc}(t - m\delta t); R\right] \tag{2.24}$$

## 2.4 Lattice dynamics and phonons

To calculate the lattice dynamical properties of materials, the density functional perturbation theory (DFPT) have been widely applied, using implementation in Phonopy packages[136]. The perturbation means to move a small displacement from the equilibrium position of an atom. The detailed expressions can be found in references[137, 138]. Phonon spectrum can be calculated from the dynamical matrix:

$$D_{ij}(\vec{q}) = \sum_{\vec{R}} e^{-i\vec{q}\cdot\vec{R}'} \frac{\partial^2 E}{\partial u_i\left(\vec{R}+\vec{R}'\right)\partial u_j(\vec{R})} \tag{2.25}$$

where ($u_i(\vec{R})$) is the atomic displacements for each atom in each direction (*i* and *j* correspond to *x*, *y*, and *z* coordinates) by solving the matrix equation:

$$D_{ij}(\vec{q})\vec{\varepsilon} = M\omega_{\vec{q}}^2\vec{\varepsilon} \tag{2.26}$$

which gives the frequencies ($\omega_{\vec{q}}^2$) of the phonons with the wave vector ($\vec{q}$). The knowledge of the phonon spectrum is fundamental to understanding the dynamic stability of compounds.

## 2.5 Magnetic materials and Monte Carlo simulations

Transition metal cations with various oxidation state form $TMX_n$ polyhedra with surrounding main-group elements X (typically, n = 4-6). The *d* orbital of $TMX_n$ splits to non-degenerate energy levels due to breaking of the spherical symmetry of the *d* orbital (*i.e.* the crystal field effect). In general, the local magnetic moments of TM ions in solid systems can be understood in terms of their high and low spin states. Based on the Griffth's theory[139], the spin states of TM ions in the crystal is determined by the relative magnitude of field splitting ($\Delta_{cf}$) and exchange splitting ($\Delta_{ex}$). In a strong crystal field ($\Delta_{cf} > \Delta_{ex}$), TM ions prefer a low spin states breaking the Hund's rule. In a weak crystal field ($\Delta_{cf} < \Delta_{ex}$), the TM ions prefer a high spin states to following the Hund's rule. However, calculations at GGA and LDA level generally underestimate the exchange splitting of TM ions, resulting in an incorrect spin state. In general, DFT+U and HSE can appropriately correct the exchange splitting and give a correct spin state for magnetic materials[140].

The macroscopic magnetism of materials is derived from the spin arrangement (*i.e.*, spin-exchange interaction)[141]. Different spin arrangements of TM ions generate the FM, AFM and ferrimagnetic (FIM) order in magnetic materials. The strength of the spin-exchange in materials is related to spin exchange parameter described by model spin Hamiltonian:

$$H_{spin} = \sum_{i \neq j} J_{ij} \hat{S}_i \cdot \hat{S}_j \tag{2.27}$$

based on DFT calculations of different spin-configurations, the exchange-coupling parameter ($J_{ij}$) can be evaluated by energy-mapping analysis. The $T_C$ and Néel temperature ($T_N$) of the FM (and AFM) materials is a reflection of the $J_{ij}$ strength. $T_C$ (and $T_N$) is defined as a critical temperature. The magnetism transition is from FM (and AFM) to paramagnetic (or vice versa) occurs at the critical temperature. $T_C$ and $T_N$ can be evaluated by the mean-field theory[142] or Monte Carlo simulations[143].

## 2.6 Berry curvatures

In the system lacking inversion symmetry (for example monolayer TMDs or the biased graphene bilayer), carriers (electron and hole) in $K^+$ and $K^-$ valleys are subjected to opposite Berry curvatures ( $\vec{\Omega} = \vec{\nabla}_k \times \vec{A}(k)$ ), which is a tensor derived from the Berry phase[144]:

$$\vec{A}(k) = i \sum_{occupied} \left\langle u_{nk} \mid \vec{\nabla}_k \mid u_{nk} \right\rangle \tag{2.28}$$

where *k* is the crystal momentum, *n* is the band index, and $u_{nk}$ as the periodic part is from Bloch wave function $\Psi_{nk}(r) = e^{ik \cdot r} u_{nk}(r)$ . The detailed expressions can be found in references[145].

Berry curvatures act like effective magnetic fields in the momentum space[101, 106]. The magnetic moment of valleys also arises from the orbital angular momentum, which is related to the effect of the Berry phase of electrons that arise from the band structure[144, 146]. Moreover, in a system that have strong SOC, the time-reversal symmetry dictates the spin splitting to have opposite signs at $K^+$ and $K^-$ valleys, giving rise to an effective coupling between spin and valley. Strong spin-valley coupling can enhance the spin and valley polarization lifetime.

The Berry curvature has a strong effect on the electronic transport properties and is the kernel parameter to various Hall effects[147]. Hence, we considered the spin-resolved non-zero *z*-component Berry curvature ( $\Omega_{n,z}^{\uparrow(\downarrow)}$ ) from the Kubo's formula derivation[148],

$$\Omega_{n,z}^{\uparrow(\downarrow)}(k) = -\sum_{n' \neq n} \frac{2\,\mathrm{Im}\left\langle \varphi_{n,k}^{\uparrow(\downarrow)} \mid \nu_x \mid \varphi_{n',k}^{\uparrow(\downarrow)} \right\rangle \left\langle \varphi_{n',k}^{\uparrow(\downarrow)} \mid \nu_y \mid \varphi_{n,k}^{\uparrow(\downarrow)} \right\rangle}{(E_{n'}^{\uparrow(\downarrow)} - E_n^{\uparrow(\downarrow)})^2} \tag{2.29}$$

where $\nu$ is velocity operator, $E_n$ is the energy of the *n*th band, and $\left\langle \varphi_{n,k}^{\uparrow(\downarrow)} \mid \nu_x \mid \varphi_{n',k}^{\uparrow(\downarrow)} \right\rangle$ is the matrix element of the velocity operator.

The Berry curvature was calculated using the *ab initio* tight binding method and using maximally localized Wannier functions implemented in Wannier90 code[149].

## 2.7 Models and computational details

The aim of this thesis was to investigate novel properties of low-dimensional materials for their potential applications. For such purpose, the systematic computational investigation can help to increase the atomistic understanding of those low-dimensional materials. The models in these studies are shown in Figure 2.1, showing typical structures of these materials. In particular, several carbide MXenes, including traditional MXenes, double metal MXenes (out-of-plane), *i*-MXenes (in-plane), are depicted. For MXenes, the functional groups are positioned above the hollow site formed by three neighboring C atoms mirroring the positions of the metals on the opposite surface. In general, such structures are systematically more stable than structures with functional groups sitting on top of the C atoms. In addition, the models of Janus TMDs and isolated $VS_4$ NWs are also shown in Figure 2.1.

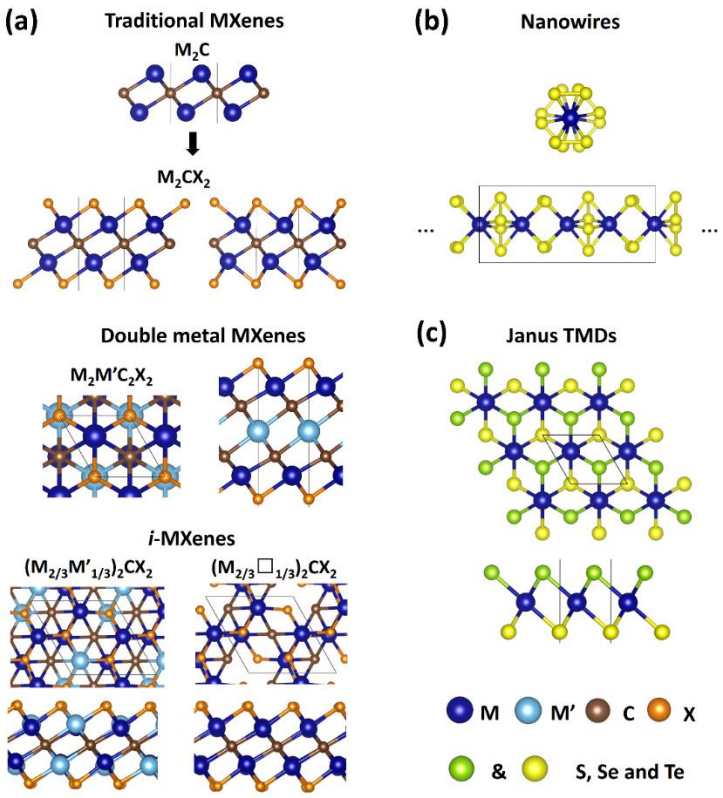


**Figure 2.1** Top and side views of typical structures of (a) various examples of MXenes, (b) $VS_4$ nanowires, and (c) Janus TMDs. The unit cell of these material is marked by black lines. M and M' indicate transition metal atoms, "X" indicates the functionalization, and "□" indicates the vacancy.

Calculations with periodic models were performed at the DFT level with the projected augmented wave approximation, as implemented in VASP[133]. PBE+U and HSE06 exchange–correlation functional were used in this work. The geometry optimizations were carried out at the PBE level which is considered sufficient for most solids. The choices of k-point sampling depended on the system. In this thesis, 1D and 2D models of nanowire and monolayer, respectively, are associated with a large vacuum (approximately 15 Å) to avoid the artificial interactions between periodic images. The phonon spectra of investigated materials were performed with Phonopy packages[136]. The Monte-Carlo simulations of $T_C$ and $T_N$ were performed with open access softwares, ALPS[150] and MCsolver[151]. Electronic and magnetic properties of materials were post-processed by applying VASPKIT[152]. The Berry curvature was post-processed applying WannierTools.[153]

# CHAPTER 3. Results

## 3.1 $Cr_2TiC_2FCl$ MXene: Bipolar AFM semiconductor

The double metal MXenes extends the family of the ordered 2D transition metal carbides, where two different early transition metals (M and M') combine to $M_2M'C_2$ and $M_2M'_2C_3$ [22]. In these MXenes, M layers sandwich M' carbide layers, for example, $Cr_2TiC_2X_2$ (X is the functionalization, **Figure 3.1**). Since the M' atoms are on the outside, they can be functionalized and magnetic and electronic properties of corresponding MXenes can thus be controlled.

Most of the theoretical and experimental studies focused on FM order. The extra or intra magnetic fields limit the generation and complicate the manipulation of spin-polarized carriers in FM materials. In principle, AFM materials show intrinsic advantages, including robustness against magnetic field perturbation, no stray fields, and high speed of device operation (see Section 3.1 and 3.4). Therefore, AFM materials have attracted great attention for potential applications in spintronics. The manipulation and detection of spin structures in AFM materials have been the challenge due to the absence of a net magnetic moment and spin degeneracy in the band structure. In order to solve those problems, the concept of HMAF in CrMnSb Heusler compounds was proposed[79]. Such HMAF materials offer new opportunities to manipulate and detect the spin in AFM materials. However, only a few 2D AFM systems have been predicted to have the high spin-polarization.

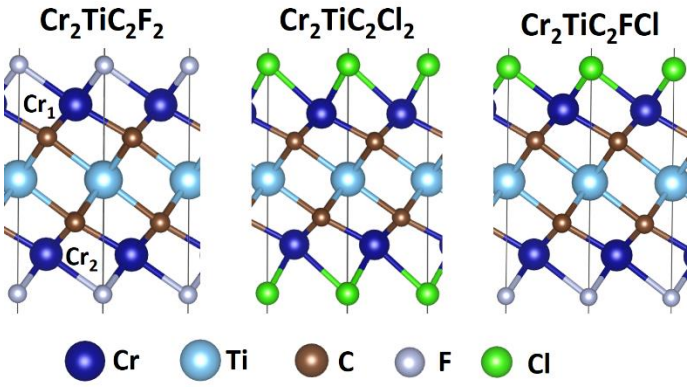


**Figure 3.1** The side view of $Cr_2TiC_2F_2$, $Cr_2TiC_2Cl_2$ and $Cr_2TiC_2FCl$ MXenes. The color scheme for different atoms is described in the figure. The $Cr_1$ and $Cr_2$ represent the Cr bonded with Cl and F, respectively.

We propose that the $Cr_2TiC_2FCl$ MXene (**Figure 3.1**) is a bipolar antiferromagnetic semiconductor (BAFS) with vanishing magnetic moment. The gate voltage can be used to manipulate the spin direction, leading to the transition from BAFS to HMAF. The underlying mechanisms can be explained based on the band structure analysis (Section 3.1.3).

### 3.1.1 Symmetrical functionalization of $Cr_2TiC_2$ MXenes

We firstly discuss geometrical, electronic and magnetic properties of symmetrically functionalized MXenes. The $Cr_2TiC_2F_2$ and $Cr_2TiC_2Cl_2$ MXenes are AFM semiconductors with band gap of 1.26 eV and 1.04 eV, respectively. Their band structures are shown in **Figure 3.2**.

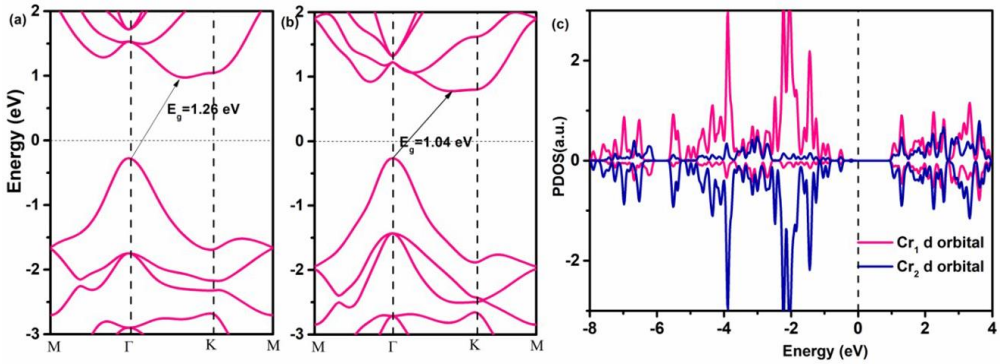


**Figure 3.2** The band structure of (a) $Cr_2TiC_2F_2$ and (b) $Cr_2TiC_2Cl_2$ MXenes. (c) The PDOS of 3*d* states are shown for the Cl-bonded ($Cr_1$) and F-bonded ($Cr_2$) Cr atoms in $Cr_2TiC_2F_2$, respectively. The Fermi level is set to zero.

Each Cr atom is spin-polarized and it has local magnetic moment, however there is no net spin-polarization in the $Cr_2TiC_2F_2$ MXene due to the compensated AFM order. The projected density of states (PDOS) of Cr-3*d* orbitals in the upper and lower layers show that symmetrically functionalized $Cr_2TiC_2$ have the symmetrical distribution due to equivalent chemical environments of Cr atoms. The Janus graphene (asymmetrically functionalized by fluorine and hydrogen) had been experimentally synthesized. Therefore, we are interested in the impact of electronic and magnetic properties of asymmetrically functionalized $Cr_2TiC_2$ MXenes.

### 3.1.2 Electronic and magnetic properties of $Cr_2TiC_2FCl$

We now explore the electronic and magnetic properties of $Cr_2TiC_2FCl$ MXene. To determine the magnetic ground state of $Cr_2TiC_2FCl$ MXene, the collinear FM, AFM-a, AFM-b and AFM-c states were considered (**Figure 3.3**). The AFM-c magnetic configuration (set as the reference energy) has the lowest energy. FM, AFM-a, and AFM-b configurations have energies of 210 meV, 717 meV, 618 meV, respectively. Therefore, the AFM-c state of $Cr_2TiC_2FCl$ MXene is the magnetic ground state with high magnetic stability. The Cr sublattices are separated by $Ti_2C$ layers with a vertical distance of 4.76 Å. Therefore, the AFM-c ground state configuration includes both intra-plane and inter-plane magnetic coupling.

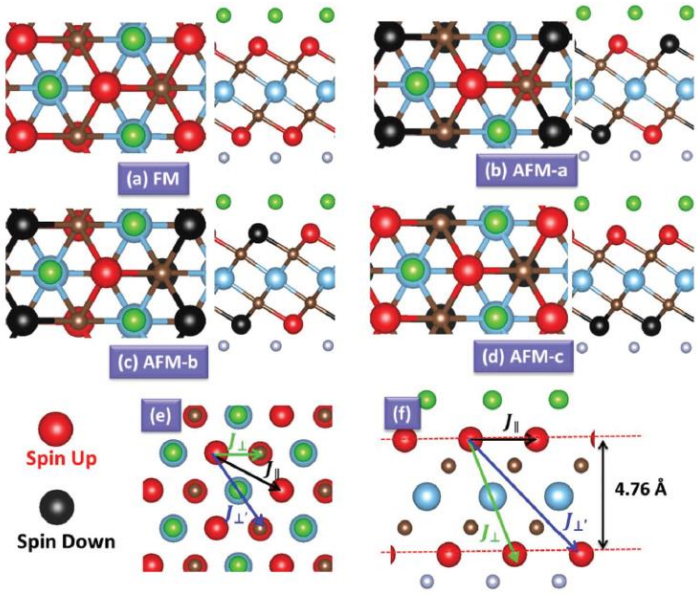


**Figure 3.3** The top and side views of possible magnetic configurations of the $Cr_2TiC_2FCl$ MXene: FM (a), AFM-a (b), AFM-b (c), and AFM-c (d). Red and black balls represent Cr atoms with spin up and spin down electron configurations. The spin exchange parameter $J_{\parallel}$, $J_{\perp}$ and $J_{\perp'}$ are shown in parts (e) and (f) in the top and side view, respectively.

The magnetic exchange coupling parameters ($J_{\parallel}$, $J_{\perp}$ and $J_{\perp'}$) of $Cr_2TiC_2FCl$ MXene are 62.52 meV, −12.28 meV and −18.80 meV, respectively. These results demonstrate that the intra-plane coupling between two Cr sublattices has a strong FM coupling, while inter-plane interactions have AFM coupling. Given by the mean-field approximation, we calculated the $T_N$

of $Cr_2TiC_2FCl$ MXene. The high $T_N$ of $Cr_2TiC_2FCl$ MXene is 901 K, which suggests potential applications of AFM spintronic devices at room-temperature.

### 3.1.3 Induced HMAF in $Cr_2TiC_2FCl$ MXene

The band structure of $Cr_2TiC_2FCl$ shows the semiconducting features with an indirect band gap of 0.91 eV (**Figure 3.4**). VBM and CBM of $Cr_2TiC_2FCl$ MXene are derived from two opposite spin channels. Therefore, the $Cr_2TiC_2FCl$ MXene is BAFS. The BAFS feature of $Cr_2TiC_2FCl$ also can be described by three energy gaps (Δ1, Δ2 and Δ3) (**Figure 3.4d**).

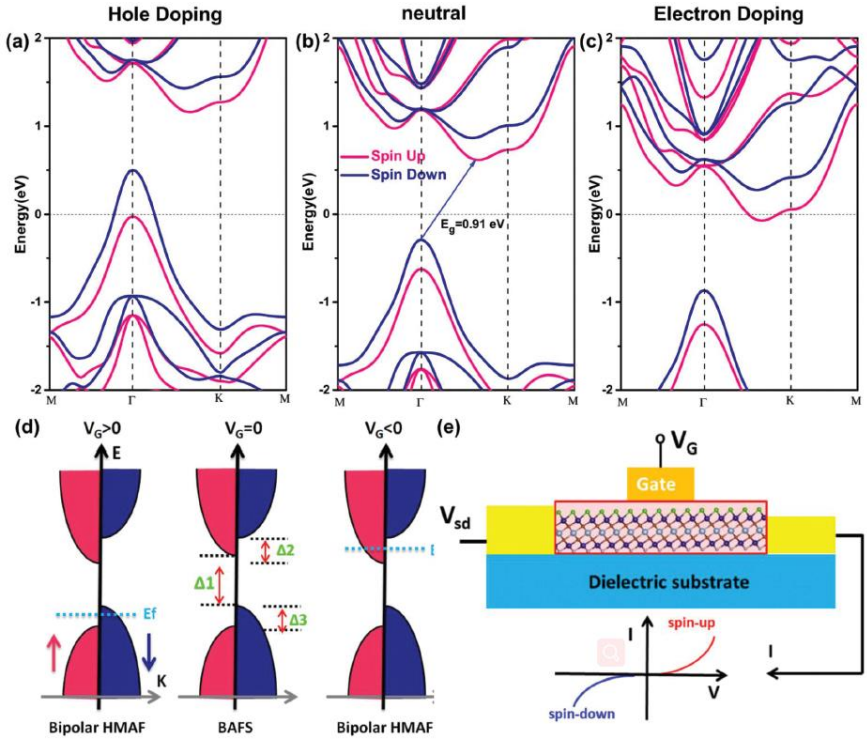


**Figure 3.4** Band structures of $Cr_2TiC_2FCl$ double MXenes with carrier doping (a) 0.1 hole (b) neutral, and (c) 0.1 electron per unit cell. (d) Schematic of transformation between the bipolar HMAF and BAFS states under gate voltages. Spin–flip gaps and spin-conserved gaps (Δ1, Δ2 and Δ3) are marked. (e) Schematic of AFM spintronics device based on BAFS materials, together with the I–VG relationship under positive and negative gate voltage.

The Δ1 gap is defined as a spin-flip gap with opposite spin polarization between the VBM and CBM, while (Δ1 + Δ2) and (Δ1 + Δ3) are defined as spin-conserved gaps. Δ1 should be small enough to shift the Fermi level to the spin-up (or spin-down) channel by the gate voltage.

Moreover, Δ2 and Δ3 should be large to guarantee the half-metallic gap. The values of Δ1, Δ2 and Δ3 are 0.91 eV, 0.31 eV, and 0.27 eV, respectively. These values indicate that $Cr_2TiC_2FCl$ MXene has potential applications in AFM spintronics. We show that carrier doping for $Cr_2TiC_2FCl$ MXene can shift the Fermi level to different spin-polarized VBM and CBM regions, resulting in a tunable spin orientation. The completely spin-polarized current with HMAF properties can be realized in $Cr_2TiC_2FCl$ MXene by a specific dopant (**Figure 3.4**).

### 3.1.4 The origin of BAFS

To gain insight into electronic properties of $Cr_2TiC_2FCl$ MXene, PDOS of the $Cr_1$ and $Cr_2$ atoms were plotted (**Figure 3.5**). According to the $D_{3d}$ local symmetry of the crystal field of Cr atoms, Cr-3*d* orbitals split into a non-degenerate a ($d_{z^2}$) orbital and two 2-fold degenerate $e_1$ ($d_{yz} + d_{xz}$) and $e_2$ ($d_{x^2-y^2} + d_{xy}$) orbitals. VBM and CBM states of $Cr_2TiC_2FCl$ MXene are derived from the $Cr_2$-a and mixed $Cr_1$-$e_1$ (and -$e_2$) states, respectively.

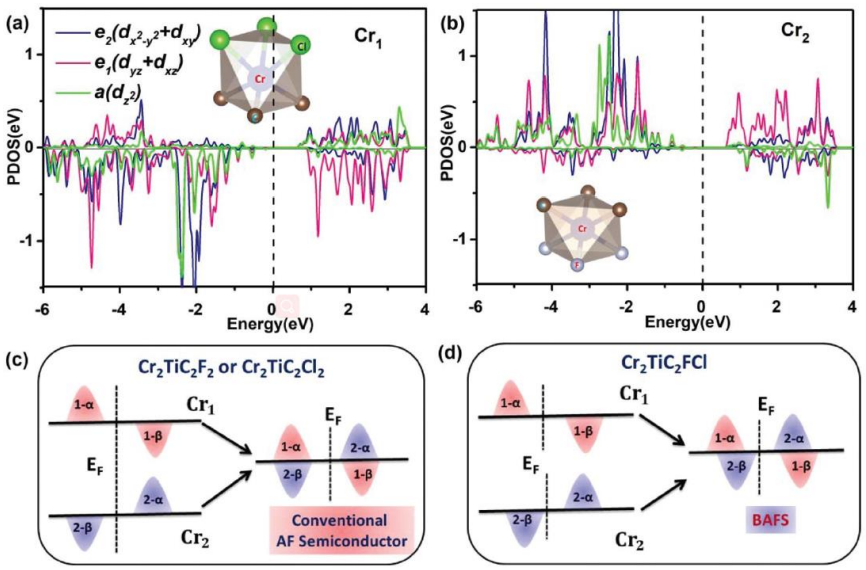


**Figure 3.5** PDOS of d states for (a) $Cr_1$ and (b) $Cr_2$ of $Cr_2TiC_2FCl$ MXene. The insets show the local structure of the Cr atoms with F and Cl functionalization, respectively. The Fermi level is set to zero. Schematic diagrams of the Cr spin exchange splitting in (c) symmetrically and (d) asymmetrically functionalized MXenes. α and β represent the spin-up and spin down, respectively.

According to Griffith's crystal field theory, the distribution of the 3*d* states of Cr reflects the crystal field splitting ($\Delta_{cf}$) and exchange splitting ($\Delta_{ex}$) due to the crystal field interactions and on-site coulombic interaction, respectively. $\Delta_{cf}$ and $\Delta_{ex}$ of $Cr_1$-3*d* and $Cr_2$-3*d* are different due to Cr ions located in different chemical environments. Schematics of the $Cr_1$ (upper Cr) and $Cr_2$ (lower Cr) spin exchange splitting in symmetrically and asymmetrically functionalized surfaces are shown in **Figure 3.5**. For the $Cr_2TiC_2FCl$ MXene, different chemical environments in the upper and the lower surface induces a mismatch of Cr-3*d* states and consequently results in the BAFS feature.

### 3.1.5 The mixed functionalization

The Janus $Cr_2TiC_2FCl$ MXene with the perfectly asymmetrical functionalization is an ideal model. In general, MXenes are obtained by exfoliation in the HF solution where both surfaces have mixed functionalizations. Therefore, the electronic properties for $Cr_2TiC_2$ MXene with mixed functionalization should be considered. Several mixed functionalization models ($Cr_2TiC_2F_xCl_{2-x}$, x = 0.25, 0.75, 1.25, 1.75) and their magnetic and electronic properties are shown in **Figure 3.6**.

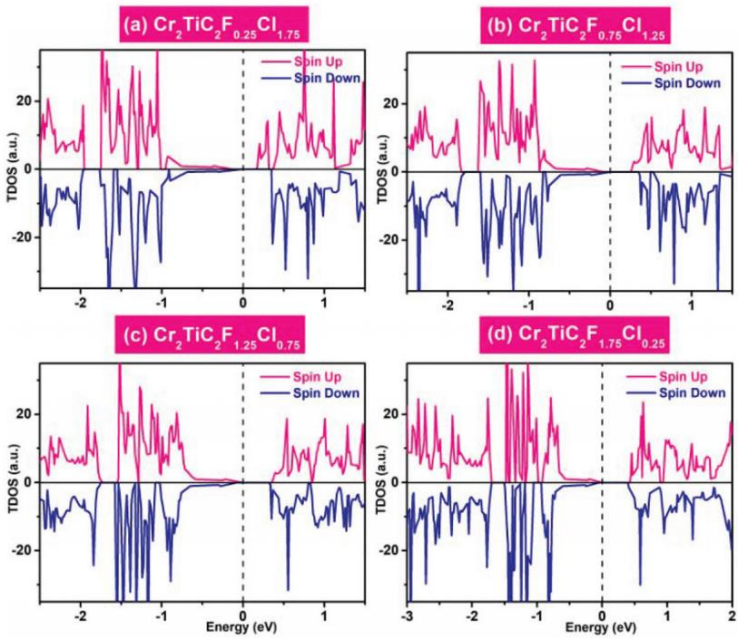


**Figure 3.6** DOS for $Cr_2TiC_2F_xCl_{2-x}$ systems, x = 0.25 (a), 0.75 (b), 1.25 (c), 1.75 (d). The pink and blue colors represent the spin up and spin down polarizations, respectively. The Fermi level is set to zero.

The results show that $Cr_2TiC_2$ MXene with mixed functionalization remain as a BAFS with interlayer AFM ground states. Therefore, even mixed functionalizations on $Cr_2TiC_2$ MXene is sufficient to affect the chemical environment of Cr atoms to observe BAFS feature. Moreover, the varying concentration of F and Cl on the surfaces of $Cr_2TiC_2$ MXene can provide an effective way to control the spin polarization.

### 3.1.6 Summary

A new 2D BAFS, $Cr_2TiC_2FCl$ MXene, is reported. The $Cr_2TiC_2FCl$ MXene with AFM order and bipolar semiconducting character has potential applications for generating and manipulating spin-polarized carriers in AFM spintronics. In analogy to conventional semiconductor field effect transistors (FET), the gate voltage can tune the half-metallicity and can control its spin polarized orientation. We briefly demonstrate a typical AFM spin-FET. Applying a real gate voltage may enhance or suppress the dipole moment and change the shape of the electronic band. Our results open up a new route for AFM spintronics and the realization of AFM spin-FET.

## 3.2 *i*-MXenes: in-plane ordering MXenes

*i*-MXene ("*i*" indicates in-plane ordering) as a new type of MXene is derived from the *i*-MAX phases, which can be described as $(M_{2/3}M'_{1/3})_2AlC$. *i*-MAX phases reported to date have the *C2/c* monoclinic or the *Cmcm* orthorhombic structure. $(Mo_{2/3}Sc_{1/3})_2AlC$ and $(V_{2/3}Zr_{1/3})_2AlC$ were the first examples of *i*-MAX phase[24]. In *i*-MAX, the M' atoms are arranged in a hexagonal arrangement, M' atoms are at the centers of hexagons, and Al atoms are arranged in a Kagome-like lattice.

Moreover, the vacancy-ordered *i*-MXene $(Mo_{2/3}\square_{1/3})_2C$ (where $\square$ denotes the missing transition metal atom) has been reported[26]. While the pristine *i*-MXene $(Mo_{2/3}\square_{1/3})_2C$ is non-magnetic, different surface functional groups can be used to tune the band gap. In this section, we describe our investigation of the $(V_{2/3}Zr_{1/3})_2AlC$ *i*-MAX phase and the properties of the corresponding $(V_{2/3}Zr_{1/3})_2C$ *i*-MXene and related vacancy ordered $(V_{2/3}\square_{1/3})_2C$ *i*-MXene. It is demonstrated based on the first principle calculations that suitable surface functionalization affects the electronic and magnetic properties of both $(V_{2/3}Zr_{1/3})_2CX_2$ and $(V_{2/3}\square_{1/3})_2CX_2$ (X = O, F and OH) *i*-MXenes.

### 3.2.1 Structure and stability

Most MXenes have the high-symmetry *P31m* space group. In our case, the symmetry of bimetallic and vacancy-ordered *i*-MXenes is lower than that of the $V_2C$ MXene due to the presence of Zr atoms (or vacancy). *i*-MXene structures derive from corresponding bulk *i*-MAX phases (**Figure 3.7**). The pristine $(V_{2/3}Zr_{1/3})_2C$ *i*-MXene is formed (removal of the Al layer) by three hexagonal layers stacked on top of each other, and the layer of C atoms is sandwiched between layers composed of V and Zr atoms (**Figure 3.7b**). The Zr atoms are all aligned along the short diagonal of the xy plane. Functionalized *i*-MXenes are obtained by surface functionalization (F, OH, or O), and vacancy-ordered *i*-MXenes are obtained by removing Zr atoms. The structural details (lattice constant, bond lengths, etc.) are outlined in **Table 3.1**.

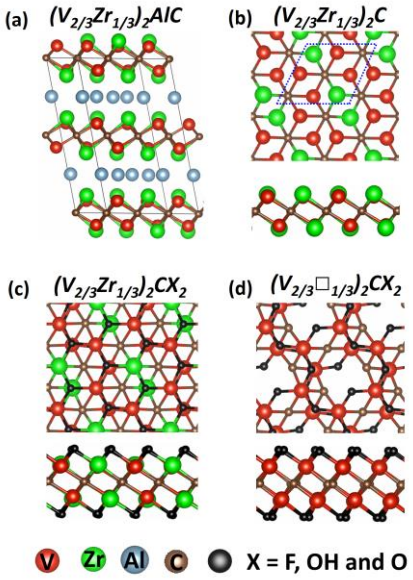


**Figure 3.7** Structures of parent *i*-MAX phase $(V_{2/3}Zr_{1/3})_2AlC$ (a), pristine bimetallic *i*-MXene $(V_{2/3}Zr_{1/3})_2C$ (b), functionalized bimetallic *i*-MXene $(V_{2/3}Zr_{1/3})_2CX_2$ (c) and vacancy-ordered $(V_{2/3}\square_{1/3})_2CX_2$ (X = F, OH and O) *i*-MXene (d). The unit cell of *i*-MXenes is marked by a blue dotted line.

To accurately assess the phonon dispersion and the band structure (see 3.2.2 section) of *i*-MXenes, we expanded the definition of symmetry points of the hexagonal Brillouin zone (**Figure 3.8**), thus breaking the degeneracy of M and K points and naming the now inequivalent points as M1, K1, M2, K2, M3, K3, as previously reported for $(Mo_{2/3}\square_{1/3})_2CX_2$[26]. The energy difference at symmetry points is significant and therefore cannot be disregarded.

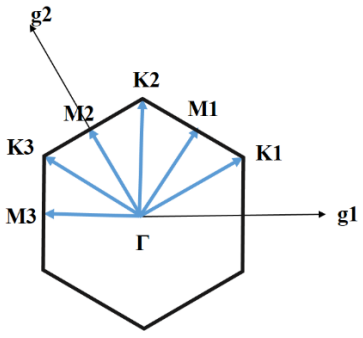


**Figure 3.8** A schematic representation of the Brillouin zone of a 2D hexagonal lattice, along with an expansion of symmetry points for the reduced symmetry of $(V_{2/3}Zr_{1/3})_2CX_2$ and $(V_{2/3}\square_{1/3})_2CX_2$ *i*-MXenes. g1 and g2 are the basis vectors.

**Table 3.1** Calculated structural characteristics of $V_2C$ MXene, pristine $(V_{2/3}Zr_{1/3})_2C$ *i*-MXene, three different $(V_{2/3}Zr_{1/3})_2CX_2$ *i*-MXenes and two vacancy ordered $(V_{2/3}\square_{1/3})_2CX_2$ *i*-MXene. L is the lattice constant (Å). $d_1$ and $d_2$ are bond distances between V and C atoms, $d_3$ is the bond distance between Zr and C atoms. Q is the atomic charge obtained by Bader charge analysis.

| Configurations | L | $d_1$ | $d_2$ | $d_3$ | Q(V) | Q(Zr) | Q(C) | Q(O) | Q(F) |
|---|---|---|---|---|---|---|---|---|---|
| $V_2C$ | 5.435 | 2.111 | 2.111 | / | -1.33 | / | 2.65 | / | / |
| $(V_{2/3}Zr_{1/3})_2C$ | 5.368 | 2.127 | 2.099 | 2.223 | -1.17 | -1.33 | 2.40 | / | / |
| $(V_{2/3}Zr_{1/3})_2CO_2$ | 5.262 | 2.087 | 2.084 | 2.429 | -2.12 | -2.32 | 1.96 | 1.21 | / |
| $(V_{2/3}Zr_{1/3})_2CF_2$ | 5.485 | 2.109 | 2.226 | 2.256 | -1.81 | -2.14 | 2.18 | / | 0.81 |
| $(V_{2/3}Zr_{1/3})_2C(OH)_2$ | 5.508 | 2.225 | 2.225 | 2.171 | -1.81 | -2.09 | 2.24 | 1.80 | / |
| $(V_{2/3}\square_{1/3})_2CF_2$ | 5.136 | 2.032 | 2.107 | / | -2.21 | / | 1.59 | / | 0.70 |
| $(V_{2/3}\square_{1/3})_2C(OH)_2$ | 5.157 | 1.938 | 2.042 | / | -2.19 | / | 1.64 | 1.63 | / |

The stability and other properties of *i*-MXenes depend on functionalization, which in turn depends on the exfoliation process. We selected the following surface functional groups: O, F and OH. The functional groups are positioned above the hollow site formed by three neighboring C mirroring thus the positions of the metals on the opposite layer. Such structures are more stable than those with functionalization groups above the C atoms.

To evaluate the stability of functionalized $(V_{2/3}Zr_{1/3})_2CX_2$ *i*-MXenes, the formation energy ($E_{form}$) is calculated as:

$$E_{form} = \frac{(E[(V_{2/3}Zr_{1/3})_2CX_2] - E[(V_{2/3}Zr_{1/3})_2C] - 2E[X_g])}{2}$$

where $E[(V_{2/3}Zr_{1/3})_2C]$ and $E[(V_{2/3}Zr_{1/3})_2CX_2]$ stand for the total energies of pristine $(V_{2/3}Zr_{1/3})_2C$ and functionalized $(V_{2/3}Zr_{1/3})_2CX_2$ *i*-MXenes, respectively. $E[X_g]$ is the gas phase energy of 1/2 $O_2$ and 1/2 $F_2$ molecules and E[OH] is the difference E[$H_2O$] – 1/2 E[$H_2$]. The formation energies of $(V_{2/3}Zr_{1/3})_2CX_2$ *i*-MXenes are large, -5.21, -7.55 and -4.48 eV for X = F, OH and O, respectively, thus the formation of strong chemical bonds on *i*-MXenes surfaces (V or Zr atoms) is expected.

The stability of *i*-MXenes is also demonstrated by AIMD simulations carried out at 300K (**Figure 3.9** shows the results for $(V_{2/3}Zr_{1/3})_2C$ *i*-MXene). However, the $(V_{2/3}\square_{1/3})_2C$ and $(V_{2/3}$

$\square_{1/3})_2CO_2$ structures are subjected to large interatomic forces and heavily distortion during a short AIMD simulation. We also found that only $(V_{2/3}\square_{1/3})_2CF_2$ and $(V_{2/3}\square_{1/3})_2C(OH)_2$ are kinetically stable, based on both AIMD and phonon spectra calculations.

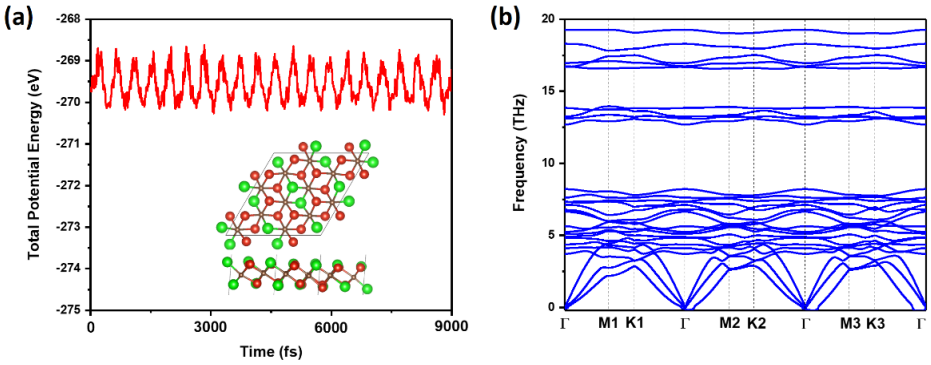


**Figure 3.9** (a) Variations of the total potential energy of $(V_{2/3}Zr_{1/3})_2C$ *i*-MXene during AIMD simulations at 300 K. (b) Phonon dispersion curves for $(V_{2/3}Zr_{1/3})_2C$ *i*-MXene.

### 3.2.2 Magnetic and electronic properties

We used the collinear magnetic model and considered the FM configuration and three possible AFM states to calculate the preferred magnetic ground state structures of *i*-MXenes (**Figure 3.10**).

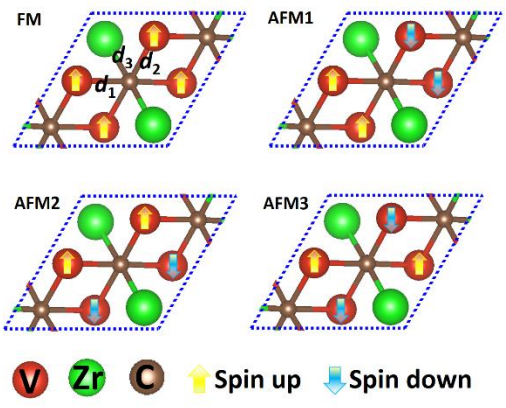


**Figure 3.10** FM and three AFM states of $(V_{2/3}Zr_{1/3})_2C$ *i*-MXenes are presented. $d_1$, $d_2$ and $d_3$ are bond length of C-V and C-Zr.

The $(V_{2/3}Zr_{1/3})_2C$ *i*-MXene exhibits an antiferromagnetic behavior with the super-exchange mechanism. This can be seen in the spin polarized charge densities and in electron localization functions (ELF is a probability of finding an electron in the neighborhood space of a reference electron) (**Figure 3.11**). PDOS of $(V_{2/3}Zr_{1/3})_2C$ shows a semiconducting character with a band gap of 0.78 eV (**Figure 3.11**). PDOS near CBM and VBM have main contributions from the V-3*d* orbitals, while the contributions from Zr-3*d* orbitals and C-2*p* orbitals are insignificant.

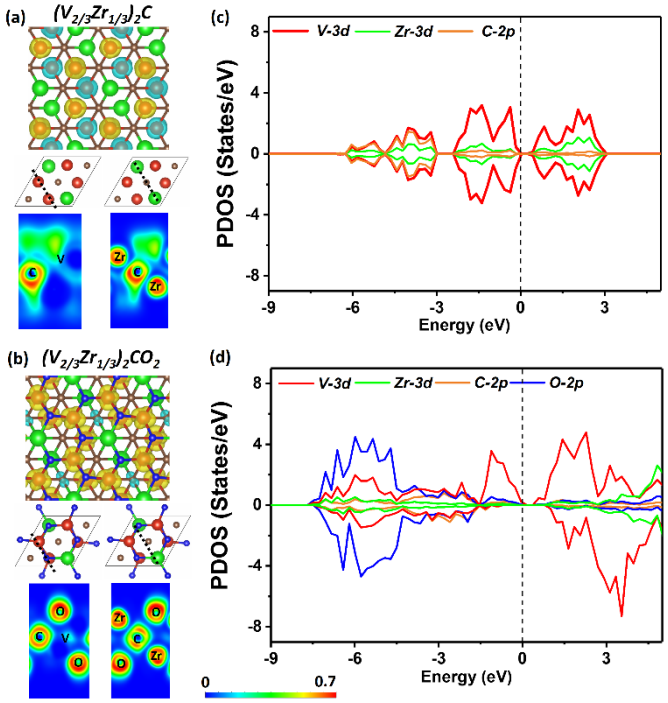


**Figure 3.11** Spin polarized charge densities and ELF maps (perpendicular to [001]) are shown for (a) $(V_{2/3}Zr_{1/3})_2C$ and (b) $(V_{2/3}Zr_{1/3})_2CO_2$, where spin up and spin down densities are shown in yellow and light blue, respectively. The units of color scale is "probability". PDOS of (c) $(V_{2/3}Zr_{1/3})_2C$ and (d) $(V_{2/3}Zr_{1/3})_2CO_2$. Fermi level (black dotted line) is set to zero.

Magnetic properties of $(V_{2/3}Zr_{1/3})_2CO_2$ *i*-MXene are qualitatively different. The presence of surface oxygens changes the magnetic ordering, resulting in FM ground state with $\Delta E = E_{AFM} - E_{FM}$ of 33.59 meV/unitcell with respect to the most stable AFM state. The total magnetic moment of $(V_{2/3}Zr_{1/3})_2CO_2$ *i*-MXene is 4 $\mu_B$ per unit cell. V-3*d* electrons can induce the spin-polarization of the neighboring C atoms via double-exchange mechanism (**Figure 3.11**). The

$(V_{2/3}Zr_{1/3})_2CO_2$ *i*-MXene exhibits distinct half-semiconductor features. The two half-semiconducting gaps are 0.53 and 1.85 eV for spin-up and spin-down channels (**Figure 3.11**), respectively. In addition, both $(V_{2/3}Zr_{1/3})_2CF_2$ and $(V_{2/3}Zr_{1/3})_2C(OH)_2$ *i*-MXenes exhibits an AFM magnetic character.

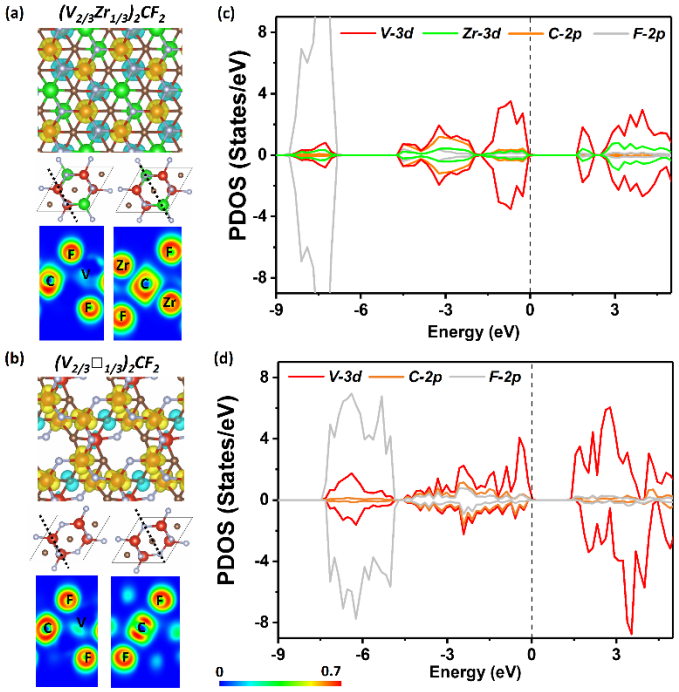


**Figure 3.12** Spin polarized charge densities and ELF maps (perpendicular to [001]) are shown for (a) $(V_{2/3}Zr_{1/3})_2CF_2$ and (b) $(V_{2/3}\square_{1/3})_2CF_2$, where spin up and spin down densities are shown in yellow and light blue, respectively. The units of color scale is "probability". PDOS of (c) $(V_{2/3}Zr_{1/3})_2CF_2$ and (d) $(V_{2/3}\square_{1/3})_2CF_2$. Fermi level (black dotted line) is set to zero.

The pristine $(V_{2/3}\square_{1/3})_2C$ *i*-MXene is unstable and therefore cannot be directly compared to the pristine bimetallic *i*-MXene. Contrary to $(V_{2/3}Zr_{1/3})_2CF_2$ *i*-MXene, the FM ordering is the most stable in $(V_{2/3}\square_{1/3})_2CF_2$ *i*-MXene, with $\Delta E$ of 22.93 meV. The reduced presence of metals induces an overall magnetic moment of 2 $\mu_B$, with the unpaired spins localized on V atoms (**Figure 3.12**). The FM ordering of $(V_{2/3}\square_{1/3})_2CF_2$ *i*-MXene results from the effect of V-3*d* electrons, which induce spin-polarization of neighboring C atoms via a double exchange mechanism (**Figure 3.12**). We can also observe a smaller polarization on VBM, due to the slight shift in the PDOS of the V-3*d* orbitals in the spin-down channel. The polarization of the

band edges can be explained by PDOS of V-3*d* orbital, C-2*p* and F-2*p* orbitals also significantly contribute to the VBM. We also considered the $(V_{2/3}\square_{1/3})_2C(OH)_2$, which behaves similarly to $(V_{2/3}\square_{1/3})_2CF_2$. However, due to the lower electronegativity of OH, the effect of spin polarization is weaker and hence $\Delta E$ is smaller.

### 3.2.3 Curie Temperatures

DFT results do not take into account magnetic properties with respect to temperature and model size effect. To account for these effects we used a simple Ising model. We considered the collinear magnetic model. The nearest-neighbor ($J_1$), second-nearest-neighbor ($J_2$), and third-nearest-neighbor ($J_3$) coupling constants were taken from DFT calculations (**Figure 3.13**).

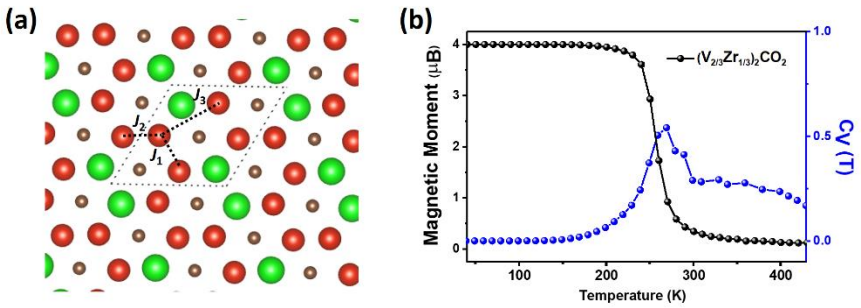


**Figure 3.13** (a) The nearest-neighbor ($J_1$), second-nearest-neighbor ($J_2$), and third-nearest-neighbor ($J_3$) coupling constants. (b) Variation of the total magnetic momentum (per unit cell) of $(V_{2/3}Zr_{1/3})_2CO_2$ MXene with respect to the temperature. Corresponding specific heats $C_V$ are shown in blue.

Curie temperatures were calculated for *i*-MXene with the FM ground state $(V_{2/3}Zr_{1/3})_2CO_2$, $(V_{2/3}\square_{1/3})_2CF_2$ and $(V_{2/3}\square_{1/3})_2C(OH)_2$. The phase transition between the FM and paramagnetic states for $(V_{2/3}Zr_{1/3})_2CO_2$ occurs around room temperature with an estimated $T_C$ of 270 K (**Figure 3.13**). This is significantly different from $(V_{2/3}\square_{1/3})_2CF_2$ and $(V_{2/3}\square_{1/3})_2C(OH)_2$ *i*-MXenes where the temperature transitions occur around 26 and 10 K, respectively. This is due to a weaker magnetic interaction upon the Zr atom removal.

### 3.2.4 Work functions

The work function (WF) of *i*-MXenes strongly depends on stoichiometry and surface

functionalization (**Figure 3.14**), which makes it possible to obtain materials which can be used as either electron emitters with low WF or contacts without Schottky barrier and high WF. The presence of electron-richer Zr in $(V_{2/3}Zr_{1/3})_2C$ *i*-MXene shifts the Fermi level and lowers the WF from 4.30 eV (pristine $V_2C$) to 3.90 eV. Surface functionalization affects the electrostatic potential charge near the surfaces, thereby increasing the WF of $(V_{2/3}Zr_{1/3})_2C$ *i*-MXene to 5.83 and 5.32 eV when the surface is functionalized by O and F, respectively. A different effect is observed in the OH functionalization, where the WF is decreased to 1.37 eV due to the intrinsic dipole of the OH group. This value is lower than that previously reported for $Sc_2C(OH)_2$ MXene (1.60 eV)[154]. Therefore, $(V_{2/3}Zr_{1/3})_2C(OH)_2$ *i*-MXene is a candidate for low-WF emitting cathods. Removing the Zr atoms increases the WF to 7.47 and 4.16 eV for $(V_{2/3}\square_{1/3})_2CF_2$ and $(V_{2/3}\square_{1/3})_2C(OH)_2$ *i*-MXenes, respectively. Our analysis shows that the WF of various $(V_{2/3}Zr_{1/3})_2C$ *i*-MXenes can be tuned within a broad range of values. Moreover, $(V_{2/3}\square_{1/3})_2CF_2$ MXene has a higher WF than the Pt metal (which has the highest WF among metals), it could thus be used for the hole injection in Schottky-barrier-free contact applications[155].

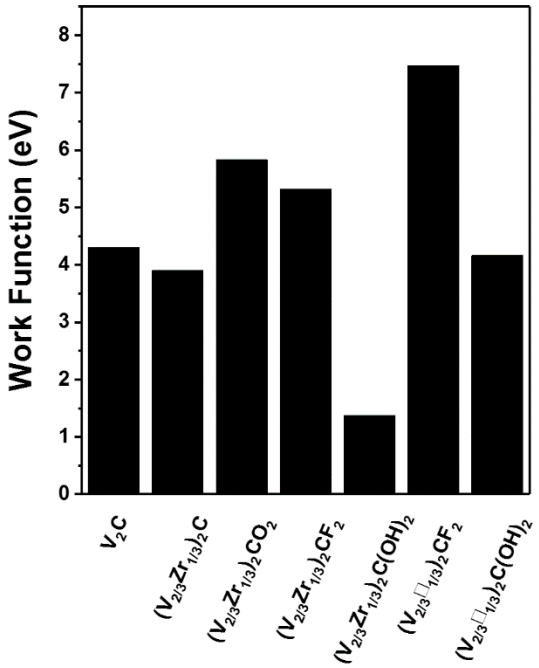


**Figure 3.14** Work functions of $V_2C$ MXene, pristine $(V_{2/3}Zr_{1/3})_2C$, bimetallic $(V_{2/3}Zr_{1/3})_2CX_2$ and vacancy-ordered $(V_{2/3}\square_{1/3})_2CX_2$ *i*-MXenes.

### 3.2.5 Summary

Our results show that modifying the stoichiometry of M and M' metals and/or surface functionalization of *i*-MXenes changes their properties. Therefore they are excellent candidates for applications in spintronics because their electric and magnetic properties can be tuned for specific purposes. In this study, $(V_{2/3}Zr_{1/3})_2CO_2$ and $(V_{2/3}\square_{1/3})_2CF_2$ and $(V_{2/3}\square_{1/3})_2C(OH)_2$ *i*-MXenes are FM half-semiconductor materials. The predicted $T_C$ for $(V_{2/3}Zr_{1/3})_2CO_2$ *i*-MXene (270 K) is higher than that of the experimentally reported 2D $CrI_3$ (45 K)[63] and $Cr_2Ge_2Te_6$ (66 K)[61]. Therefore, $(V_{2/3}Zr_{1/3})_2CO_2$ is the best candidate for spintronic applications. The surface functional groups on MXenes can dramatically change the character of their frontier orbitals, thereby affecting their work function. In particular, we found that $(V_{2/3}Zr_{1/3})_2C(OH)_2$ *i*-MXene can be used as an ultra-low work function electron emitter with work function as low as 1.37 eV. Conversely, the $(V_{2/3}\square_{1/3})_2CF_2$ *i*-MXene has a rather high WF of 7.47 eV and it can be used for holes injection in applications with requiring Schottky-barrier-free contacts. Overall, the results presented in this study establish a new family of MXenes with intrinsic magnetism, which makes them ideal candidates for both spintronic and electronic applications in the near future.

## 3.3 Magnetic Cr-based MXenes in valleytronics

MXenes have attracted great attentions in spintronics due to their tunable magnetic and electronic properties[32, 156-158]. However, no spin-valley couplings and valley polarizations were proposed for magnetic MXenes so far, even though asymmetric functionalization can naturally break the inversion symmetry of MXenes. In other words, previous studies overlooked the valley degrees of freedom of ferromagnetic MXenes despite theoretical predictions indicating that $Cr_2C$ MXenes display adjustable magnetisms and have high $T_C$ (or $T_N$) temperatures upon symmetric (or asymmetric) surface functionalization[159-161]. In this section, based on valleytronics potentials of MXenes described above, we proposed a general strategy for exploiting the asymmetric surface functionalization (Janus and mixed functionalization) of $Cr_2C$ MXenes with ferromagnetism to induce intrinsic ferrovalley polarizations. Asymmetric surface functionalization can break the inversion symmetry and can tune magnetic orders of $Cr_2C$ MXenes. The results reported in this section improve our understanding of the basic physical processes underlying exchange mechanisms in magnetic MXenes and they can help in identification of experimental opportunities for introducing robust ferrovalley properties in currently available MXenes.

### 3.3.1 $Cr_2C$ MXene Functionalization

For both $Cr_2CX_2$ and $Cr_2COX$ systems the surface functional groups can be placed in four different ways (**Figure 3.15**). The type II placement is the most energetically stable among them for both $Cr_2CX_2$ and Janus $Cr_2COX$ MXenes (**Table 3.2**).

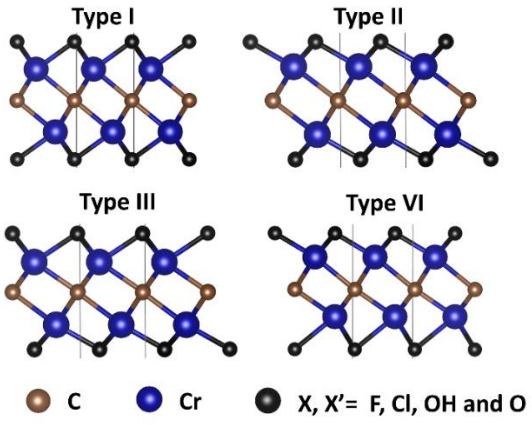


**Figure 3.15** Four possible types of $Cr_2C$ MXenes functionalization.

**Table 3.2** Four types of functionalization adsorption sites on $Cr_2CX_2$ and Janus $Cr_2COX$ MXenes. The most stable type is set to zero for each MXenes.

| MXenes | **Type I** | **Type II** | **Type III** | **Type VI** |
|---|---|---|---|---|
| $Cr_2CF_2$ | 0.52 | 0.00 | 0.17 | / |
| $Cr_2CCl_2$ | 0.56 | 0.00 | 0.23 | / |
| $Cr_2C(OH)_2$ | 2.64 | 0.00 | 0.13 | / |
| $Cr_2COF$ | 0.40 | 0.00 | 0.22 | 0.33 |
| $Cr_2COCl$ | 0.82 | 0.00 | 0.59 | 0.38 |
| $Cr_2COOH$ | 0.21 | 0.00 | 0.12 | 0.21 |

Although $Cr_2CX_2$ MXenes show inversion symmetry (the key to valley polarization), this inversion symmetry can be broken by surface engineering (Janus and mixed functionalization) (**Figure 3.16**). The structural information for all investigated $Cr_2CX_2$ and $Cr_2COX$ MXenes are summarized in **Table 3.3**.

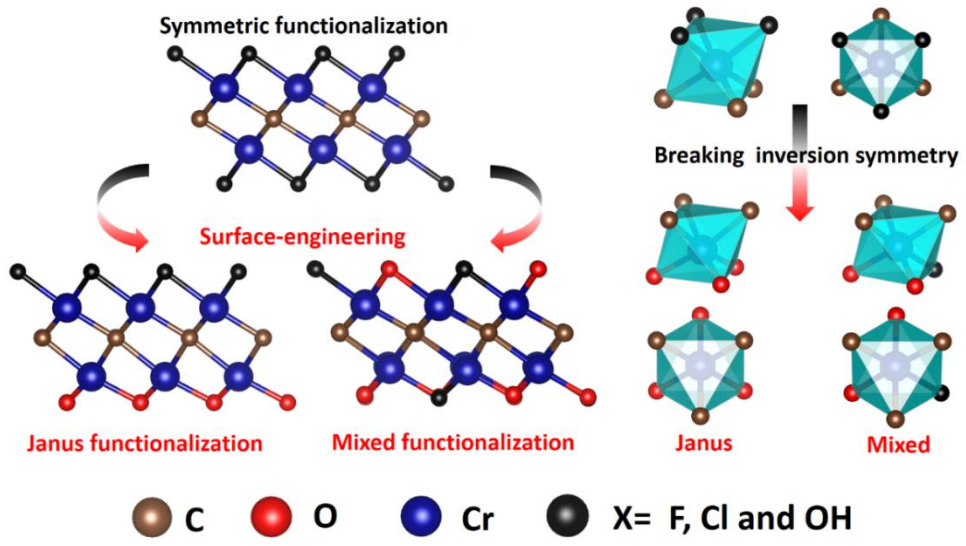


**Figure 3.16** Symmetric and asymmetric MXene functionalization (left) and a scheme showing the inversion symmetry breaking for Janus and mixed functionalizations of $Cr_2C$ MXenes (right).

**Table 3.3** Calculated structural and magnetic characteristics of $Cr_2CX_2$ and Janus $Cr_2COX$ MXenes. L is the lattice constant (in Å). Cr-C and Cr-X(X') are bond lengths (Å). Magnetic states include ferromagnetic (FM) and antiferromagnetic (AFM) states. M is magnetic moment ($\mu_B$). $J_1$, $J_2$ and $J_3$ are coupling constants (in meV). $T_C/T_N$ stands for the Curie and Neel temperatures (K). Band gaps are in spin-up and spin-down channels (eV). $\Delta K_{VBM}$ and $\Delta K_{CBM}$ stands for the valley splitting (meV).

| MXenes | $Cr_2CF_2$ | $Cr_2CCl_2$ | $Cr_2C(OH)_2$ | $Cr_2COF$ | $Cr_2COCl$ | $Cr_2COOH$ |
|---|---|---|---|---|---|---|
| **L (Å)** | 3.01 | 3.13 | 3.02 | 2.94 | 2.98 | 2.95 |
| **Cr-C** | 2.05 | 2.02 | 1.99 | 1.99 ($Cr_F$-C)<br>2.17 ($Cr_O$-C) | 1.96 ($Cr_{Cl}$-C)<br>2.10 ($Cr_O$-C) | 1.99 ($Cr_{OH}$-C)<br>2.16 ($Cr_O$-C) |
| **Cr-X(X')** | 2.12 | 2.46 | 2.14 (Cr-OH) | 2.11(Cr-F)<br>1.92(Cr-O) | 2.44(Cr-Cl)<br>1.95(Cr-O) | 2.12(Cr-OH)<br>1.93(Cr-O) |
| **Magnetic states** | AFM | AFM | AFM | FM | FM | FM |
| **M (Cr)** | ± 2.65 | ± 2.74 | ± 2.79 | 2.90 ($Cr_F$)<br>2.56 ($Cr_O$) | 2.75 ($Cr_{Cl}$)<br>2.57 ($Cr_O$) | 2.84 ($Cr_{OH}$)<br>2.59 ($Cr_O$) |
| $J_1$ | 62.14 | 181.39 | 154.83 | 24.61 | 14.37 | 24.02 |
| $J_2$ | 22.11 | 61.79 | 32.01 | 31.46 | 50.55 | 32.01 |
| $J_3$ | 56.07 | 78.4 | 53.74 | 14.64 | 8.74 | 6.44 |
| $T_C/T_N$ | 3830 | 6095 | 6095 | 1146 | 622 | 983 |
| **Gaps Up/down** | 3.40/3.40 | 2.28/2.28 | 1.55/1.55 | 0.40/3.46 | /2.54 | /3.26 |
| $\Delta K_{VBM}$ | / | / | / | 334 | -149 | 45 |
| $\Delta K_{CBM}$ | / | / | / | 421 | -139 | 140 |

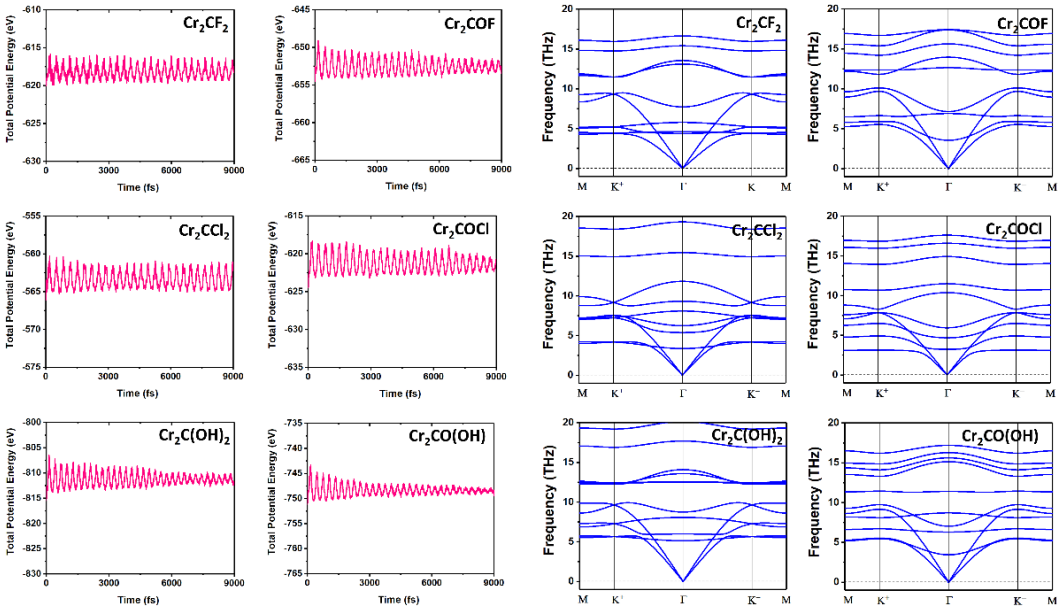


**Figure 3.17** Total potential energy of MXenes as a function of simulation time for $Cr_2CX_2$ and $Cr_2COX$ MXenes from ab-initio molecular dynamics (300K, 9 ps) (left). Phonon spectra for $Cr_2CX_2$ and $Cr_2COX$ MXenes (right).

All MXenes reported in **Table 3.3** are kinetically stable based on both AIMD simulations and phonon spectra calculations (**Figure 3.17**). AIMD simulations were performed at 300 K for 9 ps. $Cr_2C$ MXenes with mixed functionalization, *i.e.*, different concentrations of O and F on a (2 × 2 × 1) supercell, will be discussed later.

### 3.3.2 Critical Temperatures

To determine the preferred magnetic ground state structures of $Cr_2CX_2$ and $Cr_2COX$ system, the FM and three AFM states were analyzed (**Figure 3.18**). The exchange interaction can be conveniently studied by mapping the total energies of the systems with different magnetic orderings to the Ising model with the nearest-, next-nearest-, next-next-nearest-neighbor couplings $J_1$, $J_2$, and $J_3$, respectively.

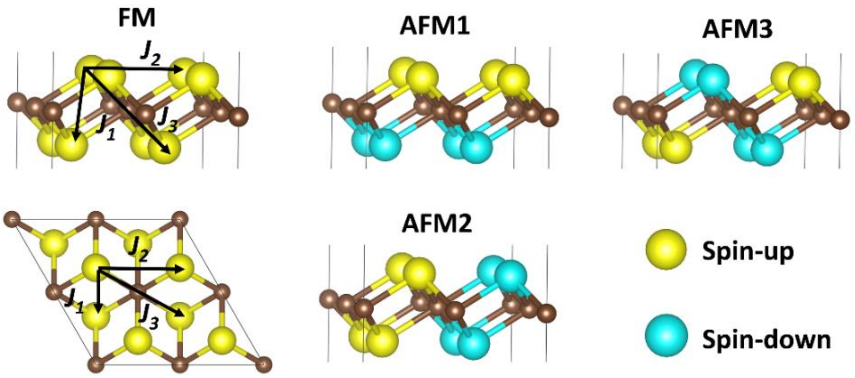


**Figure 3.18** FM and three AFM states for functionalized $Cr_2C$ MXenes.

To quantify the magnetic properties of $Cr_2CX_2$ and $Cr_2COX$ MXenes, the inter- ($J_1$ and $J_3$) and intra-plane ($J_2$) magnetic exchange coupling constants were investigated (**Table 3.3**). These results demonstrate that the intra-plane coupling between the Cr atoms in the upper- and lower-surfaces is strongly ferromagnetic, whereas the inter-plane interaction maintains the antiferromagnetic coupling. Our calculations of $T_C$ and $T_N$ reveal the high stability of the magnetic states, even above the room temperature (**Figure 3.19**). The $T_N$ of $Cr_2CX_2$ MXenes surpass 2000 K, corroborating previous studies[161]. $T_C$ of $Cr_2COF$, $Cr_2COCl$ and $Cr_2CO(OH)$ MXenes are 1146 K, 622 K and 983 K, respectively. The $T_C$ of $Cr_2CO_{0.75}F_{1.25}$ and $Cr_2CO_{1.25}F_{0.75}$ MXenes are 1648 K and 314 K, respectively (**Table 3.4**). The high $T_C$ of $Cr_2C$ MXenes with Janus and mixed functionalization are the key to potential applications in practical valleytronics devices.

**Table 3.4** Calculated structural and magnetic characteristics of two mixed MXenes. L is the lattice constant (in Å). Magnetic states include ferromagnetic (FM) and ferrimagnetic (FIM) states. $T_C/T_N$ stands for the Curie and Neel temperatures (in K). Band gaps are shown for spin-up and spin-down channels (in eV). $\Delta K_{VBM}$ and $\Delta K_{CBM}$ stands for the valley splitting (in meV).

| MXenes | L (Å) | Magnetic states | $T_C/T_N$ | Gaps Up/down | $\Delta K_{VBM}$ | $\Delta K_{CBM}$ |
|---|---|---|---|---|---|---|
| $Cr_2CO_{0.75}F_{1.25}$ | 5.96 | FIM | 1648 | 0.97/0.46 | 11 | 11 |
| $Cr_2CO_{1.25}F_{0.75}$ | 5.75 | FM | 314 | 0.31/2.66 | 15 | -12 |

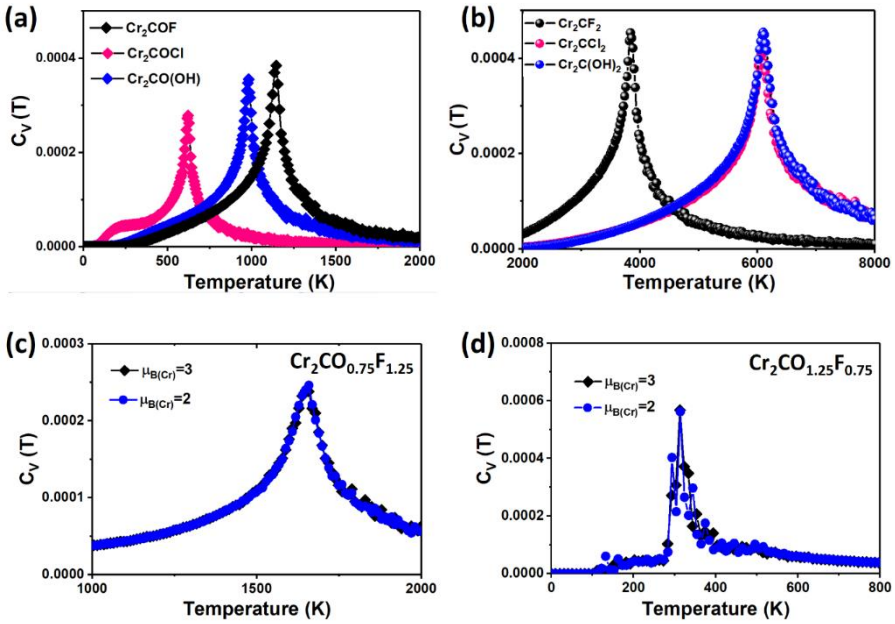


**Figure 3.19** Specific heat ($C_V$) calculated for $Cr_2CX_2$, $Cr_2COX$ and mixed $Cr_2C$ MXenes with respect to the temperature.

### 3.3.3 Electronic and Magnetic Properties

Our analysis of electronic states, spin polarization and magnetic properties of $Cr_2CF_2$ and $Cr_2COF$ MXenes is described in detail below (**Figure 3.20**). $Cr_2CF_2$ exhibits the AFM state with the super-exchange mechanism, whereas $Cr_2COF$ exhibits the FM state with the double-exchange mechanism. The spin-polarized charge densities of $Cr_2CF_2$ and $Cr_2COF$ are shown in **Figure 3.20**.

ELF maps (**Figure 3.20**) of $Cr_2CF_2$ and $Cr_2COF$ highlight the differences in 3d orbitals, with more itinerant *d* electrons in $Cr_2COF$ than in $Cr_2CF_2$. Itinerant *d* electrons induce increased spin polarization in neighboring C atoms. According to the local symmetry of the crystal field on Cr magnetic ions, $3d$ orbitals split into a non-degenerate $d_{z^2}$ orbital and two 2-fold degenerate $d_{x^2-y^2} + d_{xy}$ and $d_{yz} + d_{xz}$ orbitals. The electron-occupancy diagrams for $Cr_2CF_2$ and $Cr_2COF$ MXenes show that the model predicts partial filling of $d_{z^2}$ and $d_{x^2-y^2} + d_{xy}$ orbitals of Cr atoms. $Cr_F$ atoms (Cr atom bound to F atom) in the $Cr_2CF_2$ MXene have magnetic moments of 2.65 $\mu_B$, as expected for a formally $Cr_F^{3+}$ electronic configurations.

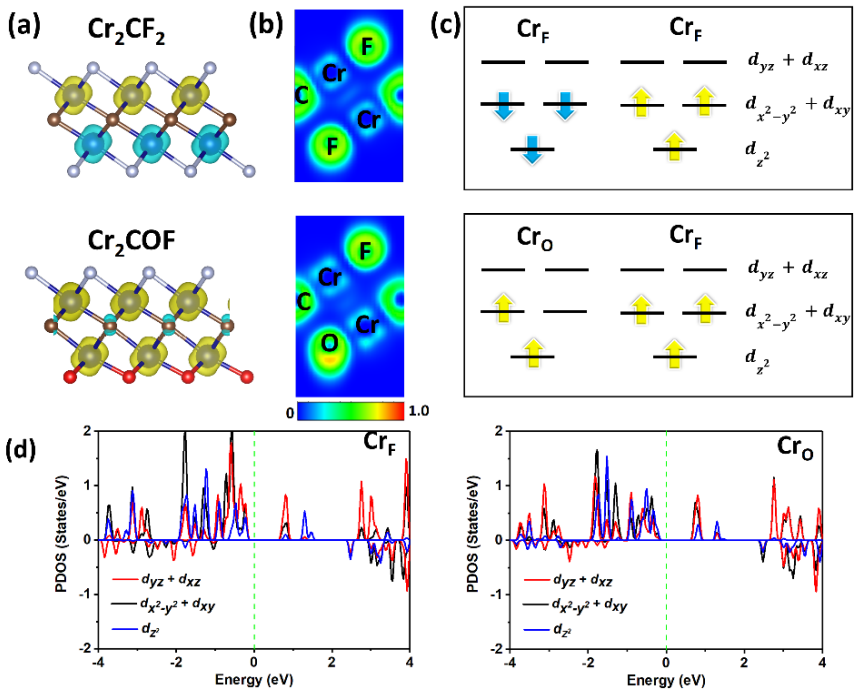


**Figure 3.20** (a) Spin polarized charge densities on $Cr_2CF_2$ and $Cr_2COF$ MXenes, where spin-up and spin-down densities are shown in yellow and blue, respectively. The isosurface is 0.045 e/Bohr$^3$. (b) ELF on $Cr_2CF_2$ and $Cr_2COF$ MXenes. The color scale (from 0 to 1) shows the probability. (c) The predicted occupations of 3*d* orbitals on Cr atoms in $Cr_2CF_2$ and $Cr_2COF$ MXenes. (d) PDOS of $Cr_2COF$ for $Cr_F$ and $Cr_O$ atoms.

Our calculations of local magnetic moments reveal that Cr atoms are in the high spin state with 3 unpaired d electrons ($d^{3\uparrow}$ spin configurations). The FM state of the $Cr_2COF$ MXene have a total magnetic moment of 5 $\mu_B$ (per unit cell), which is mainly contributed by Cr atoms. $Cr_O$ and $Cr_F$ atoms have magnetic moments of 2.56 and 2.90 $\mu_B$, again, as formally expected for $Cr_O^{4+}$ and $Cr_F^{3+}$ electronic configurations, with -0.38 $\mu_B$ on C atoms. In turn, Cr atoms are in the high spin state with 2 and 3 unpaired *d* electrons ($d^{2\uparrow}$ and $d^{3\uparrow}$ spin configurations). PDOS of $Cr_2COF$ can help us understand the magnetic properties of Cr-based MXenes. The atomic orbital of Cr-3*d* states contributes to the semiconductor states near the Fermi level, and the PDOS of $Cr_O$ and $Cr_F$ atoms are different due to the spin polarization induced by asymmetric functionalization. Similar results for symmetric cases of $Cr2CCl_2$ and $Cr_2C(OH)_2$ MXenes and Janus cases of $Cr_2COCl$ and $Cr_2CO(OH)$ MXenes are shown in **Figure 3.21**.

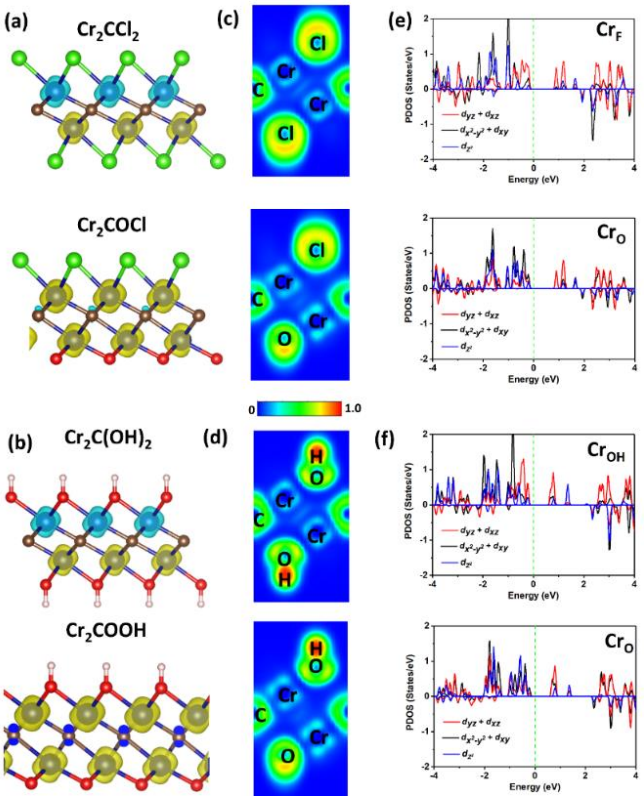


**Figure 3.21** Spin polarized charge densities on (a) $Cr_2CCl_2$ and $Cr_2COCl$ and (b) $Cr_2C(OH)_2$ and $Cr_2CO(OH)$ MXenes, where spin-up and spin-down densities are shown in yellow and blue, respectively. The isosurface is 0.045 e/Bohr$^3$. ELF of $Cr_2CCl_2$ and $Cr_2COCl$ (c) and $Cr_2C(OH)_2$ and $Cr_2CO(OH)$ MXenes (d). The color scale (from 0 to 1) shows the probability. PDOS of $Cr_2COCl$ (e) and $Cr_2CO(OH)$ MXenes (f).

### 3.3.4 Valleytronic Properties

Band structures, with and without SOC, and orbital-projected band structures of $Cr_2COF$ are shown in **Figure 3.22**. All $Cr_2CX_2$ considered herein are AFM semiconductors, whereas $Cr_2COX$ MXenes are FM semiconductors or half-metals (**Figure 3.22**). In particular, two band gaps in $Cr_2COF$ MXene are 0.40 eV and 3.46 eV in spin-up and spin-down channels, respectively. The band structure of $Cr_2COF$ MXene shows two degenerate valleys at $K^+$ and $K^-$. However, these valleys in the band structure of $Cr_2COF$ MXene become non-degenerate when considering the SOC effect. The valley splitting of $Cr_2COF$ MXene (energy difference between $K^+$ and $K^-$ at VBM and CBM) are $\Delta K_{VBM}$ = 334 meV and $\Delta K_{CBM}$ = 421 meV (**Figure 3.22**).

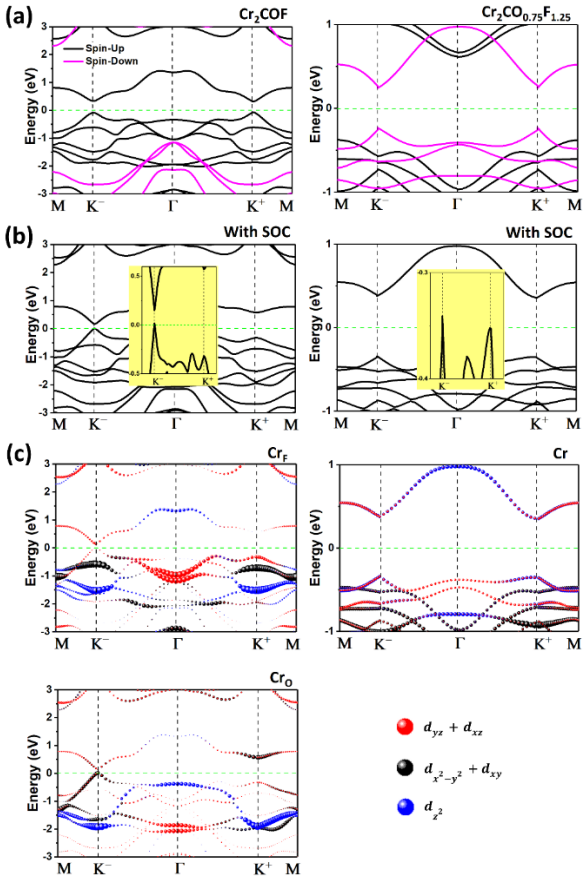


**Figure 3.22** (a) Band structures calculated at HSE06 level. Spin-up and spin-down bands are respectively denoted by black and pink lines. (b) Band structures with SOC. Details of valleys are shown in the insets. (c) Orbital projected band structures with SOC. Red, black and blue circles represent $d_{yz} + d_{xz}$, $d_{x^2-y^2} + d_{xy}$ and $d_{z^2}$ orbital composition. The sizes of the dots denote the weight of the contribution.

To better understand the intrinsic valley energy splitting of $Cr_2COF$ MXene, projected band structures are also shown in **Figure 3.22**. $Cr_F$ and $Cr_O$ atoms display different *d* orbital contributions: $d_{yz} + d_{xz}$ orbitals of $Cr_F$ contribute to both VBM and CBM; $d_{x^2-y^2} + d_{xy}$ orbitals of $Cr_O$ mainly contribute to VBM at $K^-$ and into CBM at $K^+$; and $d_{yz} + d_{xz}$ orbitals of $Cr_O$ mainly contribute to VBM at $K^+$ and CBM at $K^-$. Thus, different orbitals from one spin channel exist at different valleys, which is the fundamental ferrovalley characteristic.

Similar data for other asymmetrically functionalized MXenes are shown in **Figure 3.23**. The valley splitting identified in the band structures of $Cr_2CO(OH)$ MXene are similar to those of $Cr_2COF$ MXene (**Figure 3.23**). However, the valley polarization of $Cr_2COCl$ is opposite to that of $Cr_2COF$ due to different contributions of Cr-*3d* orbitals in two valleys. In summary, our

results show different orbital contributions at two valleys, thus intrinsically breaking valley degeneracy.

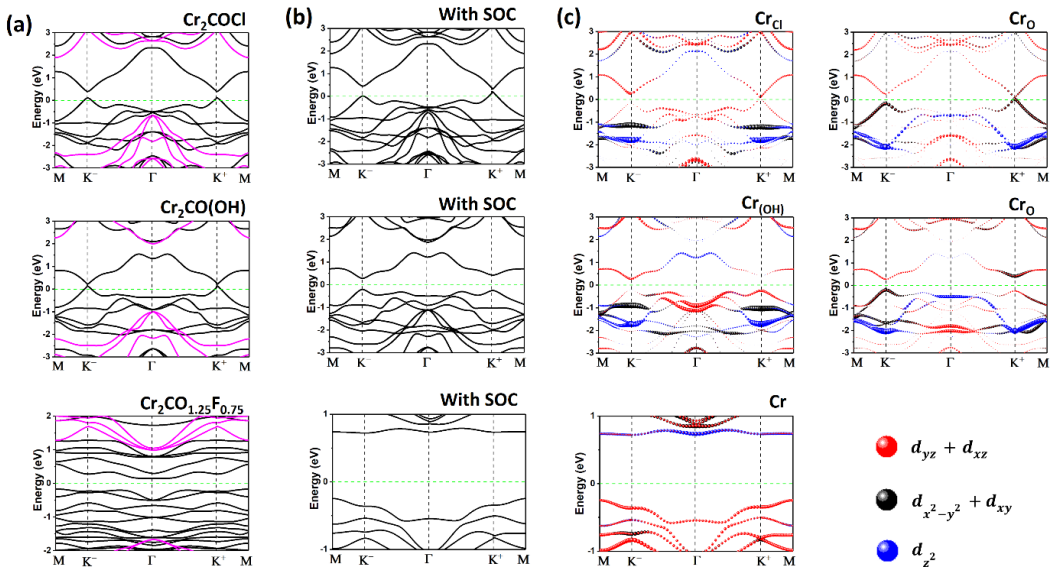


**Figure 3.23** (a) Band structures at HSE06 level. Spin-up and spin-down bands are respectively denoted by black and pink lines. (b) Band structures with SOC. (c) Orbital projected band structures with SOC. Red, black and blue circles represent $d_{yz} + d_{xz}$, $d_{x^2-y^2} + d_{xy}$ and $d_{z^2}$ orbital composition. The sizes of the dots denote the weight of contribution.

Overall, the results reveal spontaneous valley polarization in $Cr_2COX$ MXenes, as identified in the Berry curvature ($\Omega_{n,z}^{\uparrow(\downarrow)}$), which is the kernel parameter of electronic transport properties and is critical for various Hall effects. We calculated the spin-resolved nonzero $z$-component $\Omega_{n,z}^{\uparrow(\downarrow)}$ by Kubo formula derivation, due to broken time-reversal and space inversion symmetry. As a results, the absolute values of the Berry curvatures of one valley of $Cr_2COF$ (and $Cr_2CO(OH)$) MXene became stronger than those of the opposite valley of this MXene (**Figures 3.24 and 3.25**).

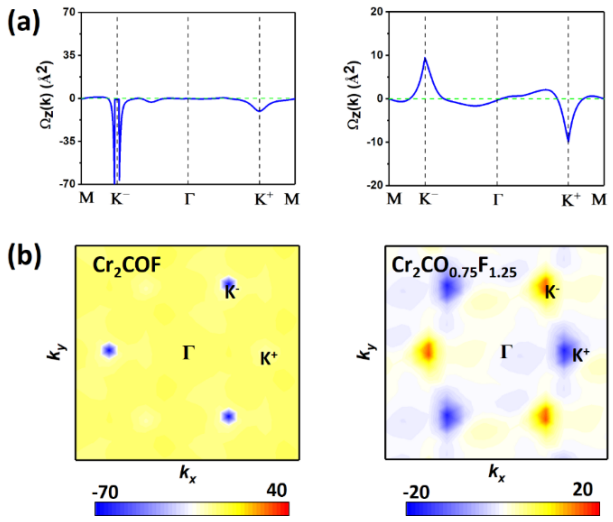


**Figure 3.24** Berry curvatures of $Cr_2COF$ and $Cr_2CO_{0.75}F_{1.25}$ along the high-symmetry points (a) and in the full Brillouin zone (b). The unit of Berry curvatures is $Å^2$.

In turn, the Berry curvatures of two different valleys of $Cr_2COCl$ MXene have opposite signs (**Figure 3.25**). Moreover, the opposite signs of Berry curvatures of different valleys of the $Cr_2CO_{0.75}F_{1.25}$ MXene suggest the valley Hall effect (**Figure 3.24**). The $Cr_2CO_{1.25}F_{0.75}$ MXene exhibits similar characteristics (**Figure 3.25**). Based on the above, carriers (for example, spin-up holes) in $Cr_2C$ MXenes with Janus or mixed functionalization can gain different transverse velocities at two valleys under an in-plane electric field.

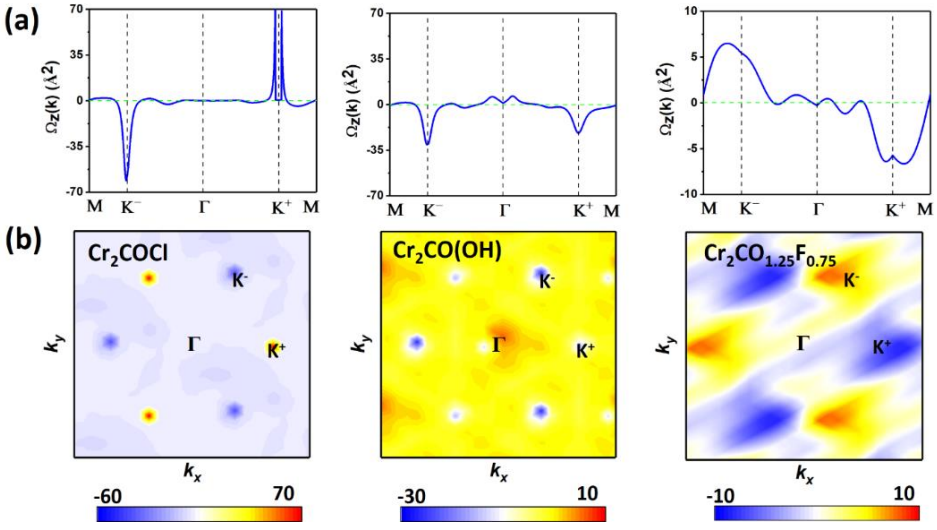


**Figure 3.25** Berry curvatures of $Cr_2COCl$, $Cr_2CO(OH)$ and $Cr_2CO_{1.25}F_{0.75}$ along high-symmetry points (a) and in the full Brillouin zone (b). Unit of Berry curvatures is $Å^2$.

### 3.3.5 Valley Hall effect

Upon applying an out-of-plane electric field, the spin-up holes will produce a net transverse spin/valley current due to the Berry-curvature-driven anomalous velocity of Bloch electrons. The external magnetic field reverses the magnetization direction, thereby producing a spin/valley Hall current with opposite spins and valley indices. Under these conditions, we can control the spin/valley polarization by inducing carrier doping and applying an external magnetic field, in addition to detecting the Hall effect by transversal voltage. Therefore, we field-tuned valley splitting by calculating $\Delta K_{VBM}$ of the $Cr_2COF$ MXene as the magnetization direction rotates from the *x* direction (in-plane) to the *z* direction (out-of-plane).

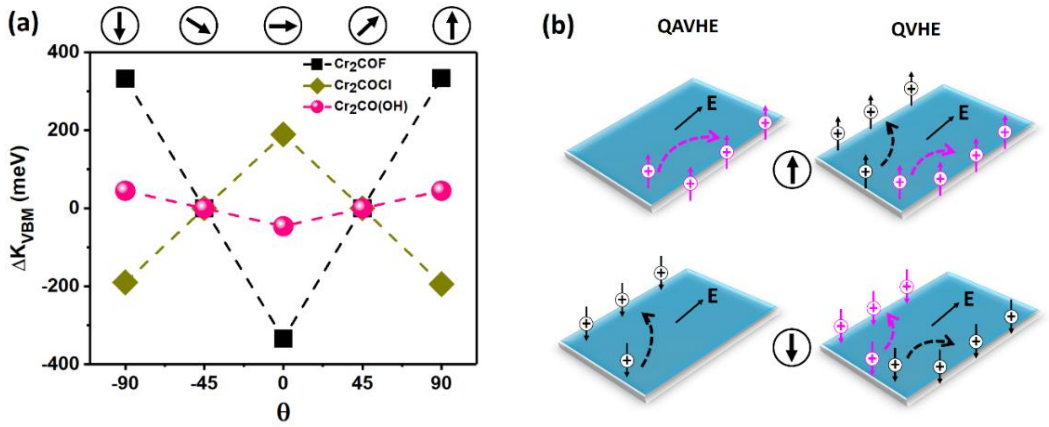


**Figure 3.26** (a) Valley splitting $\Delta K_{VBM}$ as a function of magnetization direction. The black arrows in circles show the magnetization direction (θ) in the xz plane (between the magnetic quantization axis and the monolayer) from -90 to 90. (b) Schematic diagram of rapid carrier transfer and QVHE and QAVHE effects in $Cr_2C$ MXenes. The positive sign in circles denotes the hole. Holes depicted in pink and black denote spin-up and spin-down channels, respectively. *E* is an applied in-plane electric field.

Valley polarization can be continuously tuned by rotating the magnetization direction (**Figure 3.26 and 3.27**) because the contributions from Cr-*3d* orbitals in two valleys vary with the rotation of the magnetization direction (**Figure 3.28**). Accordingly, valley polarization can be manipulated by applying an external magnetic field in a readily accessible experimental setup (**Figure 3.28b**). When $Cr_2COF$ (or $Cr_2CO(OH)$) has a positive valley polarization, most

carriers (spin-up holes) gain transverse velocities towards the right side under an in-plane electric field. Only one type of carrier comes from a single valley, *i.e.*, QAVHE effect (**Figure 3.28b**), resulting in an additional charge Hall current.

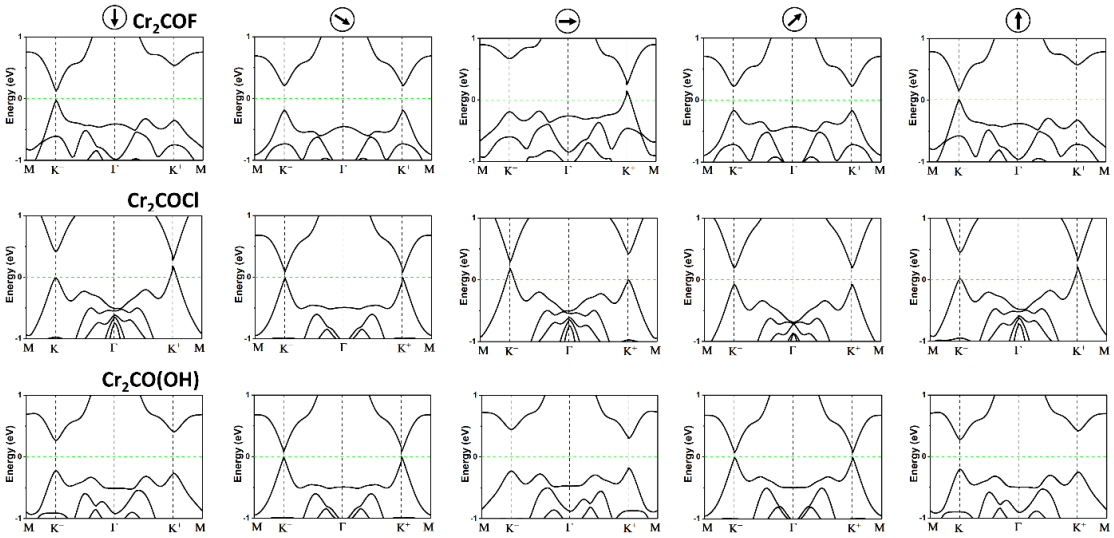


**Figure 3.27** Band structures of $Cr_2COX$ with SOC at HSE06 level. The black arrows in circles show the magnetization direction (θ) in the xz plane from -90 to 90.

Moreover, the carriers in inequivalent valleys will gain opposite velocities QVHE when injecting holes and applying an in-plane electric field to $Cr_2COCl$ MXene. The valley Hall effect can be demonstrated by optoelectronic measurements. Under the excitation of a circularly polarized laser, valley-polarized electrons and holes can be injected due to optical selection rules, forming a charge Hall current. Consequently, the sign change of Berry curvatures in different valleys is a new form of the Hall effect.

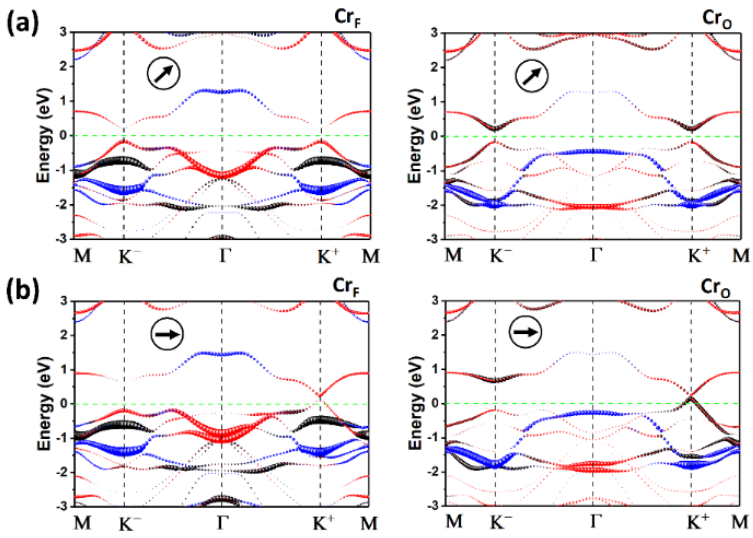


**Figure 3.28** Orbital projected band structures of $Cr_2COF$ MXene with SOC when (a) θ = 45 and (b) θ = 0. Red, black and blue circles represent $d_{yz} + d_{xz}$, $d_{x^2-y^2} + d_{xy}$ and $d_{z^2}$ orbital composition. The sizes of dots denote the weight of contribution.

### 3.3.6 Antiferrovalley

We also investigated band structures in the Janus $Cr_2TiC_2FCl$ MXene at the HSE06 level, given the presence of many magnetic states in exfoliated $Cr_2TiC_2$ MXenes[162-165], as well as its spin polarization and magnetic properties (**Figure 3.29**). $Cr_2TiC_2FCl$ MXene is a well-known bipolar AFM semiconductor with local spin polarizations at valence and conduction bands and a net magnetic moment of zero. We found that the intrinsic valley polarization of $Cr_2TiC_2FCl$ MXene is 20 meV, and its Berry curvatures at two K points have opposite signs (**Figure 3.29**). Such a valley degree of freedom has been detected in AFM materials (*i.e.*, antiferrovalley), such as $MnPX_3$ (X = S, Se) [166] and $VSe_2$ bilayers[167], thus supporting the new antiferrovalley characteristic of bipolar AFM $Cr_2TiC_2FCl$ MXene. Thus, the new antiferrovalley properties of these materials may be manipulated by carrier doping, similarly to bipolar AFM materials with applications in spintronics[168, 169].

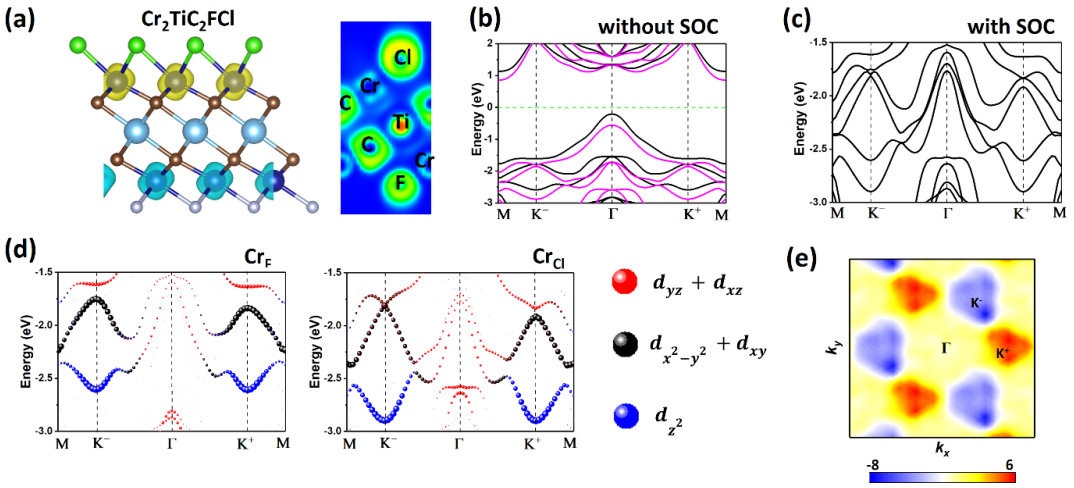


**Figure 3.29** (a) Spin polarized charge densities and electron localization functions. Spin-up and spin-down densities are shown in yellow and blue, respectively. The isosurface is 0.045 e·Bohr$^{-3}$. The color scale (from 0 to 1) shows the probability. (b) Band structures at HSE06 level. Spin-up and spin-down bands are respectively denoted by black and pink lines. (c) Band structures with SOC. (d) Orbital projected band structures with SOC. Red, black and blue circles represent $d_{yz} + d_{xz}$, $d_{x^2-y^2} + d_{xy}$ and $d_{z^2}$ orbital composition. The sizes of dots denote the weight of contribution. (e) Berry curvatures in the full Brillouin zone. Unit of Berry curvatures is Å$^2$.

### 3.3.7 Summary

We investigated the valleytronics properties of $Cr_2COX$ MXenes with Janus and mixed functionalization. These 2D nanomaterials exhibit intrinsic valley polarization in band structures due to the naturally broken inversion symmetry driven by surface engineering (functionalization). Janus $Cr_2COX$ (X= F, Cl and OH) MXenes are ideal candidates for ferrovalley materials because they have high $T_C$ and robustly intrinsic spin and valley polarization. In particular, $Cr_2COF$ MXene stands out as the optimal candidate for its valley polarization (334 meV) at two inequivalent K points, but mixed $Cr_2CO_{0.75}F_{1.25}$ and $Cr_2CO_{1.25}F_{0.75}$ MXenes also exhibit spin and valley polarization. The underlying physical mechanisms of the valley polarization in Janus and mixed functionalized $Cr_2C$ MXenes derives from different Cr-3*d* orbital contributions in valleys. Berry curvature calculations reveal the spontaneous valley polarization of Janus and mixed functionalized $Cr_2C$ MXenes. Moreover, the bipolar AFM $Cr_2TiC_2FCl$ MXene exhibits intrinsic valley polarization, which provides a

new opportunity for designing antiferrovalley materials. Our work establishes a promising platform for probing valleytronics in MXenes and an experimentally viable approach (*i.e.*, surface engineering) for chemically exfoliated MXenes.

## 3.4 $VS_4$ nanowire: 1D AFM semiconductor

Few materials can be isolated as true 1D materials, for example $NbSe_3$[44], which are joined in quasi-1D materials (bundles) through Van der Waals interaction. Several 1D FM compounds have been proposed for spintronics applications, such as metal trihydride molecular nanowires (NWs)[170], 1D metal benzenetetramine coordination polymers[171], Co-dithiolene molecular wires[172], transition metal tribromides NWs[173], transition metal trichalcogenides NWs[174], and transition metal chalcogenides NWs[15]. These materials have been theoretically investigated for their electronic and magnetic properties, but not as much for their spintronic properties, due to the lack of experimental reports.

The Vanadium tetrasulfide ($VS_4$) is found in nature as a mineral[175]. Its linear chain-like structure is composed of two $S_2^{-2}$ moieties connecting $V^{4+}$ centers. Different chains are bound together by vdW forces to form quasi-1D nanorods. Possible oxidation states of V ions induce different magnetic properties of different materials, such as Vanadium dichalcogenides ($VX_2$, X = S, Se) monolayers[176, 177], MXenes ($VX_2$, X = C, N)[156, 178], and Haeckelite $VS_2$[179]. According to these results, magnetism in $VS_4$ may be overlooked. In addition, the geometric, electronic and magnetic properties of $VS_4$ as a 1D NW are not clearly understood yet. This section will show that magnetic properties of $VS_4$ are affected by its dimensionality and how $VS_4$ can be used for spintronic applications.

### 3.4.1 Structural analysis

The primitive cell of $VS_4$ bulk phase (C2/c #15) in which each V atom is coordinated with eight S atoms to form four dimers is shown in **Figure 3.30**. From the bulk phase, we built the unite cell of the isolated $VS_4$ NW. The geometric details of the $VS_4$ bulk phase and of the isolated $VS_4$ NW are summarized in **Table 3.2**.

Both the bulk and isolate NW phases of $VS_4$ are dynamically stable, as shown by phonon dispersions (**Figure 3.30c**). Moreover, the stability of these NWs is also confirmed by AIMD simulation (**Figure 3.30d**) at room temperature (300 K), suggesting that individual NWs can be isolated.

**Table 3.5** Structural parameters, electronic and magnetic properties of the bulk phase and isolated NW of $VS_4$. $E_{form}$ is the formation energy (in eV). $L_{S\text{-}S}$ is S dimer bond-length (Å). $L_{V\text{-}V}$ is the distance of V atoms. $L_{V\text{-}S}$ is the V-S bond length. $E_g$ is the band gap. $E_{ex}$ is the exchange energy (in eV). M ($\mu_B$) is the local magnetic moment on V atoms.

| Configurations | $E_{form}$ | $L_{S\text{-}S}$ | $L_{V\text{-}V}$ | $L_{V\text{-}S}$ | $E_g$ | $E_{ex}$ | M |
|---|---|---|---|---|---|---|---|
| Bulk | -2.59 | 2.03 | 2.77, 3.20 | 2.54, 2.39 | 2.24 | 0.961 | 1.15 |
| Isolated NW | -2.06 | 2.03 | 2.77, 3.22 | 2.55, 2.39 | 2.65 | 0.948 | 1.17 |

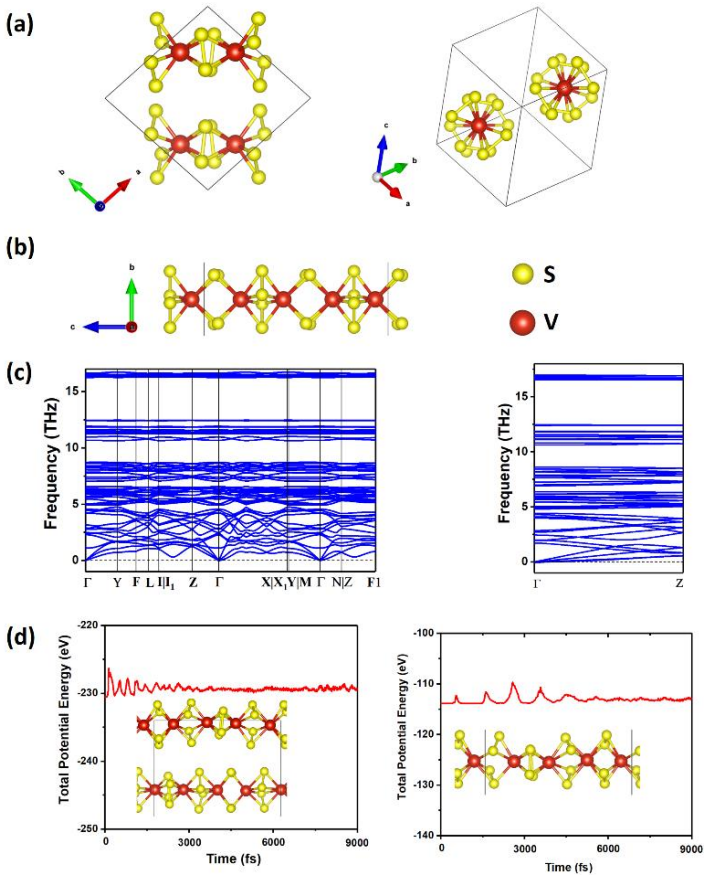


**Figure 3.30** (a) Primitive cell of the $VS_4$ bulk phase from two directions, along [001] direction (left) and along [111] direction (right). (b) Isolated $VS_4$ NW. The unit cell is marked by the black lines. (c) Phonon spectra and (d) total potential energy of NWs as a function of simulation time for the $VS_4$ bulk phase (conventional cell) and the isolated $VS_4$ NW by using AIMD. The inset shows the corresponding structure after the simulation for 9 ps.

### 3.4.2 Electronic and magnetic properties

Both the $VS_4$ bulk phase and the isolated $VS_4$ NW have an AFM ground state, and their stability is given by $E_{ex}$ (**Table 3.5**). The magnetic momentum of V is similar in the bulk phase and in the isolated NW (1.15 and 1.17 $\mu_B$). The bulk phase has an indirect band gap of 2.24 eV between the Y and Z points (**Figure 3.31**). The calculated electronic band gap is larger than the experimental optical band gap of $VS_4$ films (approximately 1.35 eV)[43]. This difference can be attributed to the experimental conditions, depending on S partial pressures of synthesis and on the morphology of the sample. Moreover, the bulk phase is a theoretically perfect crystal, which is unlikely to occur in the family of low-dimensional compounds. The spin density (**Figure 3.31**) shows the AFM G-type motif of the material[180]. VBM and CBM of the $VS_4$ bulk phase are formed by the overlap of S-2*p* orbitals with V-3*d* levels. V-3*d* orbitals split into a non-degenerate $d_{z^2}$ orbital and into two 2-fold degenerate $d_{x^2-y^2} + d_{xy}$ and $d_{yz} + d_{xz}$ orbitals. Local V-3*d* orbitals induce an antiparallel spin arrangement on neighboring V via the double-exchange mechanism. VBM and CBM of the $VS_4$ bulk phase derive from the S-2*p* orbitals and V $d_{yz} + d_{xz}$ orbitals.

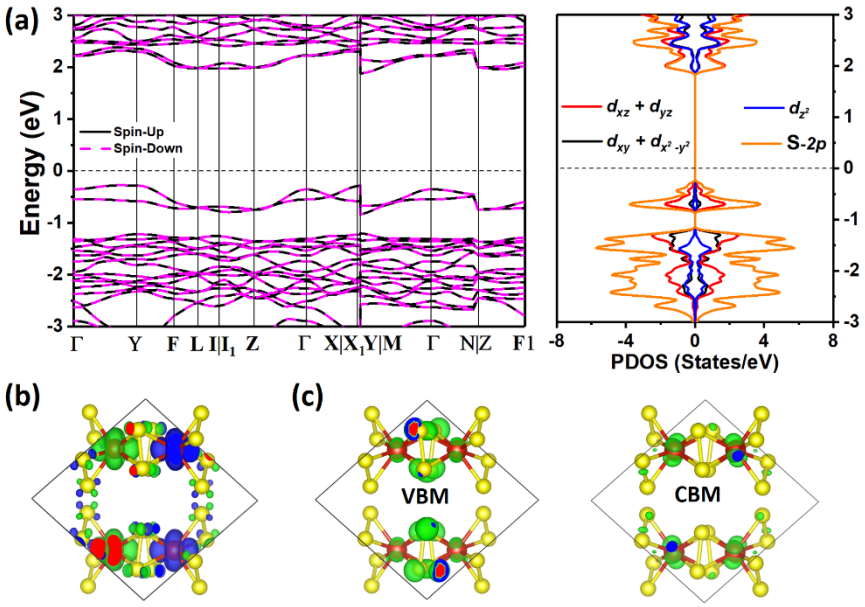


**Figure 3.31** (a) Band structures and PDOS and (b) spin-polarized density of the $VS_4$ bulk phase, where spin-up and spin-down densities are shown in green and blue, respectively. (c) VBM and CBM are shown in green. The isosurface is 0.005 e/Bohr$^3$.

Compared to the $VS_4$ bulk phase, electronic structures of the isolated $VS_4$ NW reflects the lower dimensionality of the material, which induces a larger band-gap of 2.65 eV with a higher density of state (**Figure 3.32**). The lack of interactions between different $VS_4$ chains affects the nature of the bond. A larger contribution of VBM and CBM of the isolated $VS_4$ NW derives from S-2*p* states (**Figure 3.32**). VBM and the CBM of the V-3*d* orbitals of the isolated NW are different from those of the $VS_4$ bulk phase. V $d_{x^2-y^2} + d_{xy}$ orbitals of the isolated $VS_4$ NW contribute to the VBM and CBM.

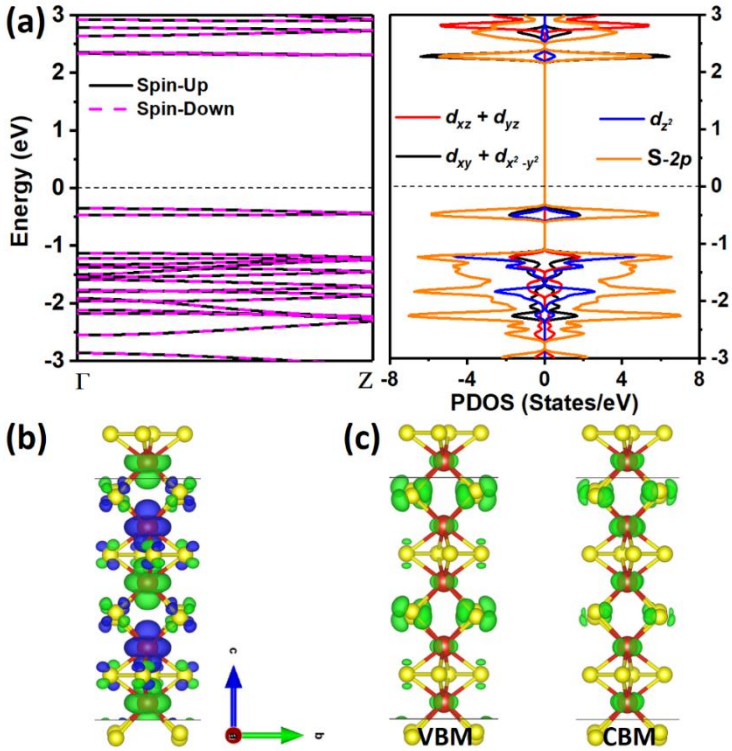


**Figure 3.32** (a) Band structures and PDOS and (b) spin-polarized density of the isolated $VS_4$ NW, where spin-up and spin-down densities are shown in green and blue, respectively. (c) VBM and CBM are shown in green. The isosurface is 0.005 e/Bohr$^3$.

To gain insight into the change of electronic and magnetic properties between the $VS_4$ bulk phase and the isolated $VS_4$ NW, ELFs for the $VS_4$ bulk phase and for the isolated $VS_4$ NW (**Figure 3.33**) were plotted. ELFs of S atoms in the $VS_4$ bulk phase are more localized than that of the isolated $VS_4$ NW, due to Van der Waals interactions between those NWs in the $VS_4$ bulk phase. Moreover, $VS_4$ NW has distinct characteristics of localized d electrons of V atoms: more

itinerant V-3*d* electrons in the isolated $VS_4$ NW than that in the $VS_4$ bulk phase. Itinerant V-3*d* electrons can induce spin polarization of neighboring S atoms, *i.e.* an anti-parallel spin arrangement via a double-exchange mechanism. In addition, PDOS of V-3*d* orbitals differ between the $VS_4$ bulk phase and the isolated $VS_4$ NW. This difference in electronic properties does not affect the AFM character of $VS_4$ NW with a double-exchange mechanism.

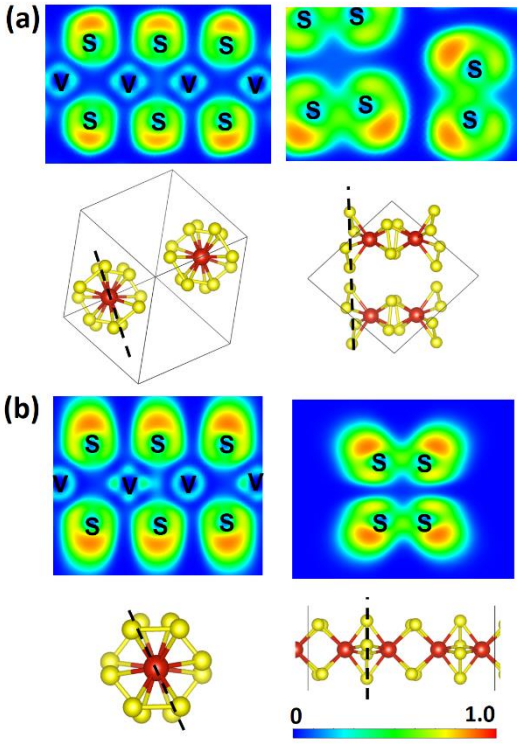


**Figure 3.33** ELF maps of (a) the $VS_4$ bulk phase and (b) isolated $VS_4$ NW. The dot line is the chosen direction of the ELF slice. The unit of the color scale is probability.

### 3.4.3 HMAF in NWs

The effect of doping concentrations of 0.1, 0.3, and 0.5 electron (and hole) per unit cell of the isolated $VS_4$ NW (i.e., 0.83, 2.50, and 4.17 $\times 10^6$ $cm^{-1}$) was investigated. The bulk phase did not further considered. The isolated $VS_4$ NW with carrier doping is HMAF, exhibiting complete spin-polarization around the Fermi level (**Figure 3.34**). This is because the carrier doping shifts the Fermi level and induces spin polarization on S and V atoms. The magnetic momentum of V atoms is affected by the carrier doping, and the magnetic momentum of each S atom is very

small. The isolated $VS_4$ NW retains its AFM state. PDOS show that main contributions around the Fermi level derive from V $d_{x^2-y^2} + d_{xy}$ orbitals and S-2$p$ orbitals. The $E_{ex}$ is rapidly decreased under hole doping and increased under electron doping. Our results indicate that the AFM state of the isolated $VS_4$ NW is stable when injected with a low concentration of carriers.

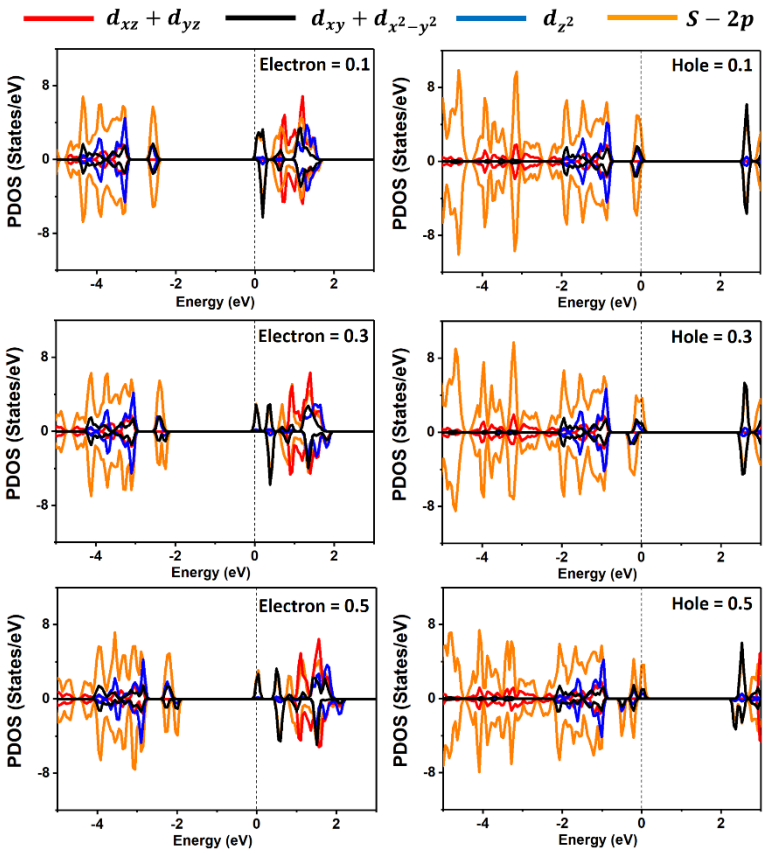


**Figure 3.34** PDOS of the isolated $VS_4$ NW under carrier doping with a carrier concentration of 0.1, 0.3 and 0.5 electron (and hole) per unit cell.

### 3.4.4 Protection of nanowires

In general, the influence of the environment (for example, oxidation) on the transport properties and electrical contacts of NWs limit their applications. Therefore, protecting NWs for preserving the electronic and magnetic properties of the isolated $VS_4$ NW have to be tested for spintronic applications. Nanotubes may protect NWs to prevent oxidation and maintaining electronic and magnetic properties[44]. The nanocable, composed of insulating outer sheaths and a NW core, may server as a model. A designed nanocable, including the isolated $VS_4$ NW

and a 1×1×5 (8, 8) boron nitride (BN) zigzag nanotube, is constructed (**Figure 3.35**), where the lattice mismatch is approximately 4.5%. The distance between the $VS_4$ NW and the wall of the BN nanotube is approximately 3.57 Å. The electronic and magnetic properties of the $VS_4$-BN nanocable is similar to that of the isolated $VS_4$ NW. Therefore, the spin polarization of the nanocable still derives from the inner NW, while the BN nanotube has a negligible effect on the NW. Such a hybrid structure could be used for spintronics applications.

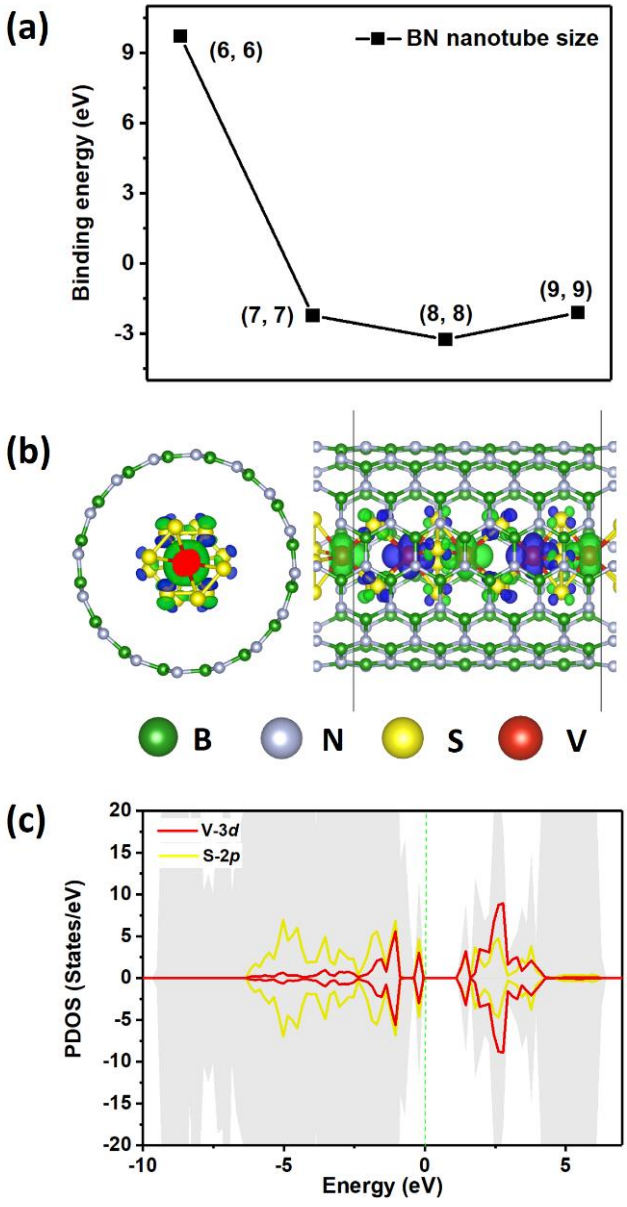


**Figure 3.35** (a) Binding energies ($E_b$) of the isolated $VS_4$ NW inside BN nanotubes of different sizes (b) Spin polarization density of the nanocable. (c) PDOS of the nanocable at PBE +U level (U = 3). The gray shadow is the total density of states.

### 3.4.5 Summary

In this section, we presented a new strategy in $VS_4$ NWs towards AFM spintronics. After confirming the stability of $VS_4$ NWs, we investigated the electronic and magnetic properties of $VS_4$ NWs. The isolate $VS_4$ NW is an AFM semiconductor with a high $T_N$ (210 K). We found that carrier doping can separate the spin degeneracy to induce local spin polarization. The isolated $VS_4$ NW represent the HMAF resulting from carrier doping, which can be achieved with gate voltages. Our results indicate that the isolated $VS_4$ NW is a promising 1D material for AFM spintronic applications. We further considered the protection of NWs. BN nanotubes can provide the protection of $VS_4$ NWs for preventing oxidation and for preserving their electronic and magnetic properties. Our results propose a new way for applying 1D NWs in AFM spintronics by inducing HMAF.

## 3.5 Magnetic Janus TMDs

2D TMDs have exhibited a wide variety of novel electronic and optical properties due to adjustable band gaps. However, the majority of 2D TMDs is intrinsically non-magnetic. Extrinsic magnetism can be also introduced into the non-magnetic 2D TMDs by defects, doping, and so on. However, these methods are not easy to control in applications. Therefore, the design of new, intrinsically magnetic, TMDs represents an attractive opportunity to explore their potential for spintronics.

The synthesis of asymmetrical TMDs monolayers has been performed (*e.g.*, $MoS_2$ → MoSSe, where top-layer S atoms were fully replaced with Se atoms[39, 40]). Although Janus TMDs have attracted great attention due to the existence of vertical dipoles, Mo/W-based Janus TMDs are not intrinsically magnetic. Therefore, a natural question arises: can the Janus TMDs with intrinsic ferromagnetism and high spin-polarization be achieved when Janus TMDs contained magnetic atoms as V, Cr and Mn? We systematically investigated the geometry, stability, electronic and magnetic properties of TMXX' (TM= V, Cr and Mn; X, X' = S, Se and Te, $X \neq X'$). Various magnetic and electronic properties of Janus TMXX' are desirable for future spintronic applications.

### 3.5.1 Structure and stability

The structure of TMXX' composes of one TM atom layer sandwiched by two different chalcogen atoms (S, Se, and Te) (**Figure 3.36**). Nine types of Janus TMXX' structures were investigated and their structural parameters are summarized in **Table 3.6** together with their electronic structure properties. The difference in atomic size and electronegativity of X and X' breaks the pristine TMDs structural symmetry and gives rise to inequivalent TM-X and TM-X' bond lengths. To determine the preferred magnetic ground state structures of TMXX' systems, the collinear FM and AFM states are considered as shown in **Figure 3.36**. Their magnetic properties will be discussed later.

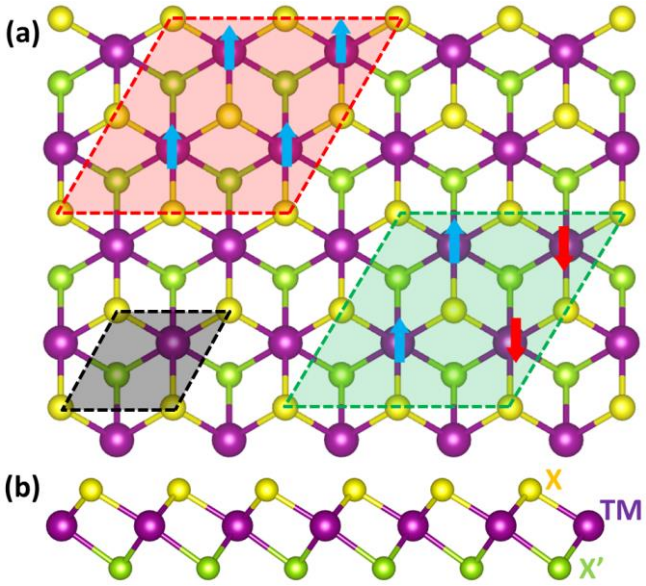


**Figure 3.36** A top (a) and a side (b) view of TMXX'. The rhombic unit cell is marked by a black dotted line. FM and AFM states are marked by red and green dotted lines, respectively.

**Table 3.6** The calculated structural parameters and electronic and magnetic properties of TMXX'. L is the lattice constant (in Å). $d_{TM}$ is the bond length (in Å). E.S. denotes the electronic structure (HM or M stands for half metal and metal). *J* is the magnetic coupling constant. $T_C$ is Curie temperature (in K). $M_{tot}$ is the total magnetic moment (in $\mu_B$).

| Structure | L (Å) | $d_{TM-S}$(Å) | $d_{TM-Se}$(Å) | $d_{TM-Te}$(Å) | E.S. | *J* (meV) | *Tc* (K) | $M_{tot}$ ($\mu_B$) |
|---|---|---|---|---|---|---|---|---|
| VSSe | 3.413 | 2.389 | 2.538 | - | HM | 5.16 | 420 | 1.05 |
| VSTe | 3.528 | 2.368 | - | 2.907 | M | 2.04 | 165 | 1.76 |
| VSeTe | 3.597 | - | 2.519 | 2.793 | M | 3.83 | 310 | 1.45 |
| CrSSe | 3.384 | 2.352 | 2.608 | - | M | 2.63 | 215 | 2.55 |
| CrSTe | 3.478 | 2.356 | - | 2.873 | M | 3.04 | 250 | 2.91 |
| CrSeTe | 3.565 | - | 2.497 | 2.849 | M | 2.35 | 190 | 2.81 |
| MnSSe | 3.533 | 2.394 | 2.520 | - | HM | 2.27 | 185 | 3.00 |
| MnSTe | 3.623 | 2.399 | - | 2.782 | M | 1.07 | 85 | 3.29 |
| MnSeTe | 3.704 | - | 2.537 | 2.772 | M | 1.43 | 115 | 3.23 |

To further confirm the dynamical stability of TMXX', their phonon spectra were calculated as shown in **Figure 3.37**. There are no negative frequency phonons of TMXX'. All these results indicate that TMXX' monolayers are dynamically stable and they could exist as free-standing 2D monolayers.

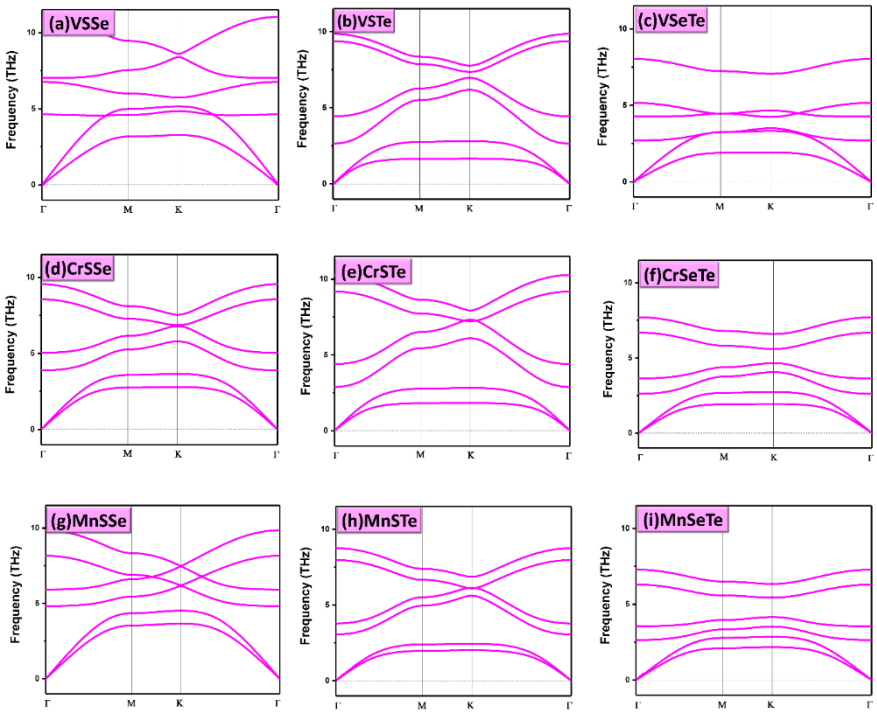


**Figure 3.37** Phonon spectrum for TMXX' monolayers.

### 3.5.2 Electronic and magnetic properties

To further explore potential applications of Janus TMXX' in spintronics, electronic properties of Janus TMXX' materials together with their magnetic properties were investigated and they are reported in **Table 3.6**. All TMXX' are predicted to be ferromagnetic metals, except MnSSe and VSSe. Magnetic moments are mainly contributed by TM atoms. X and X' atom are anti-parallelly polarized with a very small magnetic moment.

The magnetic ground states of the Janus TMXX' monolayers were investigated, Employing a (2 × 2) supercell with two typical magnetic configurations (FM and AFM states). By calculating $E_{ex}$, all TMXX' have a ferromagnetic ground states, in agreement with the previous study of 2D TMDs materials[181] . The total energy of the FM state can be expressed as $E_{FM} = E_0 - 3J|m|^2$, where $E_0$ represents the total energy in non-magnetic states. And the total energy of the AFM states can be expressed as $E_{AFM} = E_0 + J|m|^2$. Therefore, the exchange parameter can be calculated as $J = (E_{AFM} - E_{FM})/4|m|^2$. The $J$ value for all Janus TMXX' monolayers are also summarized in **Table 3.6**. The temperature dependence of magnetic

moments is shown in **Figure 3.38**. The $T_C$ for VSSe and VSeTe are higher than room temperature, indicating their potential application in practical devices. Moreover, the $T_C$ value for VSSe, VSTe and VSeTe are comparable with previous Monte Carlo simulations results for $VS_2$, $VSe_2$ and $VTe_2$ monolayers (**Figure 3.38**).

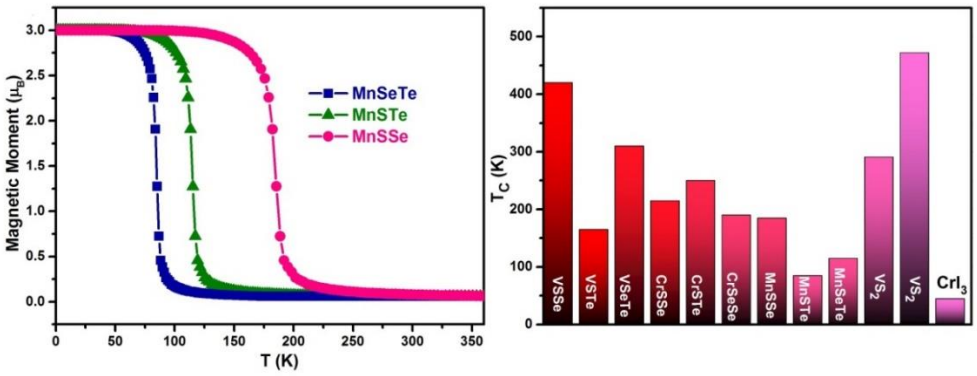


**Figure 3.38** Magnetic moments dependence on temperature for the MnXX' monolayers (Left). Curie temperature for all Janus TMDs monolayer and for 2D $CrI_3$ (45 K), $VS_2$ and $VSe_2$ monolayer (Right).

To study the electronic properties of this 2D systems, the band structure and DOS of FM TMXX' monolayers have been calculated (**Figure 3.39**). $VX_2$ and $MnX_2$ were previously predicted to be ferromagnetic semiconductors[182, 183]. However, TMXX' are metallic with ferromagnetism and high spin-polarization. Particularly, MnSSe and VSSe monolayers are intrinsic half-metallicity, leading to 100% spin-polarized electrons at the Fermi level. Moreover, the MnSSe shows the large half-metallic gap of 1.15 eV (defined as the spin–flip transition energy from two spin channels), which can efficiently prevent the spin flip transitions and can guarantee the pure spin current.

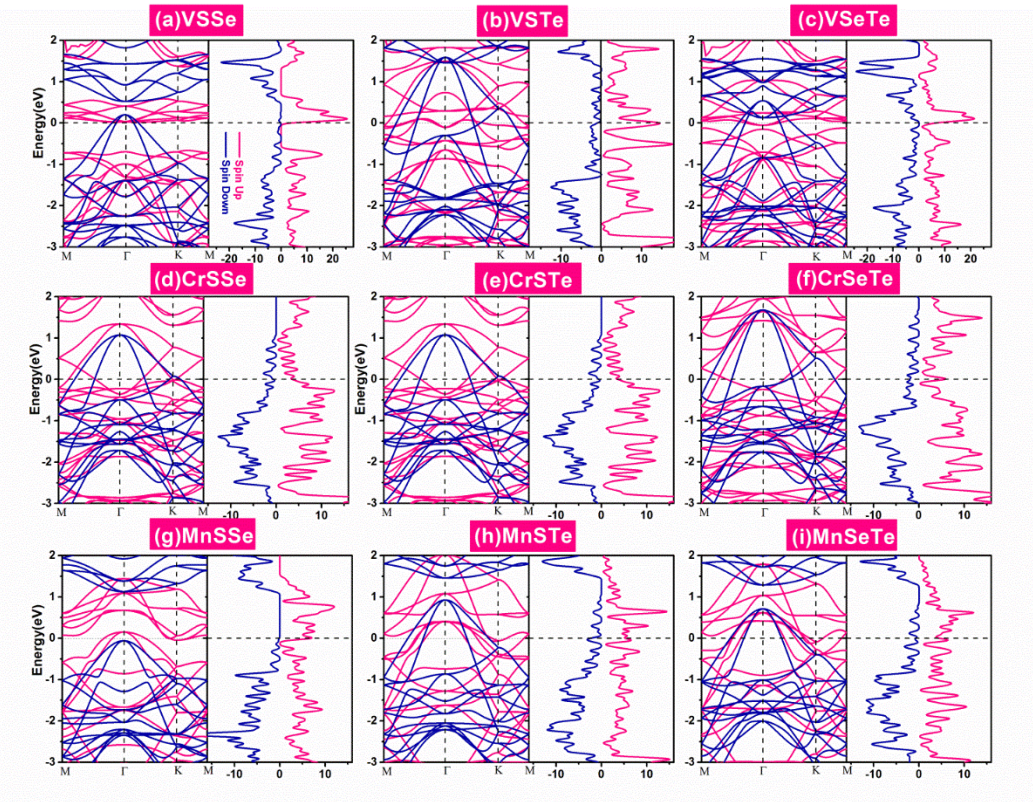


**Figure 3.39** Electronic band structures and DOS of the Janus TMDs monolayer with majority (pink line) and minority (blue line) spins. The Fermi level is denoted by a dashed line at 0 eV.

To further understand electronic and magnetic properties of TMXX', PDOS of Cr/Mn and S/Se atoms for CrSSe and MnSSe monolayers are shown in **Figure 3.40**. According to the perfect octahedral crystal field of TM atoms, the 3*d* orbitals will split into 2-fold $e_g$ ($d_{z^2}$ and $d_{x^2-y^2}$) orbitals and 3-fold degenerate $t_{2g}$ ($d_{xy}$, $d_{yz}$ and $d_{xz}$) orbitals. However, TMXX' monolayers have broken the structural symmetry. The different chalcogen atoms in top and bottom layer will induce the non-degenerated d states. PDOS for Cr-3*d* and Mn-3*d* states show different orbital features. The S atoms have lager spin splitting than Se atoms because the stronger interaction between S and TM (**Figure 3.40**). The states around the Fermi level are mainly derived from Cr/Mn-3*d* states and S/Se-2*p* states. In summary, the strong interaction between TM and X/X' results in the delocalized metallic states of TMXX' monolayers.

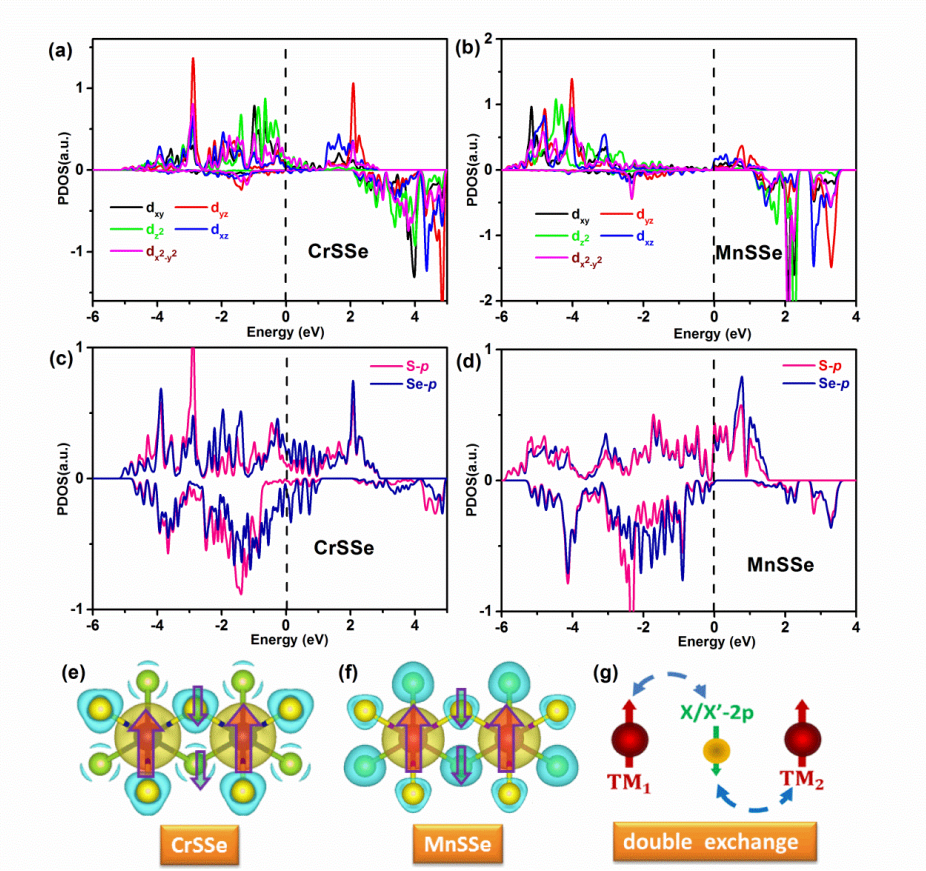


**Figure 3.40** PDOS of Cr (a) and S/Se (c) for CrSSe monolayer and PDOS Mn (b) and S/Se (d) for MnSSe monolayer. The Fermi level is set to zero. Spin-polarized charge densities with spin directions for CrSSe (e) and MnSSe (f) are shown (yellow and green dotted areas show spin-up and spin-down, respectively). Up and down arrows indicate spin-up and spin-down, respectively. (g) The schemes of the exchange mechanism for Janus TMDs monolayer.

To study the origin of magnetic exchange interactions for Janus TMXX' monolayer, the spin-polarized charge densities and schematics of the magnetic exchange mechanisms are plotted (**Figure 3.40**). Because of the delocalized TM-3*d* orbital, the d electrons can induce the spin-polarization on neighboring S/Se atoms. The spin-polarization for S and Se atoms also were identified by spin-splitting of PDOS. Two TM atoms and the nearest neighboring S/Se atoms maintain an antiferromagnetic coupling. Therefore, the ferromagnetic couplings of TM atoms in Janus TMXX' monolayer are mediated by X-2*p* states via a double-exchange mechanism (**Figure 3.40**). Consequently, the ferromagnetic order is the most favorable.

### 3.5.3 Summary

A new class of 2D magnetic TMDs (Janus TMDs), TMXX' (TM= V, Cr and Mn; X, X'= S, Se and Te, X ≠ X') was reported. TMXX' monolayers show robust ferromagnetic ordering large spin-polarization and high $T_C$. In particular, the MnSSe monolayer show strong half-metallic character with 100% spin polarization. The predicted $T_C$ of TMXX monolayers are much higher than that of the experimentally reported 2D $CrI_3$[63] and $Cr_2Ge_2Te_6$[61]. Our analysis of electronic and magnetic properties of Janus TMXX' motivates the research of new type of 2D materials with intrinsic ferromagnetism and potential for future spintronics.

# CHAPTER 4. Discussions

The realization, tuning and manipulation of magnetism in low-dimensional systems can drive the design of new nanodevices and can potentially revolutionize the development of information technology. It also drives and motivates our research on low-dimensional magnetic materials.

In general, the family of TMCs[13], including transition metal monochalcogenides, transition metal dichalcogenides, and other stoichiometries with the general formula of $M_mX_n$ (M is the transition metal, and X represents S, Se, and Te), represents an emerging class of layered materials with a wide range of robust electronic, optoelectronic, and magnetic properties. For example, chromium chalcogenides ($Cr_mX_n$, X = S, Se and Te, and m< n), a class of layered materials with robust magnetic ordering, have attracted increasing research interest[13]. With different amounts of Cr vacancies in the intercalated Cr layers, a range of $Cr_mX_n$ with different stoichiometric ratios (such as, CrX and $Cr_2X_3$) can be formed, having various magnetic ground states[184-186]. Epitaxial $Cr_mX_n$ thin films with thicknesses down to several nanometers have been grown on various substrates (such as, $SrTiO_3$), showing high $T_C$ and promising electrical transport properties (e.g., unconventional anomalous Hall effect[186]) for spintronic devices. Moreover, 2D magnetisms in TMCs can be manipulated by various extrinsic perturbations and fields, including strain, light, pressure, impurities, defects, dopants and proximity effects as well as moiré patterns[13]. Challenges remain in identifying TMDs with intrinsic 2D magnetism and room temperature FM ordering. Therefore, we proposed that FM Janus TMDs show the intrinsic spin polarization and high $T_C$, indicating they can be used in spintronics.

Unlike 2D TMDs, 2D MXenes are suitable materials for interdisciplinary research and collaboration between academia and industry[17]. Although MXenes are a large family of 2D compounds with a high potential for energy storage, research on their magnetic, properties is still in the preliminary stages. 2D magnetisms in MXenes are abundant due to the adjustable functionalization and stoichiometric ratio of transition metals (see Sections 3.1, 3.2 and 3.3). In particular, our investigation (Section 3.3) highlights that $Cr_2C$-based MXenes display not only valley properties but also the valley Hall effect, which has major implications for the expansion

of valleytronics and for the development of topological insulators.The valley Hall effect of several ferrovalley materials have been theoretically proposed[187-190]. 2H-$VSe_2$ [116]was identified as the ideal ferrovalley material with a high $T_C$ (588 K) and large valley splitting (112.1 meV) at the HSE06 level. Comparatively, our results indicate that $Cr_2COX$ MXenes, with a high $T_C$ and robust spin and valley polarization, are the best valleytronics materials described so far. Furthermore, opening up new practical applications for functionalized $Cr_2C$ MXenes already prepared by chemical exfoliation. Moreover, our results also indicate that valley polarization can be induced in several magnetic MXenes by surface engineering and that valley accumulations on the edges of these materials are important in valleytronics.[156, 191] However, valley polarization of Janus $Cr_2COF$ MXene (334 meV) is stronger than that of mixed $Cr_2CO_{0.75}F_{1.25}$ MXenes (11 meV) because symmetry is higher in the former material.

The disordering of functionalization on MXenes surfaces is an experimental reality and may acutely reduce the spin transmission life and weaken valley splitting. Consequently, further experimental research is still needed to ascertain how to manipulate the valley degree of freedom on MXenes by controlling the concentration and ordering of their functional groups.

Up to now, a series of new 2D nanomaterials have been either prepared or proposed, such as in-plane vacancy ordering MXene[192] (*i*-MXene), transition metal borides[193] (MBene) and Anti-MXenes[194], whose magnetism can also be manipulated by introducing functional groups. Therefore, our computational paradigm can be used to identify other 2D nanomaterials with similar magnetic properties and to design functionalization approaches aimed at spintronics and valleytronics applications.

# CHAPTER 5. Conclusions

The aim of this thesis is to develop and to design new magnetic materials with low dimensionality, intrinsic magnetic orders, robust spin and valley polarization, as well as high magnetic transition temperatures. Computational results demonstrate that we have discovered and developed new 2D magnetic materials with novel electronic and magnetic properties, such as half-semiconducting MXenes, bipolar antiferromagnetic MXenes, antiferromagnetic nanowires, and ferrovalley and antiferrovalley MXenes. Our work has not only significantly broaden the family of low-dimensional magnetic materials for spintronics and valleytronics applications, but also serves as a theoretical guide for future experimental works. The major achievements of this thesis are briefly summarized below:

First, a new 2D BAFS MXene is reported for asymmetrical and mixed functionalization of $Cr_2TiC_2$ double MXenes. The valence and conduction bands in band structures of BAFS materials are made up of opposite spin channels in a compensated AFM order (*i.e.*, the net magnetic moment is zero). We found that carriers (electrons and holes) doping can easily manipulate the spin carrier orientation, leading to the transition from BAFS to HMAF, which can be experimentally realized by using the gate voltage. Moreover, the BAFS characteristics are also presented in systems with mixed functionalization (*i.e.*, $Cr_2TiC_2F_xCl_{2-x}$). Our results open a new way for AFM spintronics and the realization of AFM spin field effect transistors.

Second, we found that modifying the stoichiometry and/or surface functionalization of *i*-MXenes can change their physical and chemical properties qualitatively. We found that these *i*-MXenes are excellent candidates for spintronics applications. In this study, $(V_{2/3}Zr_{1/3})_2CX_2$, $(V_{2/3}\square_{1/3})_2CF_2$ and $(V_{2/3}\square_{1/3})_2C(OH)_2$ *i*-MXenes are theoretically predicted to be stable. Among them, $(V_{2/3}Zr_{1/3})_2CO_2$, $(V_{2/3}\square_{1/3})_2CF_2$ and $(V_{2/3}\square_{1/3})_2C(OH)_2$ *i*-MXenes are half-semiconductor materials. The predicted $T_C$ (270 K) for $(V_{2/3}Zr_{1/3})_2CO_2$ MXene is higher than that of the experimentally reported 2D $CrI_3$ crystals (45 K). Hence, $(V_{2/3}Zr_{1/3})_2CO_2$ *i*-MXene is the best candidate for spintronic applications. The functionalization of *i*-MXenes can radically change the composition of their frontier orbitals, thereby affecting their work function. In particular, we found that $(V_{2/3}Zr_{1/3})_2C(OH)_2$ *i*-MXene can be used as an ultra-low work function (1.37 eV) electron emitter. Conversely, $(V_{2/3}\square_{1/3})_2CF_2$ MXene has a rather high WF of 7.47 eV, which is

thus higher than that of the Pt metal. Therefore, $(V_{2/3}\square_{1/3})_2CF_2$ *i*-MXenes can be used for holes injection in applications requiring Schottky-barrier-free contacts. Therefore, $(V_{2/3}Zr_{1/3})_2C(OH)_2$ and vacancy-ordered $(V_{2/3}\square_{1/3})_2CF_2$ *i*-MXenes are also promising candidates for electronic devices. Overall, our results establish a new family of *i*-MXenes with intrinsic magnetism, which makes them ideal candidates for both spintronics and electronics in the near future.

Third, we investigated the valleytronics properties of $Cr_2C$ MXenes with Janus and mixed functionalization. They exhibit intrinsic valley polarization in band structures due to the naturally broken inversion symmetry via surface-engineering driving. Janus $Cr_2COX$ (X= F, Cl and OH) MXenes were identified as ideal candidates for ferrovalley materials, having high $T_C$ and robustly intrinsic spin and valley polarization. In particular, $Cr_2COF$ MXene as the optimal candidate shows the robust valley polarization (334 meV) at two inequivalent K points. Moreover, $Cr_2C$ MXenes with mixed functionalizations also exhibit the spin and valley polarization. The underlying physical mechanisms of the valley polarization in Janus and mixed functionalized $Cr_2C$ MXenes derives from different Cr-3*d* orbital contributions in valleys. Berry curvature calculations reveal the spontaneous valley polarization in Janus and mixed functionalized $Cr_2C$ MXenes. In addition, the bipolar AFM $Cr_2TiC_2FCl$ MXene also exhibits the intrinsic valley polarization, which provides a new idea to design antiferrovalley materials. Our work provides a promising platform for probing valleytronics in MXenes and provides an experimentally workable approach (*i.e.* surface-engineering driving) for chemically exfoliated MXenes.

Fourth, we presented a new strategy in $VS_4$ NWs towards AFM spintronics. The $VS_4$ NWs are bound together by Van der Waals forces to form quasi 1D $VS_4$ nanorods. We investigated geometric, electronic and magnetic properties of the $VS_4$ bulk phase and isolated $VS_4$ NWs. The stability of the $VS_4$ bulk phase and isolate $VS_4$ NW are acceptable. After that, we investigated the electronic and magnetic properties of $VS_4$ NWs. The isolate $VS_4$ NW is an AFM semiconductor with a high $T_N$ (210 K). We found that carrier doping can separate the spin degeneracy to induce local spin polarization. The isolated $VS_4$ NW represent the half-metallic antiferromagnets resulting from carrier doping. Our results indicate that the isolated $VS_4$ NW is a promising 1D material for AFM spintronic applications. In addition, we found that BN nanotubes can provide protection by preventing oxidation while preserving the electronic and

magnetic properties of $VS_4$ NWs. This work shows the potential application of 1D NWs in AFM spintronics by inducing HMAF.

Finally, we proposed a new class of 2D magnetic materials, Janus monolayer transition-metal dichalcogenides, TMXX' (TM= V, Cr and Mn; X, X'= S, Se and Te, $X \neq X'$). The stability for TMXX' have been confirmed by phonon spectrum calculation. They show robust ferromagnetic ordering large spin-polarization and high $T_C$. Particularly, MnSSe monolayer is a half-metal with a large half-metal gap and 100% spin polarization. Our results show the Janus TMXX' set a new type of 2D materials with intrinsic ferromagnetism and also provide new opportunities for future spintronics.

Our study establishes a promising platform for probing spintronics and valleytronics in low-dimensional materials. Hence, we strongly recommend pursuing experimental efforts targeting magnetic MXenes, TMDs and nanowires to unveil further spintronics and valleytronics materials in the near future.

Results reported herein were published in four papers, which are included as attachments for more details. The work of MXenes in valleytronics (Section 3.3) have been submitted to "Journal of Materials Chemistry C".

# References


[1] Gibertini, M., M. Koperski, A. F. Morpurgo, and K. S. Novoselov, *Nature Nanotechnology*, **2019**, 14, 5, 408-419.

[2] Mannix, A. J., B. Kiraly, M. C. Hersam, and N. P. Guisinger, *Nature Reviews Chemistry*, **2017**, 1, 2, 0014.

[3] Sun, H., et al., *Nature Reviews Materials*, **2017**, 2, 6, 17023.

[4] Wang, M.-C., et al., *Annalen der Physik*, **2020**, 532, 5, 1900452.

[5] Ahn, E. C., *npj 2D Materials and Applications*, **2020**, 4, 1, 17.

[6] Li, B. L., et al., *Advanced Functional Materials*, **2016**, 26, 39, 7034-7056.

[7] Choi, W., et al., *Materials Today*, **2017**, 20, 3, 116-130.

[8] Geim, A. K. and K. S. Novoselov, *Nature Materials*, **2007**, 6, 3, 183-191.

[9] Kang, J., Z. Wei, and J. Li, *ACS Applied Materials & Interfaces*, **2019**, 11, 3, 2692-2706.

[10] Vogt, P., et al., *Physical Review Letters*, **2012**, 108, 15, 155501.

[11] Carvalho, A., et al., *Nature Reviews Materials*, **2016**, 1, 11, 16061.

[12] Feng, B., L. Chen, and K. Wu, *Synthesis of Borophene*, in *2D Boron: Boraphene, Borophene, Boronene*, I. Matsuda and K. Wu, Editors. 2021, Springer International Publishing: Cham. p. 51-72.

[13] Huang, Y. L., W. Chen, and A. T. S. Wee, *SmartMat*, **2021**, n/a, n/a,

[14] Cai, J., et al., *Nature Nanotechnology*, **2014**, 9, 11, 896.

[15] Shang, C., L. Fu, S. Zhou, and J. Zhao, *JACS Au*, **2021**, 1, 2, 147-155.

[16] Tsukagoshi, K., et al., *Physica B: Condensed Matter*, **2002**, 323, 1, 107-114.

[17] Gogotsi, Y. and B. Anasori, *ACS Nano*, **2019**, 13, 8, 8491-8494.

[18] Naguib, M., V. N. Mochalin, M. W. Barsoum, and Y. Gogotsi, *Advanced Materials*, **2014**, 26, 7, 992-1005.

[19] Naguib, M., et al., *Advanced Materials*, **2011**, 23, 37, 4248-4253.

[20] Alhabeb, M., et al., *Chemistry of Materials*, **2017**, 29, 18, 7633-7644.

[21] Sokol, M., V. Natu, S. Kota, and M. W. Barsoum, *Trends in Chemistry*, **2019**, 1, 2, 210-223.

[22] Anasori, B., et al., *ACS Nano*, **2015**, 9, 10, 9507-9516.

[23] Dahlqvist, M. and J. Rosen, *Nanoscale*, **2020**, 12, 2, 785-794.

[24] Dahlqvist, M., et al., *Science Advances*, **2017**, 3, 7, e1700642.

[25] Dahlqvist, M., et al., *ACS Nano*, **2018**, 12, 8, 7761-7770.

[26] Lind, H., J. Halim, S. I. Simak, and J. Rosen, *Physical Review Materials*, **2017**, 1, 4, 044002.

[27] Tao, Q., et al., *Nature Communications*, **2017**, 8, 1, 14949.

[28] Lei, J.-C., X. Zhang, and Z. Zhou, *Frontiers of Physics*, **2015**, 10, 3, 276-286.

[29] Hong Ng, V. M., et al., *Journal of Materials Chemistry A*, **2017**, 5, 7, 3039-3068.

[30] Jiang, X., et al., *Physics Reports*, **2020**, 848, 1-58.

[31] Khazaei, M., et al., *Advanced Functional Materials*, **2013**, 23, 17, 2185-2192.

[32] Khazaei, M., et al., *Journal of Materials Chemistry C*, **2017**, 5, 10, 2488-2503.

[33] Wang, Q. H., et al., *Nature Nanotechnology*, **2012**, 7, 11, 699-712.

[34] Manzeli, S., et al., *Nature Reviews Materials*, **2017**, 2, 8, 17033.

[35] Splendiani, A., et al., *Nano Letters*, **2010**, 10, 4, 1271-1275.

[36] Johari, P. and V. B. Shenoy, *ACS Nano*, **2012**, 6, 6, 5449-5456.

[37] Podzorov, V., et al., *Applied Physics Letters*, **2004**, 84, 17, 3301-3303.

[38] Mak, K. F. and J. Shan, *Nature Photonics*, **2016**, 10, 4, 216-226.

[39] Zhang, J., et al., *ACS Nano*, **2017**, 11, 8, 8192-8198.

[40] Lu, A.-Y., et al., *Nature Nanotechnology*, **2017**, 12, 8, 744-749.

[41] Çakır, D., E. Durgun, O. Gülseren, and S. Ciraci, *Physical Review B*, **2006**, 74, 23, 235433.

[42] Le, D., et al., *Surface Science*, **2013**, 611, 1-4.

[43] Flores, E., et al., *ACS Applied Energy Materials*, **2018**, 1, 5, 2333-2340.

[44] Pham, T., et al., *Science*, **2018**, 361, 6399, 263-266.

[45] Lu, H. and A. Seabaugh, *IEEE Journal of the Electron Devices Society*, **2014**, 2, 4, 44-49.

[46] Ionescu, A. M. and H. Riel, *Nature*, **2011**, 479, 7373, 329-337.

[47] Thomas, S., *Nature Electronics*, **2018**, 1, 12, 613-613.

[48] Liu, X. and M. C. Hersam, *Nature Reviews Materials*, **2019**, 4, 10, 669-684.

[49] Ratner, M., *Nature Nanotechnology*, **2013**, 8, 6, 378-381.

[50] Akinwande, D., N. Petrone, and J. Hone, *Nature Communications*, **2014**, 5, 1, 5678.

[51] Han, W., R. K. Kawakami, M. Gmitra, and J. Fabian, *Nature Nanotechnology*, **2014**, 9, 10, 794-807.

[52] Yang, T., T. Kimura, and Y. Otani, *Nature Physics*, **2008**, 4, 11, 851-854.

[53] Žutić, I., J. Fabian, and S. Das Sarma, *Reviews of Modern Physics*, **2004**, 76, 2, 323-410.

[54] Yamaguchi, A., et al., *Physical Review Letters*, **2004**, 92, 7, 077205.

[55] Wolf, S. A., et al., *Science*, **2001**, 294, 5546, 1488-1495.

[56] Awschalom, D. D. and M. E. Flatté, *Nature Physics*, **2007**, 3, 3, 153-159.

[57] Song, T., et al., *Science*, **2018**, 360, 6394, 1214-1218.

[58] Dery, H., P. Dalal, Ł. Cywiński, and L. J. Sham, *Nature*, **2007**, 447, 7144, 573-576.

[59] Deng, Y., et al., *Nature*, **2018**, 563, 7729, 94-99.

[60] Bonilla, M., et al., *Nature Nanotechnology*, **2018**, 13, 4, 289-293.

[61] Gong, C., et al., *Nature*, **2017**, 546, 7657, 265-269.

[62] Huang, B., et al., *Nature Nanotechnology*, **2018**, 13, 7, 544-548.

[63] Huang, B., et al., *Nature*, **2017**, 546, 7657, 270-273.

[64] Li, X. and J. Yang, *National Science Review*, **2016**, 3, 3, 365-381.

[65] Felser, C., G. H. Fecher, and B. Balke, *Angewandte Chemie International Edition*, **2007**, 46, 5, 668-699.

[66] Park, J. H., et al., *Nature*, **1998**, 392, 6678, 794-796.

[67] Coey, J. M. D. and S. Sanvito, *Journal of Physics D: Applied Physics*, **2004**, 37, 7, 988-993.

[68] Bafekry, A., B. Akgenc, M. Ghergherehchi, and F. M. Peeters, *Journal of Physics: Condensed Matter*, **2020**, 32, 35, 355504.

[69] Huang, L., et al., *Nature Materials*, **2016**, 15, 11, 1155-1160.

[70] You, J.-Y., et al., *Physical Review Research*, **2020**, 2, 1, 013002.

[71] Cheng, Y. C., et al., *Physical Review B*, **2013**, 87, 10, 100401.

[72] Furdyna, J. K., *Journal of Applied Physics*, **1988**, 64, 4, R29-R64.

[73] Liu, Y., et al., *Journal of Solid State Chemistry*, **2011**, 184, 5, 1273-1278.

[74] Huang, C., et al., *Physical Review Letters*, **2018**, 120, 14, 147601.

[75] Martí, X., I. Fina, and T. Jungwirth, *IEEE Transactions on Magnetics*, **2015**, 51, 4, 1-4.

[76] MacDonald, A. H. and M. Tsoi, *Philosophical Transactions of the Royal Society A: Mathematical, Physical and Engineering Sciences*, **2011**, 369, 1948, 3098-3114.

[77] Gomonay, E. V. and V. M. Loktev, *Low Temperature Physics*, **2014**, 40, 1, 17-35.

[78] Němec, P., M. Fiebig, T. Kampfrath, and A. V. Kimel, *Nature Physics*, **2018**, 14, 3, 229-241.

[79] van Leuken, H. and R. A. de Groot, *Physical Review Letters*, **1995**, 74, 7, 1171-1173.

[80] Galanakis, I. and E. Şaşıoğlu, *Applied Physics Letters*, **2011**, 99, 5, 052509.

[81] Galanakis, I., *Theory of Heusler and Full-Heusler Compounds*, in *Heusler Alloys: Properties, Growth, Applications*, C. Felser and A. Hirohata, Editors. 2016, Springer International Publishing: Cham. p. 3-36.

[82] Özdog˘an, K. and I. Galanakis, *Journal of Magnetism and Magnetic Materials*, **2009**, 321, 15, L34-L36.

[83] Gong, S.-J., et al., *Proceedings of the National Academy of Sciences*, **2018**, 115, 34, 8511-8516.

[84] Fukuma, Y., et al., *Nature Materials*, **2011**, 10, 7, 527-531.

[85] Dankert, A. and S. P. Dash, *Nature Communications*, **2017**, 8, 1, 16093.

[86] Drögeler, M., et al., *Nano Letters*, **2016**, 16, 6, 3533-3539.

[87] Maassen, J., W. Ji, and H. Guo, *Nano Letters*, **2011**, 11, 1, 151-155.

[88] Yazyev, O. V. and M. I. Katsnelson, *Physical Review Letters*, **2008**, 100, 4, 047209.

[89] Seneor, P., et al., *MRS Bulletin*, **2012**, 37, 12, 1245-1254.

[90] Tang, X., T. Fan, C. Wang, and H. Zhang, *Small*, **2021**, n/a, n/a, 2005640.

[91] Magda, G. Z., et al., *Nature*, **2014**, 514, 7524, 608-611.

[92] Kochan, D., S. Irmer, and J. Fabian, *Physical Review B*, **2017**, 95, 16, 165415.

[93] Hirsch, J. E., *Physical Review Letters*, **1999**, 83, 9, 1834-1837.

[94] Sinova, J., et al., *Physical Review Letters*, **2004**, 92, 12, 126603.

[95] Kato, Y. K., R. C. Myers, A. C. Gossard, and D. D. Awschalom, *Science*, **2004**, 306, 5703, 1910-1913.

[96] Bernevig, B. A. and S.-C. Zhang, *Physical Review Letters*, **2006**, 96, 10, 106802.

[97] Chang, C.-Z., et al., *Science*, **2013**, 340, 6129, 167-170.

[98] Francescato, Y., V. Giannini, and S. A. Maier, *New Journal of Physics*, **2013**, 15, 6, 063020.

[99] Behnia, K., *Nature Nanotechnology*, **2012**, 7, 8, 488-489.

[100] Zhong, D., et al., *Science Advances*, **2017**, 3, 5, e1603113.

[101] Liu, Y., et al., *Nano Research*, **2019**, 12, 11, 2695-2711.

[102] Vitale, S. A., et al., *Small*, **2018**, 14, 38, 1801483.

[103] Molina-Sánchez, A., D. Sangalli, L. Wirtz, and A. Marini, *Nano Letters*, **2017**, 17, 8, 4549-4555.

[104] Yu, T. and M. W. Wu, *Physical Review B*, **2014**, 89, 20, 205303.

[105] Mak, K. F., D. Xiao, and J. Shan, *Nature Photonics*, **2018**, 12, 8, 451-460.

[106] Schaibley, J. R., et al., *Nature Reviews Materials*, **2016**, 1, 11, 16055.

[107] Wang, Y., et al., *Nanoscale Horizons*, **2019**, 4, 2, 396-403.

[108] Manca, M., et al., *Nature Communications*, **2017**, 8, 1, 14927.

[109] Jiang, C., et al., *Nature Communications*, **2018**, 9, 1, 753.

[110] Schaibley, J., *Chapter 10 - Valleytronics in 2D semiconductors*, in *2D Materials for Photonic and Optoelectronic Applications*, Q. Bao and H.Y. Hoh, Editors. 2020, Woodhead Publishing. p. 281-302.

[111] Stier, A. V., et al., *Nature Communications*, **2016**, 7, 1, 10643.

[112] Nagler, P., et al., *Nature Communications*, **2017**, 8, 1, 1551.

[113] MacNeill, D., et al., *Physical Review Letters*, **2015**, 114, 3, 037401.

[114] Qi, J., X. Li, Q. Niu, and J. Feng, *Physical Review B*, **2015**, 92, 12, 121403.

[115] Tong, W.-Y., S.-J. Gong, X. Wan, and C.-G. Duan, *Nature Communications*, **2016**, 7, 1, 13612.

[116] Liu, J., et al., *Journal of Physics: Condensed Matter*, **2017**, 29, 25, 255501.

[117] Koch, W. and M. C. Holthausen, *A chemist's guide to density functional theory*. 2015: John Wiley & Sons.

[118] Born, M. and R. Oppenheimer, *Annalen der Physik*, **1927**, 389, 20, 457-484.

[119] Hohenberg, P. and W. Kohn, *Physical Review*, **1964**, 136, 3B, B864-B871.

[120] Kohn, W. and L. J. Sham, *Physical Review*, **1965**, 140, 4A, A1133-A1138.

[121] Jones, R. O., *Reviews of Modern Physics*, **2015**, 87, 3, 897-923.

[122] Thomas, H. L. and R. H. Fowler, *Proceedings of the Royal Society of London. Series A, Containing Papers of a Mathematical and Physical Character*, **1927**, 114, 768, 561-576.

[123] Hille, E., *Proceedings of the National Academy of Sciences*, **1969**, 62, 1, 7-10.

[124] Dirac, P. A. M., *Mathematical Proceedings of the Cambridge Philosophical Society*, **2008**, 26, 3, 376-385.

[125] Perdew, J. P., *Physical Review B*, **1986**, 33, 12, 8822-8824.

[126] Perdew, J. P., K. Burke, and M. Ernzerhof, *Physical Review Letters*, **1996**, 77, 18, 3865-3868.

[127] Hammer, B., L. B. Hansen, and J. K. Nørskov, *Physical Review B*, **1999**, 59, 11, 7413-7421.

[128] Adamo, C. and V. Barone, *The Journal of Chemical Physics*, **1999**, 110, 13, 6158-6170.

[129] Heyd, J., G. E. Scuseria, and M. Ernzerhof, *The Journal of Chemical Physics*, **2003**, 118, 18, 8207-8215.

[130] Anisimov, V. I., F. Aryasetiawan, and A. I. Lichtenstein, *Journal of Physics: Condensed Matter*, **1997**, 9, 4, 767-808.

[131] Loschen, C., J. Carrasco, K. M. Neyman, and F. Illas, *Physical Review B*, **2007**, 75, 3, 035115.

[132] Dudarev, S. L., et al., *Physical Review B*, **1998**, 57, 3, 1505-1509.

[133] Kresse, G. and D. Joubert, *Physical Review B*, **1999**, 59, 3, 1758-1775.

[134] Kühne, T. D., *WIREs Computational Molecular Science*, **2014**, 4, 4, 391-406.

[135] Kühne, T. D., M. Krack, F. R. Mohamed, and M. Parrinello, *Physical Review Letters*, **2007**, 98, 6, 066401.

[136] Baroni, S., S. de Gironcoli, A. Dal Corso, and P. Giannozzi, *Reviews of Modern Physics*, **2001**, 73, 2, 515-562.

[137] Savrasov, S. Y., *Physical Review Letters*, **1992**, 69, 19, 2819-2822.

[138] Jiang, J.-W., B.-S. Wang, and T. Rabczuk, *Nanotechnology*, **2014**, 25, 10, 105706.

[139] Griffith, J. S., *The theory of transition-metal ions*. 1964: Cambridge University Press.

[140] He, J., P. Lyu, and P. Nachtigall, *Journal of Materials Chemistry C*, **2016**, 4, 47, 11143-11149.

[141] Xiang, H., et al., *Dalton Transactions*, **2013**, 42, 4, 823-853.

[142] Aoki, H., et al., *Reviews of Modern Physics*, **2014**, 86, 2, 779-837.

[143] Binder, K., et al., *Monte Carlo methods in statistical physics*. Vol. 7. 2012: Springer Science & Business Media.

[144] Berry, M. V., *Proceedings of the Royal Society of London. A. Mathematical and Physical Sciences*, **1984**, 392, 1802, 45-57.

[145] Fang, Z., et al., *Science*, **2003**, 302, 5642, 92-95.

[146] Resta, R., *Journal of Physics: Condensed Matter*, **2000**, 12, 9, R107-R143.

[147] Spaldin, N. A., *Journal of Solid State Chemistry*, **2012**, 195, 2-10.

[148] Thouless, D. J., M. Kohmoto, M. P. Nightingale, and M. den Nijs, *Physical Review Letters*, **1982**, 49, 6, 405-408.

[149] Mostofi, A. A., et al., *Computer Physics Communications*, **2008**, 178, 9, 685-699.

[150] Albuquerque, A. F., et al., *Journal of Magnetism and Magnetic Materials*, **2007**, 310, 2, Part 2, 1187-1193.

[151] Liu, L., et al., *Applied Surface Science*, **2019**, 480, 300-307.

[152] Wang, V., et al., *Computer Physics Communications*, **2021**, 108033.

[153] Wu, Q., et al., *Computer Physics Communications*, **2018**, 224, 405-416.

[154] Khazaei, M., et al., *Physical Review B*, **2015**, 92, 7, 075411.

[155] Liu, Y., H. Xiao, and W. A. Goddard, *Journal of the American Chemical Society*, **2016**, 138, 49, 15853-15856.

[156] Frey, N. C., et al., *ACS Nano*, **2019**, 13, 3, 2831-2839.

[157] Dong, L., et al., *The Journal of Physical Chemistry Letters*, **2017**, 8, 2, 422-428.

[158] Schultz, T., et al., *Chemistry of Materials*, **2019**, 31, 17, 6590-6597.

[159] He, J., et al., *Journal of Materials Chemistry C*, **2016**, 4, 27, 6500-6509.

[160] Si, C., J. Zhou, and Z. Sun, *ACS Applied Materials & Interfaces*, **2015**, 7, 31, 17510-17515.

[161] Sun, Q., Z. Fu, and Z. Yang, *Journal of Magnetism and Magnetic Materials*, **2020**, 514, 167141.

[162] He, J., et al., *Nanoscale*, **2019**, 11, 1, 356-364.

[163] Jing, Z., et al., *The Journal of Physical Chemistry Letters*, **2019**, 10, 19, 5721-5728.

[164] Hantanasirisakul, K., et al., *Nanoscale Horizons*, **2020**, 5, 12, 1557-1565.

[165] Hart, J. L., et al., *Advanced Materials Interfaces*, **2021**, 8, 5, 2001789.

[166] Li, X., et al., *Proceedings of the National Academy of Sciences*, **2013**, 110, 10, 3738-3742.

[167] Tong, W.-Y. and C.-G. Duan, *npj Quantum Materials*, **2017**, 2, 1, 47.

[168] Jungwirth, T., X. Marti, P. Wadley, and J. Wunderlich, *Nature Nanotechnology*, **2016**, 11, 3, 231-241.

[169] Gomonay, O., T. Jungwirth, and J. Sinova, *Physica Status Solidi-Rapid Research Letetrs*, **2017**, 11, 4, 1700022.

[170] Li, X., et al., *Journal of the American Chemical Society*, **2017**, 139, 18, 6290-6293.

[171] Wan, Y., Y. Sun, X. Wu, and J. Yang, *The Journal of Physical Chemistry C*, **2018**, 122, 1, 989-994.

[172] Zhang, T., L. Zhu, and G. Chen, *Journal of Materials Chemistry C*, **2016**, 4, 43, 10209-10214.

[173] Li, S.-s., et al., *Nanoscale*, **2018**, 10, 33, 15545-15552.

[174] Ye, H., et al., *Advanced Energy Materials*, **2017**, 7, 5, 1601602.

[175] Hillebrand, W., *Journal of the American Chemical Society*, **1907**, 29, 7, 1019-1029.

[176] Pan, H., *The Journal of Physical Chemistry C*, **2014**, 118, 24, 13248-13253.

[177] Fuh, H.-R., et al., *Scientific Reports*, **2016**, 6, 1, 32625.

[178] Gao, G., et al., *Nanoscale*, **2016**, 8, 16, 8986-8994.

[179] Ma, Y., et al., *Angewandte Chemie International Edition*, **2017**, 56, 34, 10214-10218.

[180] Hotta, T., S. Yunoki, M. Mayr, and E. Dagotto, *Physical Review B*, **1999**, 60, 22, R15009-R15012.

[181] Kan, M., et al., *The Journal of Physical Chemistry Letters*, **2013**, 4, 20, 3382-3386.

[182] Kan, M., S. Adhikari, and Q. Sun, *Physical Chemistry Chemical Physics*, **2014**, 16, 10, 4990-4994.

[183] Ma, Y., et al., *ACS Nano*, **2012**, 6, 2, 1695-1701.

[184] Cui, F., et al., *Advanced Materials*, **2020**, 32, 4, 1905896.

[185] Sun, X., et al., *Nano Research*, **2020**, 13, 12, 3358-3363.

[186] Zhao, D., et al., *Nano Research*, **2018**, 11, 6, 3116-3121.

[187] Peng, R., et al., *Physical Review B*, **2020**, 102, 3, 035412.

[188] Zhou, J., Q. Sun, and P. Jena, *Physical Review Letters*, **2017**, 119, 4, 046403.

[189] Shen, X.-W., H. Hu, and C.-G. Duan, *Chapter 3 - Two-dimensional ferrovalley materials*, in *Spintronic 2D Materials*, W. Liu and Y. Xu, Editors. 2020, Elsevier. p. 65-93.

[190] Hu, H., et al., *npj Computational Materials*, **2020**, 6, 1, 129.

[191] Xiao, D., et al., *Physical Review Letters*, **2012**, 108, 19, 196802.

[192] Gao, Q. and H. Zhang, *Nanoscale*, **2020**, 12, 10, 5995-6001.

[193] Wu, F., et al., *Physical Chemistry Chemical Physics*, **2021**,

[194] Gu, J., et al., *ACS Nano*, **2021**,

# List of Attached Publications

**The thesis is based on following articles:**

**Attachment No.1:**

**Shuo Li**, Junjie He, Petr Nachtigall, Lukáš Grajciar, and Federico Brivio,

Titel: Control of spintronic and electronic properties of bimetallic and vacancy-ordered vanadium carbide MXenes via surface functionalization, Physical Chemistry Chemical Physics, 2019, 21, 25802-25808.

To download this article, please use: https://doi.org/10.1039/C9CP05638F

**Attachment No.2:**

**Shuo Li**, Junjie He, Petr Nachtigall, Lukáš Grajciar, and Federico Brivio,

Title: Doping isolated one-dimensional antiferromagnetic semiconductor Vanadium tetrasulfide ($VS_4$) nanowires with carriers induces halfmetallicity, Journal of Materials Chemistry C, 2021, 9, 3122-3128.

To download this article, please use: https://doi.org/10.1039/D1TC00096A

**Attachment No.3:**

**Shuo Li**, Junjie He, Lukáš Grajciar, and Petr Nachtigall,

Title: Intrinsic valley polarization in 2D magnetic MXenes: surface engineering induced spin-valley coupling, submission to Journal of Materials Chemistry C.

**Attachment No.4:**

Junjie He and **Shuo Li**,

Title: Two-dimensional Janus transition-metal dichalcogenides with intrinsic ferromagnetism and half-metallicity, Computational Materials Science, 2018, 152, 151-157.

To download this article, please use: https://doi.org/10.1016/j.commatsci.2018.05.049

**Attachment No.5:**

Junjie He, Guangqian Ding, Chengyong Zhong, **Shuo Li**, Dengfeng Li, and Gang Zhang,

Titel: $Cr_2TiC_2$-based double MXenes: novel 2D bipolar antiferromagnetic semiconductor with gate-controllable spin orientation toward antiferromagnetic spintronics, Nanoscale, 2019, 11, 356-364.

To download this article, please use: https://doi.org/10.1039/C8NR07692H

# Attached Publications